



ulm university universität
uulm

**Fakultät für
Naturwissenschaften**

Institute of Theoretical
Physics

The Effects of Casimir Interactions in Experiments on Gravitationally-induced Entanglement

Bachelor Thesis

Submitted by:

Jan Bulling
jan.bulling@uni-ulm.de
1109395

Supervised by:

Marit O. E. Steiner, Julen S. Pedernales, Martin B. Plenio

Abstract

Contents

1	Introduction	5
1.1	Feynman's Gedankenexperiment	5
2	A first look	6
2.1	Time evolution under a gravitational potential	10
2.2	Entanglement measures	11
2.3	Issues with the idealized experimental procedure	15
3	Casimir effect	17
3.1	Proximity force approximation	19
3.2	Casimir forces between a conducting plate and a dielectric sphere	21
3.3	Imperfect plate and spheres	23
4	The particle in front of a static shield	26
4.1	Entanglement generation	29
4.2	The optimal setup	33
4.2.1	Orientation	33
4.2.2	Separation, mass and superposition size	39
4.3	Trapping the particle	43
4.4	Discussions	45
5	The consequences of a thermal shield	49
5.1	Thickness and size of the shield	49
5.1.1	Shielding Coulomb-Interactions	50
5.1.2	Shielding Casimir-Interactions	52
5.1.3	Gravitational effects of the shield	53
5.2	Thermal shield vibrations	53
5.3	Entanglement in front of a thermal shield	56
5.3.1	Analytic dynamics	59
5.3.2	Small shields	62
5.4	Discussions on the shield	62
6	Discussion and outlook	63
	Bibliography	64

Contents

A	TITLE TO BE DONE	69
A.1	Evolution under a gravitational Hamiltonian	69
A.1.1	Using time dependent perturbation theory	69
A.1.2	Using an exact time evolution	70
A.2	Exemplary calculation of E_N	70
B	Casimir interactions	72
B.1	Polarizability of a dielectric sphere	72
C	The shield and its consequences	74
C.1	Blocking of the shield	74
C.2	Thermal harmonic oscillator	74
D	Calculations	76

1 Introduction

Newton (1687)

Keplers law are inverse square of gravitational force

Maskelyne (1774) Gravitational force of a mountain [1, 2]

Cavendish (1798) Gravitational force via torsion pendulum

1.1 Feynman's Gedankenexperiment

2 A first look

Testing the quantum nature of gravity is no easy task and many proposals seek to detect gravitationally induced entanglement between two masses [3–6] as a form of proof. For all these proposals, gravity is assumed to be mediated by a gravitational field. During a time evolution, this field (like any other external field) can only perform local operations (LO) on the states of the test masses. If gravity is now assumed to behave classically, the propagation between the masses can be described by a classical communication (CC) channel [6, 7]. These LOCC operations however cannot turn an initially unentangled state into an entangled one [8, 9]. It immediately follows, that if one measures the involved masses to be entangled after a mutual gravitational interaction, gravity necessarily has to be quantum in some way. It is important to note, that the opposite of this statement is not true. Measuring unentangled masses does not directly imply the classicality of the gravitational field. This can be seen by considering operations that are non-LOCC and also produce unentangled states like for example the swap operation $|\psi\rangle_A |\phi\rangle_B \rightarrow |\phi\rangle_A |\psi\rangle_B$. This operations obviously can't induce entanglement to initially unentangled states, but requires the perfect exchange of quantum information between the states - which is not possible using classical communication alone. In other words: If one prepares masses initially in a pure product state and measures *any* state which cannot be obtained by LOCC-operations after some final time evolution, it is impossible for gravity to behave classical. One can even go so far and define the term ***quantum gravity*** as any interaction mediated by gravity that cannot be described by LOCC operations alone [7].

A plausible and logical idea for an experiment to test for gravitational induced entanglement is described in this chapter - which is, as a reminder, enough to prove a quantum nature of gravity. It requires the generation of coherent delocalized quantum superpositions of massive objects either as so-called Schrödinger-cat states or squeezed gaussian states [6, 10]. Theses masses are brought close enough together for gravity to have a measurable effect. The distances between different parts of the spatial superpositions must have different distances to the delocalized second mass. As a result - and of course *if gravity behaves quantum* - the states should get entangled. To see this, consider the ideal simplification of a real experimental setup where two bodies with mass m are trapped in an harmonic potential wall (like for example in an optical trap) with frequency ω separated by a distance d . The local Hamiltonian of the system is given by

$$\hat{H}_0 = \sum_{i=1,2} \frac{\hat{p}_i^2}{2m} + \frac{1}{2}m\omega^2\hat{x}_i^2 \quad (2.1)$$

where \hat{x} and \hat{p} are the position and momentum operators satisfying the canonical com-

mutation relation $[\hat{x}_i, \hat{p}_j] = i\hbar\delta_{ij}$. For now, all non-gravitational interactions between the masses have been ignored. In the low energy regime, where the energy transfer during a process is far below the Planck scale $m_p c^2 \sim 10^{19}$ GeV, gravity can be traded as an effective field theory with tools available similar to those for the electromagnetic field and QED [11]. In the non-relativistic limit $v \ll c$, the gravitational interaction can be described by a Newtonian $1/r$ potential acting on the center-of-mass positions, with all classical quantities are replaced by quantum operators [10–12]. Spatial superpositions lead to superpositions of the metric and consequently (in the non-relativistic limit) to a superposed Newtonian potential. The interaction Hamiltonian \hat{H}_G should therefore be describable by

$$\hat{H}_G = -\frac{Gm^2}{|d - \hat{x}_1 + \hat{x}_2|}, \quad (2.2)$$

where $G = 6.6743 \times 10^{-11} \text{ m}^3\text{kg}^{-1}\text{s}^{-2}$ is the gravitational constant. The separation of the masses d is chosen much larger than the extension of the delocalization (in this setup comparable to the position variance of the harmonic oscillator). This condition is realistic given that the biggest spatial delocalization ever achieved in matter wave experiments is in the order of 500 nm [13]. Expanding the Hamiltonian \hat{H}_G for small \hat{x}_i , only the second order term proportional to $(\hat{x}_1 - \hat{x}_2)^2$ can induce entanglement [3]. The zeroth order term is just a overall energy offset, the first order term $\propto (\hat{x}_1 - \hat{x}_2)$ as well as the terms \hat{x}_i^2 result only in a local interaction for each mass separately. The coupling term $-(\hat{x}_1\hat{x}_2 + \hat{x}_2\hat{x}_1) = -2\hat{x}_1\hat{x}_2$ however is very interesting as it couples both oscillators and can thus mediate entanglement. Introducing the ladder operators, the Hamiltonian $\hat{H} = \hat{H}_0 + \hat{H}_G$ can be expressed as [11]:

$$\hat{H} = \sum_{i=1,2} \hbar\omega \hat{a}_i^\dagger \hat{a}_i - \frac{Gm^2}{d^3} \left(\sqrt{\frac{\hbar}{2m\omega}} \right)^2 (\hat{a}_1\hat{a}_2 + \hat{a}_1\hat{a}_2^\dagger + \hat{a}_1^\dagger\hat{a}_2 + \hat{a}_1^\dagger\hat{a}_2^\dagger) \quad (2.3)$$

Applying the *rotating-wave approximation*¹, the terms $\hat{a}_1\hat{a}_2 + \hat{a}_1^\dagger\hat{a}_2^\dagger$ can be dropped. Defining the coupling strength g of the interaction as $g = Gm/\omega d^3$, eq (2.3) can be rewritten as

$$\hat{H} = \sum_{i=1,2} \hbar\omega \hat{a}_i^\dagger \hat{a}_i - \hbar g (\hat{a}_1\hat{a}_2^\dagger + \hat{a}_1^\dagger\hat{a}_2). \quad (2.4)$$

Now, for simplicity and as a simple example, the evolution of the initial Fock state $|\psi(0)\rangle = |10\rangle$ is considered. The gravitational interaction H_G can be treated as a time dependent perturbation and the state evolution is given as (for calculation see appendix A.1.1) [11]

$$|\psi(t=0)\rangle = |10\rangle \xrightarrow{\text{time } t} |\psi(t)\rangle = \mathcal{N} (|10\rangle - i g t |01\rangle + \mathcal{O}(g^2)) \quad (2.5)$$

¹This approximation is known from quantum optics, where all fast oscillating terms in the Hamiltonian can be dropped [7, 11]. In the interaction picture, the ladder operators evolve as $\hat{a}(t) = \hat{a}e^{-i\omega t}$. The terms like $\hat{a}_1(t)\hat{a}_2(t)$ oscillate with frequency 2ω whereas $\hat{a}_1^\dagger(t)\hat{a}_2(t)$ does not oscillate at all. Due to the small coupling, this approximation works very well here.

where \mathcal{N} is an appropriate normalization constant. The evolved state (2.5) is entangled and cannot be reduced into a product of two oscillator Fock states. The entanglement is very small since it is proportional to the gravitational coupling constant gt ². Another interesting result, which underlines the false inference of a classical gravity from observed non-entanglement discussed above can be seen by considering the time evolution of a coherent product state $|\alpha\rangle \otimes |\beta\rangle$ where $\hat{a}|\alpha\rangle = \alpha|\alpha\rangle$. The time evolution is derived in appendix A.1.2 and results in

$$e^{-i\hat{H}t/\hbar}(|\alpha\rangle \otimes |\beta\rangle) = |e^{-i\omega t}(\alpha \cos gt - \beta \sin gt)\rangle \otimes |e^{-i\omega t}(-\alpha \sin gt + \beta \cos gt)\rangle. \quad (2.6)$$

This state is clearly a product state and thus not entangled. But for a time $t_0 = \pi/2g$ the state is effectively the swapped initial state $|\beta\rangle \otimes |\alpha\rangle$ up to a local phase. This swap operation is however, as established earlier, not possible under a LOCC protocol. Thus, even if the resulting state after time evolution under a gravitational interaction is unentangled, we can rule out the classicality of gravity [7, 11]. Gravity must therefore be capable of transmitting quantum information and must be described by a quantum channel.

Experimentally, one requires the ability to generate spatial superpositions of two massive objects with large enough coherence times. Usually the weak gravitational interaction requires coherence times in the order of 100 ms – 10 s for any meaningful and measurable entanglement to build up. The masses should additionally be massive enough for their gravitational effects to be measurable. These requirements impose huge experimental and engineering challenges. To contextualize: The most massive object ever put into a spatial superposition in matter-wave interferometry is in the order of 4×10^{-23} kg [13], whereas the smallest object whose gravitational field has been measured was just below 100 mg [14] - a difference of 19 orders of magnitude. One way to experimentally create such spatial superpositions is giving the masses a spin-1/2 degree of freedom. For example, a nitrogen-vacancy diamonds can be used [6], where the NV site provides the required spin of 1/2. An applied magnetic gradient $\partial_x B$ functions like a “beam splitter” and creates a delocalized state. The extend of this superposition can be calculated and separations in the order of 100 μ m are theoretically achievable [6]. Levitated, trapped particles isolated and shielded in a vacuum can increase environmental isolation by avoiding contact with surrounding noise. The additional forces due to the trapping potential or the gravitational acceleration can be studied in advance. In this thesis, I assume that all required states and superpositions can be prepared experimentally.

The general and idealized problem considered is illustrated in fig. 2.1. Two massive bodies with masses M_A and M_B are initially separated by a center-to-center distance $2L$. The masses are prepared in a coherent delocalized quantum superposition Schrödinger-cat-like state in, for now, a parallel orientation as depicted in fig. 2.1. The extension of the superposition is denoted by Δx and is the same for both masses. It is important to choose the positions of the masses such that the distances between each part of the

²The amount of entanglement can for example be quantified with the later introduced *logarithmic negativity* E_N . For this state, it is given by $E_N(|\psi(t)\rangle\langle\psi(t)|) \simeq 2tg/\log 2 + \mathcal{O}(g^2) \geq 0$.

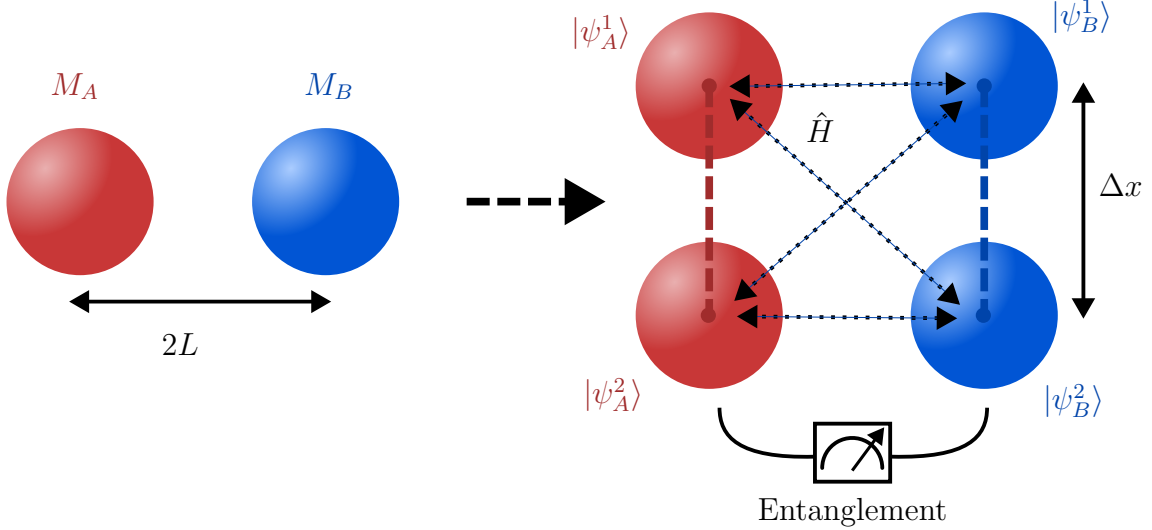


Figure 2.1: Schematic figure of the proposed experiment with two masses prepared in a spatial superposition state. The gravitational interaction \hat{H} induces different phases to each of the superpositions due to the different distances between all masses. This results in measurable entanglement after some time evolution.

delocalized mass A and B are not always identical. Otherwise, all built up phases are the same and no entanglement is observable. With the notation introduced in fig. 2.1, the initial state at $t = 0$ is given by

$$|\psi(t=0)\rangle = \frac{1}{2} (|\psi_A^1\rangle + |\psi_A^2\rangle) \otimes (|\psi_B^1\rangle + |\psi_B^2\rangle). \quad (2.7)$$

The state evolves under a Hamiltonian \hat{H} and after some time the position of each mass is measured and checked for entanglement. For now I assume that all interactions except gravity can be neglected. In reality, electromagnetic forces and Casimir-Polder interactions [15, 16] need to be considered.

As established earlier in this chapter, with some assumptions made, gravitational interaction can generate entanglement. In the time scales of the experiment, the acceleration of the masses due to the mutual gravitational interaction can be neglected³. The Hamiltonian therefore only needs to include the gravitational potential

$$\hat{V} = -\frac{GM_A M_B}{|\hat{D}|} \quad (2.8)$$

where \hat{D} is the distance operator between the masses. It depends on the individual positions \hat{x}_A and \hat{x}_B . During time evolution, the different parts of the superpositions

³Take for example a silica sphere ($\rho = 2648 \text{ kg/m}^3$) with $R = 10^{-5} \text{ m}$ separated by $2L = 4R$. The mutual gravitational acceleration for each sphere is around $a = GM/(2L)^2 = 5 \times 10^{-13} \text{ m/s}^2$ which results for $t \sim 1 \text{ s}$ in a distance traveled of $\sim 10^{-13} \text{ m}$.

built up different local phases. I am interested in calculating, how much entanglement one can expect from this kind of interactions.

2.1 Time evolution under a gravitational potential

Proposition 2.1. *The time evolution under a static and constant Hamiltonian $\hat{H} = \hat{V}(\hat{x}_i) = \text{const.}$ is given by the eigenenergies of the system $\hat{V} |n\rangle = V_n |n\rangle$ proportional to $e^{-iV_n t/\hbar}$.*

Proof. This is a trivial statement. The time evolution is governed by the Schrödinger equation

$$i\hbar \frac{\partial}{\partial t} |\psi(t)\rangle = \hat{H} |\psi(t)\rangle. \quad (2.9)$$

The formal solution of this first order PDE is given by

$$|\psi(t)\rangle = e^{-i\hat{V}t/\hbar} |\psi(t=0)\rangle. \quad (2.10)$$

The constant (hermitian) potential operator can be expressed in the energy-eigenbasis $\{|n\rangle\}$ as $\hat{V} |n\rangle = V_n |n\rangle$. The initial state can be expressed as a superposition in the same eigenstates like $|\psi\rangle = \sum_n c_n |\psi_n\rangle$. Putting both together and using the Taylor expansion of the exponential function, one arrives at the simple form

$$|\psi(t)\rangle = \sum_n e^{-i\hat{V}t/\hbar} |n\rangle \langle n|\psi\rangle = \sum_{n,k} \frac{(-i\hat{V}t/\hbar)^k}{k!} |n\rangle c_n |\psi_n\rangle \quad (2.11)$$

$$= \sum_{n,k} \frac{(-iV_n t/\hbar)^k}{k!} c_n |\psi_n\rangle = \sum_n e^{-iV_n t/\hbar} c_n |\psi_n\rangle \quad (2.12)$$

where in the second to last step $\hat{V}^k |n\rangle = \hat{V}^{k-1} \hat{V} |n\rangle = \hat{V}^{k-1} |n\rangle V_n = \dots = V_n^k |n\rangle$ was used. \square

Using the preceding proposition, the initial state eq. (2.7) can be evolved in time. The potential operator eq. (2.8) acts on every state in the $\{|\psi_A^1\rangle, |\psi_A^2\rangle\} \otimes \{|\psi_B^1\rangle, |\psi_B^2\rangle\}$ basis differently. This is because of the different distances between the states $|\psi_A^i\rangle$ and $|\psi_B^j\rangle$ for different $i, j \in \{1, 2\}$. This results in phases ϕ_{ij} to be built up during time evolution according to proposition 2.1. The state $|\psi(t)\rangle$ after some time evolution is therefore given as

$$|\psi(t)\rangle = \frac{1}{2} \left(e^{i\phi_{11}} |\psi_A^1\rangle |\psi_B^1\rangle + e^{i\phi_{12}} |\psi_A^1\rangle |\psi_B^2\rangle + e^{i\phi_{21}} |\psi_A^2\rangle |\psi_B^1\rangle + e^{i\phi_{22}} |\psi_A^2\rangle |\psi_B^2\rangle \right), \quad (2.13)$$

where the \otimes symbol was omitted. The phases are

$$\phi \equiv \phi_{11} = \phi_{22} = \frac{GM_A M_B}{2\hbar L} t \quad \text{and} \quad \phi_{12} = \phi_{21} = \frac{GM_A M_B}{\hbar \sqrt{4L^2 + (\Delta x)^2}} t. \quad (2.14)$$

Assuming again that the superposition size Δx is much smaller than the distance L between the masses - like before in eq. (2.2) - the phases $\phi_{12} = \phi_{21}$ can be expanded and a global phase ϕ can be factored:

$$\phi_{12} = \phi_{21} \approx \frac{GM_A M_B}{\hbar} \left[\frac{1}{2L} - \frac{(\Delta x)^2}{16L^3} \right] t \equiv \phi - \Delta\phi. \quad (2.15)$$

The state eq. (2.13) can now be expressed in the form

$$|\psi(t)\rangle = e^{i\phi} \frac{1}{\sqrt{2}} \left[|\psi_A^1\rangle \otimes \frac{|\psi_B^1\rangle + e^{-i\Delta\phi} |\psi_B^2\rangle}{\sqrt{2}} + |\psi_A^2\rangle \otimes \frac{e^{-i\Delta\phi} |\psi_B^1\rangle + |\psi_B^2\rangle}{\sqrt{2}} \right], \quad (2.16)$$

where the entanglement dynamics can be directly seen. This state is entangled, if it is not representable as a product state $|\psi\rangle \neq |\psi_A\rangle \otimes |\psi_B\rangle$. That is the case, if the states containing $|\psi_B^i\rangle$ are not both equal to each other (i.e. differ only by a phase) and thus cannot be factored. The system is therefore entangled, if and only if $\Delta\phi \neq k\pi$ with integer $k \in \mathbb{Z}$.

In order to assess in a more quantitative way how entangled the state $|\psi\rangle$ is, a more sophisticated entanglement measure is needed. In the next chapter, the **logarithmic negativity** is motivated and introduced. In the rest of this thesis, I will repeatedly opt for this measure.

2.2 Entanglement measures

Checking whether an arbitrary state ρ is entangled or not is no easy task. In fact, this problem is known to be NP-hard [17]. A state $\rho_{AB} \in \mathcal{H}_A \otimes \mathcal{H}_B$ is called entangled, if it is **non-separable**, that is, it cannot be expressed as a tensor product of two subsystems $\rho_A \in \mathcal{H}_A$ and $\rho_B \in \mathcal{H}_B$. Only for specific cases - like the case of two qubits or qubit-qutrit - a simple sufficient criterion for determining the separability of a general mixed state is known: The positive partial transpose (PPT) criterion states, that if the partial transpose of the density matrix is positive ($\rho^{\Gamma_A} > 0$ ⁴), the state ρ is separable [8, 9]. In other words, if ρ^{Γ_A} has negative eigenvalues, ρ is guaranteed to describe an entangled state. The inverse is true, if and only if the dimension of $\rho_A \otimes \rho_B$ is 2×2 or 3×2 [8] - otherwise, only having non-negative eigenvalues doesn't necessarily result in an unentangled system (such states are called "bound states"). The partial transpose with respect to a subsystem i can be understood in the same way as the partial trace, where the operation (in this case the transform) is performed only on indices corresponding the subsystem ρ_i . To see the necessity of the PPT criterion, consider a separable mixed state ρ , which can be generally expressed as

$$\rho = \sum p_i \rho_A^i \otimes \rho_B^i. \quad (2.17)$$

⁴A matrix is defined as positive ("positive definite"), if all eigenvalues are positive.

The partial transpose is in this case trivial:

$$\rho^{\Gamma_A} = \sum p_i (\rho_A^i)^T \otimes \rho_B^i. \quad (2.18)$$

Since the transpose preserves eigenvalues, the transposed subsystem A is still positive $(\rho_A^i)^T > 0$ and describes again a valid quantum state. It follows, that ρ^{Γ_A} is positive as well. If somehow ρ^{Γ_A} has any negative eigenvalues, this can only mean that the initial state ρ is not separable and cannot be expressed in the form of eq. (2.17) and the necessity of the criterion is shown.

For quantifying entanglement in a more precise way, a mathematical quantity called **entanglement measure** can be used. A good measure should be able to capture the essential features of entanglement. One can axiomatically state what properties such a measure $E(\rho)$ should have [8, 9]:

Normalization An entanglement measure should be a mapping from densities to real positive values between 0 and 1:

$$\rho \rightarrow E(\rho) \in \mathbb{R}^+ \quad (2.19)$$

where usually the maximally entangled state has $E = 1$.

Monotonicity under LOCC E should not increase under local operations and classical communications. This is the most important postulate for an entanglement measure and often cited as the *only* required postulate.

Vanishing on separable states $E(\rho) = 0$ if ρ is separable

Often one finds additional properties useful like *convexity* $E(\sum p_i \rho_i) \leq \sum p_i E(\rho_i)$ or (full) *additivity* $E(\rho \otimes \sigma) = E(\rho) + E(\sigma)$.

A function that satisfies the most important of these conditions is often called an *entanglement monotone*.

The **negativity** \mathcal{N} is such an entanglement monotone [9, 18] that used the PPT criterion to determine if a state is entangled or not. It is defined as

$$\mathcal{N} = \frac{\|\rho^{\Gamma_A}\|_1 - 1}{2} \quad (2.20)$$

where $\|A\|_1 = \text{tr} |A| = \text{tr} \sqrt{A^\dagger A}$ is the trace norm. The negativity however is not additive and a more suitable and widely used entanglement measure is the **logarithmic negativity** [8, 9, 19]

$$E_N(\rho) = \log_2 \|\rho^{\Gamma_A}\|_1. \quad (2.21)$$

The monotonicity of the logarithm implies, that E_N is an entanglement monotone as well. Furthermore, for the calculations it does not matter which subsystem is transposed.

Proposition 2.2. a) The partial transpose w.r.t. subsystem A is equal to the transposed partial transpose w.r.t. subsystem B : $\rho^{\Gamma_A} = (\rho^{\Gamma_B})^T$. b) The trace norms of partially transposed density operators w.r.t. any subsystem are equal: $\|\rho^{\Gamma_A}\|_1 = \|\rho^{\Gamma_B}\|_1$.

Proof. a) A general density matrix ρ can be expressed as

$$\rho = \sum_{i,j,k,l} \rho_{ij,kl} |i\rangle\langle j|_A \otimes |k\rangle\langle l|_B$$

The partial transpose with respect to subsystem B is then defined as

$$\rho^{\Gamma_B} \equiv \sum_{i,j,k,l} \rho_{ij,kl} |i\rangle\langle j|_A \otimes (|k\rangle\langle l|_B)^T = \sum_{i,j,k,l} c_{ij,kl} |i\rangle\langle j|_A \otimes |l\rangle\langle k|_B$$

The complete transpose of this is

$$(\rho^{\Gamma_B})^T = \sum_{i,j,k,l} \rho_{ij,kl} (|i\rangle\langle j|_A)^T \otimes (|l\rangle\langle k|_B)^T = \sum_{i,j,k,l} c_{ij,kl} |j\rangle\langle i|_A \otimes |k\rangle\langle l|_B \equiv \rho^{\Gamma_A}$$

b) Clear by a) and by using lemma 2.1 and the fact that the eigenvalues of a square matrix A and A^T are equal. \square

The logarithmic negativity is very easy to calculate compared to other entanglement measures. It is enough to compute the square root of the eigenvalues of $(\rho^\Gamma)^\dagger \rho^\Gamma$ or the absolute sum of the eigenvalues of ρ^Γ . For practical and numeric calculations it is often more easy and stable to take a single eigenvalue than the need to compute the sum of multiple. For all numerical calculations in this thesis, I therefore opt for an alternative way to compute the logarithmic negativity.

Lemma 2.1. *The trace norm $\|A\|_1 \equiv \text{tr} \sqrt{A^\dagger A}$ of a hermitian matrix A is equal to the sum of the absolute eigenvalues of A .*

Proof. This can be immediately seen by the spectral decomposition $\lambda(A) = \{\lambda_1, \dots\}$:

$$\text{tr} \sqrt{A^\dagger A} = \text{tr} \sqrt{A^2} = \text{tr} \left\{ U \sqrt{\text{diag}(\lambda_1, \dots)^2} U^\dagger \right\} = \sum_i \sqrt{\lambda_i^2} = \sum_i |\lambda_i|.$$

\square

Proposition 2.3. *The negativity eq. (2.20) is given as the absolute sum of all negative eigenvalues of ρ^Γ :*

$$\mathcal{N}(\rho) \equiv \frac{\|\rho^\Gamma\|_1 - 1}{2} = \left| \sum_{\lambda_i < 0} \lambda_i \right|. \quad (2.22)$$

Proof. The proof is in parts given by Vidal and Werner [18]. It is known that the density matrix is hermitian: $\rho = \rho^\dagger$. Using lemma 2.1, the trace norm of the density matrix is given as $\|\rho\|_1 = \sum \lambda_i = \text{tr} \rho = 1$. The partial transpose ρ^Γ obviously also satisfies $\text{tr} \rho^\Gamma = 1$ but might have negative eigenvalues. Since ρ^Γ is still hermitian, the trace norm is given by

$$\|\rho^\Gamma\|_1 = \sum_i |\lambda_i| = \sum_{\lambda_i \geq 0} \lambda_i + \sum_{\lambda_i < 0} |\lambda_i| = \sum_i \lambda_i + 2 \sum_{\lambda_i < 0} |\lambda_i| = 1 + 2 \sum_{\lambda_i < 0} |\lambda_i|,$$

where in the last step $\sum \lambda_i = \text{tr} \rho^\Gamma = 1$ was used. \square

Remark. The PPT criterion states, that if ρ^Γ has negative eigenvalues, the state ρ is entangled. The negativity uses this criterion for a quantification of entanglement. This proposition makes sense of the name *negativity*.

Calculating the logarithmic negativity of the evolved state eq. (2.13), it is possible to quantify how the entanglement behaves in time. A straight forward computation following the calculation methods established above yields (for detailed calculations see appendix A.2)

$$E_N(|\psi(t)\rangle\langle\psi(t)|) = \log_2(1 + |\sin \Delta\phi|). \quad (2.23)$$

It is interesting to see, that the maximum entanglement $E_N = 1$ is reached for $\Delta\phi = 2\pi k \pm \pi/2$, $k \in \mathbb{Z}$ and no entanglement ($E_N = 0$) is measurable for $\Delta\phi = k\pi$. This result aligns with the previous observations by demanding that the evolved state eq. (2.13) is separable. The complete entanglement dynamics are shown in fig. 2.2. The time

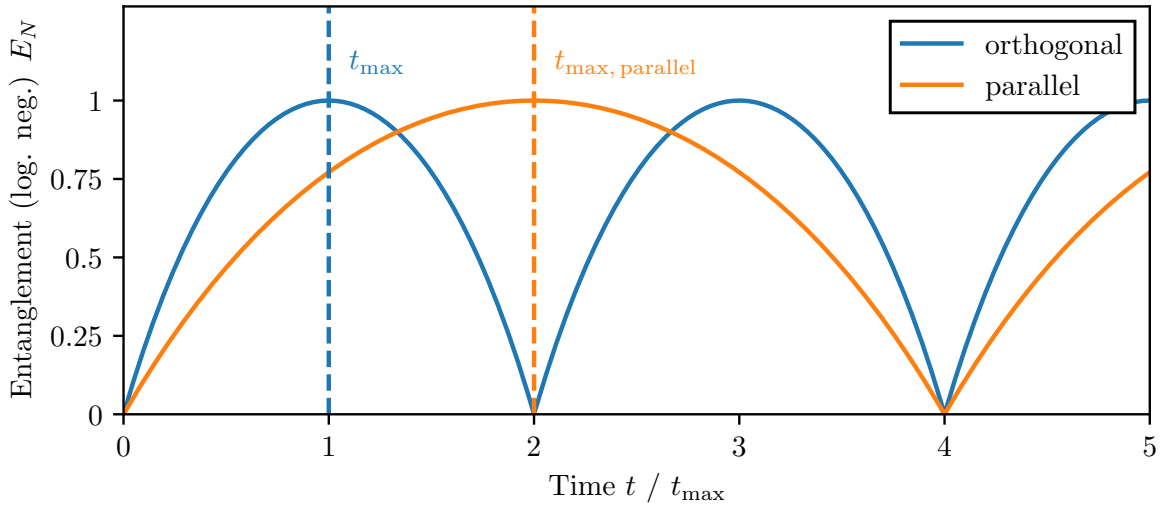


Figure 2.2: Entanglement dynamics quantified by the logarithmic negativity for two different orientations of the spatial superpositions. The parallel orientation was considered in this chapter (see eq. (2.23)), the “orthogonal” one in Ref. [10]. The time of maximum entanglement t_{\max} for the orthogonal configuration is reached after $t_{\max} = 4\pi\hbar L^3/(GM_A M_B \Delta x^2) \simeq 129$ ms.

$t_{\max, \text{parallel}}$ at which the entanglement is maximal (for the first time) can be calculated by using the definition of $\Delta\phi$ from eq. (2.15) as

$$t_{\max, \text{parallel}} = \frac{8\pi L^3 \hbar}{GM_A M_B (\Delta x)^2}. \quad (2.24)$$

In fig. 2.2 the entanglement dynamics for a different orientation considered in Ref. [10] is also shown. There, the superpositions are aligned in the same line as the direct connection between the masses (“orthogonal” to the parallel configuration before), maximizing the differences in distances between them and thus creating entanglement faster. This

expected behavior can be well seen in fig. 2.2: The time t_{\max} until the maximum entanglement is reached, is precisely by a factor of 2 faster than in the here considered parallel configuration [10]. For a practical experiment, this suggests that using the orthogonal orientation could be beneficial and would require shorter coherence times for the superpositions. To give an estimate, consider two identical silica spheres with a density of $\rho = 2648 \text{ kg/m}^3$ with a radius of $R = 10^{-5} \text{ m}$, a separation of $2L = 4R$ and a superposition size $\Delta x = 100 \text{ nm}$ (which is realistic considering theoretical sizes of up to micrometers [6]), the maximum entanglement is reached after about $t_{\max} \approx 129 \text{ ms}$ which is a quite long coherence time and challenging experimentally.

2.3 Issues with the idealized experimental procedure

For the realization of an experiment to measure quantum gravity induced entanglement of masses, one can only consider parameter spaces in which most of the expected and measured entanglement ultimately arises due to the gravitational interaction between the masses. Other forms of interactions and in particular electromagnetic forces have to be suppressed sufficiently. In particular, the short range **Casimir interactions** (chapter 3) have to be shielded as they induce a much greater attraction force than gravity at small separations. It is however not clear, that Casimir interactions can entangle real macroscopic masses at all as it is not even known whether the Casimir force field between bodies is conservative, although most researchers belief it is [20, 21]. As a estimation of the minimal separation distance L_{\min} , requiring that the gravitational potential should be stronger by a factor χ than the Casimir potential between the two massive spherical particles [22], the following inequality can be stated:

$$\chi |V_{\text{Casimir}}| \leq |V_{\text{Gravity}}| \quad (2.25)$$

$$\chi \times \frac{23\hbar c}{4\pi L^7} \left(\frac{\varepsilon_r - 1}{\varepsilon_r + 2} \right)^2 R^6 \leq \frac{GM^2}{L}. \quad (2.26)$$

Using $M = 4/3\pi R^3 \rho_{\text{Silica}}$, this results in a minimum separation distance independent of the size of the particles of

$$L_{\min} \geq \left(\chi \times \frac{207}{64} \frac{\hbar c}{\pi^3 G \rho_{\text{Silica}}^2} \right)^{1/6} \approx 140 \mu\text{m} \times \sqrt[6]{\chi}. \quad (2.27)$$

For the same particles used before, this would require very large measurement times of $t_{\max} \approx 90 \text{ s} \times \sqrt{\chi}$. It would therefore be beneficial to screen the Casimir interactions by placing a conducting Faraday shield between the particles so that they can be moved closer together [23]. Such a conducting shield would simultaneously shield all other forms of electromagnetic interactions such as Coulomb interactions, if the particles are charged.

This thesis is focused around the problem which arise by trying to measure the entanglement as a lot of individual measurements are required and it is virtually impossible to

ensure that each measurement started with identical initial conditions. Small variations in the placement of the particles can ultimately destroy the entanglement in the final averaged measurement result due to Casimir interactions between the particles and the newly placed shield. In chapter 4 this effect is studied in detail and the space of possible parameters for the particle-shield separation as well as for the superposition size and the particles mass is reduced. Thermal vibrations and noise due to the shield are considered in chapter 5

3 Casimir effect

Casimir forces can be viewed in a very similar way to the *van der Waals forces*. In fact, both phenomena describe just two different sides of the same coin. They define the so-called ***dispersion forces*** between neutral atoms or bodies. The quantum theory of van der Waals forces between two neutral atoms was developed by London in 1930 who found the attractive potential $\propto 1/r^6$ for small separations [24]. Casimir and Polder showed in 1948, that for separations larger than the resonance wavelength of the atoms, retardation effects need to be taken into account and the potential decays by a power law of $1/r^7$ [16]. Additionally, they calculated the interaction with a atom or molecule and a perfectly conducting plate, showing that macroscopic objects could experience these ***Casimir-Polder interactions*** as well. It becomes evident, that a full description of dispersion forces cannot be given by classical electrodynamics alone. Additional considerations regarding relativistic effects and quantum electrodynamics have to be made [25–27]. Casimir, following a suggestion by Bohr [28], found a simple derivation using the zero-point energy of the vacuum to calculate the attraction between two conducting plates. In quantum electrodynamics each point in the electromagnetic field can be described by an quantized harmonic oscillator with ground state energy $E_0 = \hbar\omega/2$. The total *zero-point energy* of the ground state of the field (the vacuum) is therefore given by summing over the energies E_0 for each possible mode n

$$E_{\text{vacuum}} = \frac{\hbar}{2} \sum_n \omega_n. \quad (3.1)$$

These sums are clearly divergent since there are infinitely many possible excitations. Electrostatic boundary conditions require the field to be zero at the surface of conductors restricting the possible modes between two parallel plates. Precisely the finite difference between the infinite vacuum energy with and without the macroscopic plates give rise to the ***Casimir forces***. Often, this divergence is simply dropped, motivated by the fact that energy is normally defined only up to a constant [25]. Casimir was able to use regularization techniques to deal with the infinite quantities and arrived at his famous formula [15]

$$E_{\text{Casimir}} = -\frac{\hbar c \pi^2}{720 L^3} A \quad (3.2)$$

for the attractive Casimir-potential between two plates with surface area A and separation L . The attractive force $F = -\nabla E$ between the plates can now be simply expressed as

$$F_{\text{Casimir}} = -\frac{\hbar c \pi^2}{240 L^4} A. \quad (3.3)$$

3 Casimir effect

It is remarkable, that such a simple relation arises out of the infinities of the vacuum. To this day, these Casimir forces are a major topic of modern scientific research. They are generally very difficult to calculate for geometries other than two infinitely large plates or for real materials with dielectric properties. For simple geometries, even the sign of the force is not always intuitively clear: As an example, the Casimir force can be repulsive for an ideal metal spherical shell [26]. Between other simple and important objects like the sphere-plane or sphere-sphere geometry, no universally valid closed formula for any separation L/R between the bodies exists. This is discussed in more detail in section 3.2.

Almost ten years after the discovery of Casimir and Polder, Lifshitz was the first to find an expression for the Casimir force between two dielectric plates with arbitrary relative permittivity $\varepsilon_{r,1,2}$ for separations larger than the resonant wavelength⁵ [30]. The expression he found facilitates the general complexity of the Casimir interactions and is only expressible as a complicated integral [30]

$$F/A = -\frac{\hbar c}{32\pi^2 L^4} \int_0^\infty dx \int_1^\infty dp \frac{x^3}{p^2} \left\{ \left[\frac{(s_1 + p)(s_2 + p)}{(s_1 - p)(s_2 - p)} e^x - 1 \right]^{-1} + \left[\frac{(s_1 + \varepsilon_{r,1}p)(s_2 + \varepsilon_{r,2}p)}{(s_1 - \varepsilon_{r,1}p)(s_2 - \varepsilon_{r,2}p)} e^x - 1 \right]^{-1} \right\} \quad (3.4)$$

with

$$s_{1,2} = \sqrt{\varepsilon_{r,1,2} - 1 + p^2}.$$

In the limit of two perfectly conducting plates ($\varepsilon_{r,1} = \varepsilon_{r,2} \rightarrow \infty$), the integral can be solved analytically resulting in the same expression already obtained by Casimir

$$F_{\text{cond.}}/A = -\frac{\hbar c}{16\pi^2 L^4} \int_0^\infty dx \int_1^\infty dp \frac{x^3}{p^2(e^x - 1)} = -\frac{\hbar c\pi^2}{240L^4}. \quad (3.5)$$

Lifshitz determined the Casimir force between a conducting metal plate and a dielectric plate (denoted DM) as well as the force between two dielectric plates with the same dielectric constant ε_r (DD) as

$$F_{\text{DM}} = -\frac{\hbar c\pi^2}{240L^4} \frac{\varepsilon_r - 1}{\varepsilon_r + 1} \varphi(\varepsilon_r) \quad (3.6)$$

$$F_{\text{DD}} = -\frac{\hbar c\pi^2}{240L^4} \left(\frac{\varepsilon_r - 1}{\varepsilon_r + 1} \right)^2 \varphi(\varepsilon_r) \quad (3.7)$$

where $\varphi(\varepsilon_r)$ is a numerical function obtained by solving eq. (3.4), which approaches 1 for a perfect conductor [30]. I calculated the function numerically and the result is shown in fig. 3.1. For a dielectric and metal plate, the function φ approaches the finite value $\varphi(\varepsilon_r \rightarrow 1) \approx 0.46$ for small dielectric constants. This limit is practically already reached at $\varepsilon_r \approx 4$ and φ stays approximately constant for smaller ε_r .

⁵The “resonance wavelength” for a macroscopic body in this case can be understood as e.g. the plasma frequency in the Drude model [29]. Different models for light-matter interaction result in slightly different resonant wavelength. The Lifshitz formula however holds true for the cases of separations in the micro-meter regime for all practical materials [23].

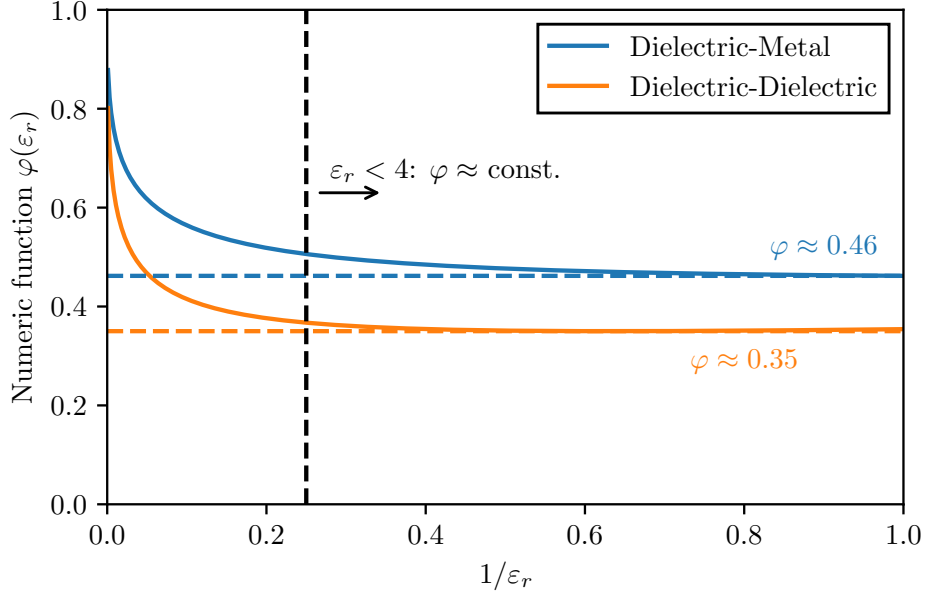


Figure 3.1: Numeric calculations of the function $\varphi(\varepsilon)$ used in the Lifshitz formula eq. (3.6) and (3.7). The function was calculated for **(blue)** a dielectric and a metal plates and **(orange)** two dielectric plates. The function approaches unity for $\varepsilon_r \rightarrow \infty$ and a finite value for $\varepsilon_r \rightarrow 1$.

3.1 Proximity force approximation

The Casimir-Polder force cannot be computed easily for arbitrary shapes. There even exists no analytic expression for the simple (and for this thesis relevant) plate-sphere geometry for all separations L/R . For a general shape, even the sign of the force, i.e. whether it is attractive or repulsive, is often unknown [26]. Fortunately, approximation methods exist and in particular the **proximity-force-approximation (PFA)** can be calculated very easily [31–33]. The PFA is only valid for small separations ($L/R \approx 1$) between the considered smooth bodies, where R is the size of the bodies i.e. the radius of the sphere for the sphere-plate geometry. The idea of this approximation is to divide the surfaces of the two bodies into infinitesimal small parallel plates with area dA and summing over the forces dF (or the Casimir-energy dE) between them (see fig. 3.2):

$$E_{\text{PFA}} = \iint_A dA \frac{E_{\text{plate-plate}}}{A} \quad (3.8)$$

where for the casimir energy per unit area $E_{\text{plate-plate}}/A$ either eq. (3.2) or any of the Lifshitz equations (3.7), (3.6) can be used. For the following calculations, it is important to distinguish between the distance between the plates center and the spheres center L (like used before) and the edge-to-edge distance $\mathcal{L} = L - R$.

The problem with this approximation is, that it is ambiguous, what surface the area element dA represents. For the plate-sphere geometry, the element can be either chosen

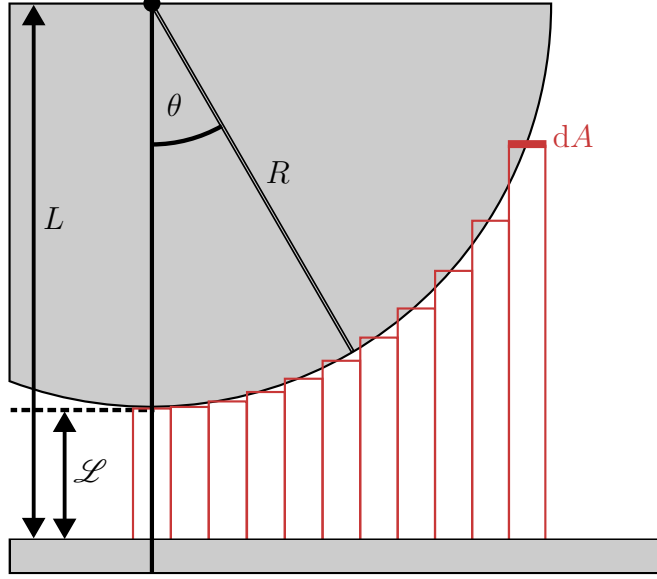


Figure 3.2: In the proximity force approximation the sphere is divided into infinitesimal plane areas dA which all exert a force dF according to eq. (3.3). All the contributions are added up together.

tangential to the sphere or parallel to the plate (or in theory any other fictitious surface somewhere in between) [33]. For the plate-sphere geometry, in the limit of the validity of the PFA $\mathcal{L} \ll R$ both methods yield the same result. For the following calculations, I choose dA parallel to the plate and the area can be parameterized with $r \in [0, R]$ and $\varphi \in [0, 2\pi]$ resulting in a distance z between the infinitesimal area elements $z(r) = \mathcal{L} + R - \sqrt{R^2 - r^2}$ ⁶. The PFA eq. (3.8) then yields for a dielectric sphere against a perfectly conducting plate

$$E_{\text{plate-sphere}} = -\frac{\hbar c \pi^2}{720} \left(\frac{\varepsilon_r - 1}{\varepsilon_r + 1} \right) \varphi(\varepsilon_r) \int_0^R dr \int_0^{2\pi} r d\varphi \frac{1}{z(r)^3} \quad (3.9)$$

$$= -\frac{\hbar c \pi^3}{360} \left(\frac{\varepsilon_r - 1}{\varepsilon_r + 1} \right) \varphi(\varepsilon_r) \frac{R^2}{2\mathcal{L}^2(R + \mathcal{L})} \quad (3.10)$$

$$\approx -\frac{\hbar c \pi^3}{720} \left(\frac{\varepsilon_r - 1}{\varepsilon_r + 1} \right) \varphi(\varepsilon_r) \frac{R}{\mathcal{L}^2} \quad (3.11)$$

⁶Taking dA tangential to the sphere, it can be parameterized with $\theta \in [0, \pi/2]$ and $\varphi \in [0, 2\pi]$ resulting in $z(\theta) = \mathcal{L} + R - R \cos \theta$. The PFA eq. (3.8) yields with $dA = R^2 \sin \theta d\theta d\varphi$ the result $\propto \frac{\pi R^2 (R + 2\mathcal{L})}{\mathcal{L}^2 (R + \mathcal{L})^2}$ which in the limit of $\mathcal{L} \ll R$ results in the same expression as eq. (3.11).

3.2 Casimir forces between a conducting plate and a dielectric sphere

An empirical derivation for power law of the casimir energy between a sphere and a conducting plate can be made directly from the energy between two atoms with static polarizability α_i given by Casimir and Polder [16]. They derived an expression for the Casimir-Polder potential of ⁷

$$E = -\frac{23\hbar c\alpha_1\alpha_2}{4\pi L^7}. \quad (3.12)$$

The polarizability of a sphere with radius R is derived in appendix B.1 and is given for an dielectric with ε_r as

$$\alpha_{\text{sphere}} \propto \left(\frac{\varepsilon_r - 1}{\varepsilon_r + 2} \right) R^3. \quad (3.13)$$

If one atom is now replaced by a conducting sphere ($\varepsilon_r \rightarrow \infty$) of radius $\sim L$ (much larger than the atom) with a polarizability of L^3 , it get obvious that between this big sphere and the atom, the energy is given by a power law of $1/L^4$. It is therefore natural to assume, that for a macroscopic sphere and a macroscopic plate, the Casimir energy behaves similar to a $1/L^4$ law - at least for the **large separation limit (LSL)**. The exact calculation for this problem is very hard. In fact, no analytic solution is known.

Ford was able to determine an integral expression using a macroscopic approach in 1998 [29]:

$$F = -\frac{\hbar c}{4\pi L^4} \int_0^\infty d\omega \alpha(\omega) [3 \sin 2\omega L - 6L\omega \cos 2\omega L - 6L^2\omega^2 \sin 2\omega L + 4L^3\omega^3 \cos 2\omega L]. \quad (3.14)$$

The expression depends on the polarizability, which is generally not constant for a dielectric. Especially for small separations between the sphere and the plate, this dependence and the non-constant polarizability make this integral nearly unsolvable. For large separations, much larger than the absorption wavelength of the dielectric or much larger than the wavelength corresponding to the plasma frequency in the Drude-Model, the polarizability can be assumed to be static $\alpha = \text{const}$ [23, 29]. In this simplifying case, the integral can be solved using an exponential convergence factor and results in

$$F = -\frac{6\hbar c}{4\pi L^5} \alpha \quad (3.15)$$

and thus

$$E = -\frac{3}{8} \frac{\hbar c}{\pi L^4} \left(\frac{\varepsilon_r - 1}{\varepsilon_r + 2} \right) R^3. \quad (3.16)$$

⁷For two macroscopic spheres, the casimir potential looks very similar to eq. (3.12). The polarizability of a sphere is given by eq. (3.13). Using this result, the Casimir energy between two identical dielectric spheres in the large separation limit is given as $-\frac{23\hbar c}{4\pi L^7} \left(\frac{\varepsilon_r - 1}{\varepsilon_r + 2} \right)^2 R^6$ [22].

For the large separations, the Casimir interaction between a sphere and a plate indeed behaves like expected compared with the motivation of the $1/L^4$ -law above in this section.

A second method to calculate the Casimir energy for arbitrary compact objects and a conducting wall was developed in Ref. [22]. For the sphere-plate geometry, this results in the large separation limit (LSL) in a infinite series, where the first-order term ($\propto 1/L^4$) is precisely given by eq. (3.16) [32, 34]. The first 8 terms of this series are shown in fig. 3.3 as well as a few specific numerical points for higher terms. It becomes evident,

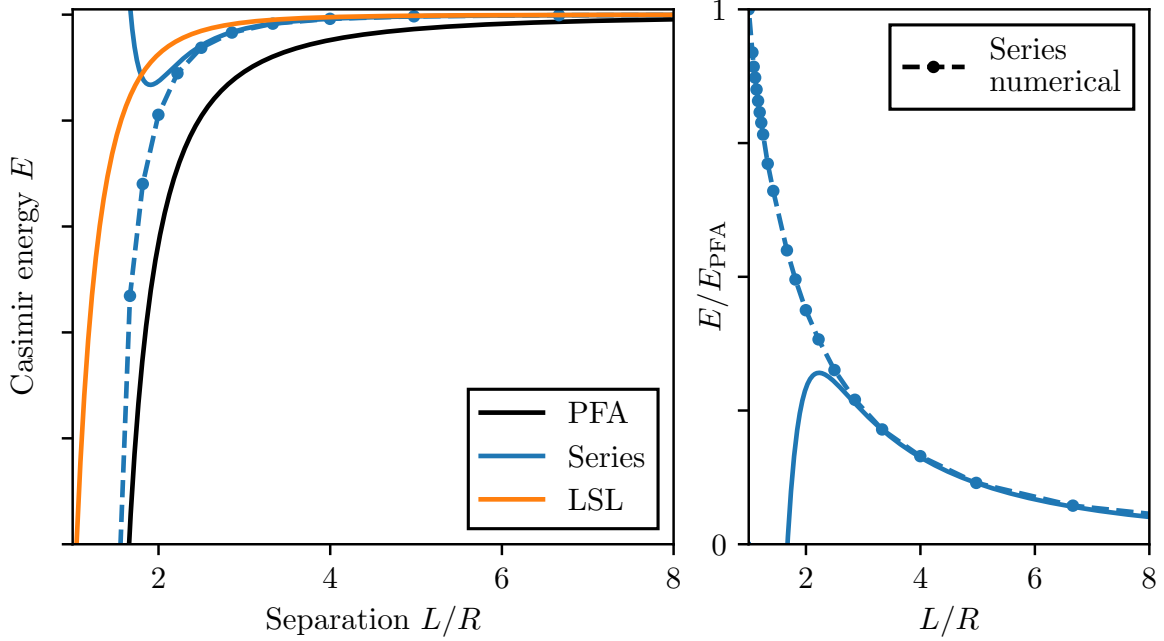


Figure 3.3: Behavior of different approximations of the casimir interaction between a conducting sphere and a perfectly conducting plate. Additionally, a comparison between the PFA and an exact numerical series expansion from Ref. [32] is shown.

that the series expansion converges to the LSL eq. (3.16) for large separations and to the PFA eq. (3.11) for small separations. However, quantitatively the numerics show, that $E/E_{\text{PFA}} \leq 1$ and thus the PFA predicts a stronger Casimir energy for all separations.

Theorem 3.1. *The PFA model for the Casimir energy between a conducting sphere and a conducting plate is an upper bound for the actual Casimir potential for any separation L/R .*

Proof. The proof is given in the following two steps: First it is shown that **(a)** $|E_{\text{PFA}}| > |E_{\text{LSL}}|$ for arbitrary dielectric spheres, then it is shown that **(b)** $|E_{\text{PFA, cond.}}| \geq |E_{\text{PFA, diel.}}|$.

Using the numerical series expansion in fig. 3.3 it is clear that this argumentation holds for all separations L/R .

(a) Directly comparing the PFA eq. (3.11) and the LSL eq. (3.16) shows

$$|E_{\text{PFA}}| > |E_{\text{LSL}}| \quad (3.17)$$

$$\frac{\hbar c \pi^3}{720} \left(\frac{\varepsilon_r - 1}{\varepsilon_r + 1} \right) \varphi(\varepsilon_r) \frac{R}{\mathcal{L}^2} > \frac{3\hbar c}{8\pi L^4} \left(\frac{\varepsilon_r - 1}{\varepsilon_r + 2} \right) R^3 \quad (3.18)$$

$$\frac{8\pi^4}{3 \cdot 720} \frac{\varepsilon_r + 2}{\varepsilon_r + 1} \varphi(\varepsilon_r) > \frac{(L - R)^2 R^2}{L^4} = \left(\frac{R}{L} \right)^2 - 2 \left(\frac{R}{L} \right)^3 + \left(\frac{R}{L} \right)^4 \quad (3.19)$$

However, comparing the maximum of the RHS at $1/16$ (for $R/L = 1/2$) and the minimum of the LHS, this inequality holds. The terms $(\varepsilon_r + 2)/(\varepsilon_r + 1) > 1$ and $\varphi(\varepsilon_r) \geq 0.46$ are bound. Thus the minimum of the LHS is bounded above $\approx 0.166 > 1/16$.

(b) For $\varepsilon_r \in [1, \infty)$, both $\varphi(\varepsilon) < 1$ and $(\varepsilon_r + 2)/(\varepsilon_r - 1) < 1$ are bounded, resulting trivially in $|E_{\text{PFA, cond.}}| \geq |E_{\text{PFA, diel.}}|$. \square

Remark. For later calculations, only the difference in the Casimir energy for slightly different separations L and thus effectively the gradient $\nabla E_{\text{Casimir}}$ is required. The same arguments as above can be made to see that the gradient of the PFA is an upper bound for all separations as well.

During the rest of the thesis, I therefore opt for the use of the proximity force approximation as a worst-case estimation. If it is appropriate, I will compare both Casimir models - the PFA and the LSL.

3.3 Imperfect plate and spheres

In reality, the plate and/or the spheres are not perfectly flat and the surfaces are strewn with imperfections. This leads to small and local changes in the sphere-plate separation and thus to a marginally altered Casimir interaction. Due to symmetry it is enough to only consider a imperfect plate and a perfectly smooth sphere as the Casimir interactions in the proximity force approximation (PFA) solely depend on the separation \mathcal{L} . To quantify and estimate the changes in the Casimir force due to these surface irregularities, a selection of different and relevant forms of imperfections with amplitude $\Delta\mathcal{L}$ shown in fig. 3.4 have been studied with numerical methods.

- (a) A *gaussian deformation* of the plate can be used to describe a range of possible local imperfections in the size of the sphere. For a small shield in the size of the spheres ($r_s \approx R$) thermal vibrations look very similar to these deformations, as discussed in chapter 5. A positive and negative displacement in the form of a gaussian function is considered.
- (b) For the description of large and thus linearizable imperfections (like thermal excitations in on a large shield $r_s \ll R$), a *linear deflection* is used. This deflection

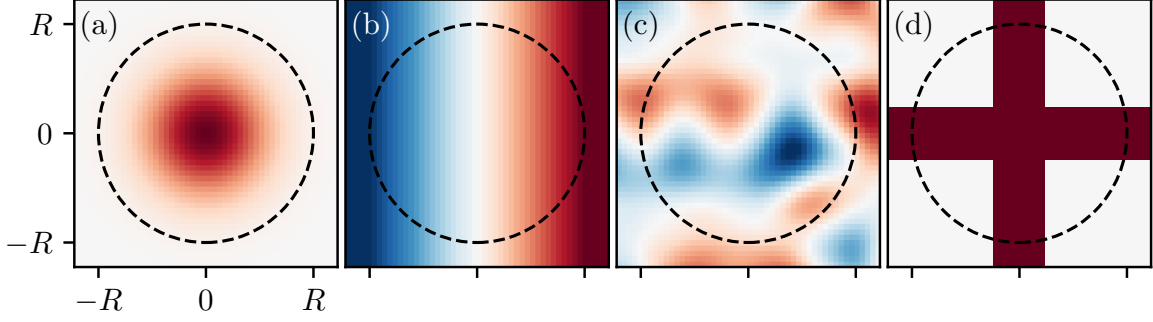


Figure 3.4: A selection of imperfect plates. **(a)** A simple gaussian deformation in the same size as the sphere. **(b)** Linearly inclining plate or a tilted flat plate. **(c)** Uneven and noisy but uniformly random surface realized using *Perlin noise* [35]. **(d)** A cross-shape in the center of the plate.

can be also understood as a tilted plate in front of the sphere where one side is much closer to the sphere than the other. For small tilting angles these variations in the Casimir interaction cancel out in first order and one expects no significant change in the total attraction force.

- (c)** Similarly neglectable should therefore be random noisy but uniformly distributed deformations which are here qualitatively given by the *Perlin noise* function [35]. This type of noise is commonly used in computer science and produces a uniform smooth pseudo-random noise that is often used to imitate surface roughness [35]. Equidistant grid-points are defined, each of which is assigned with a pseudo-random gradient. The noise function follows this gradient in the vicinity of a grid-point and interpolation between points generates smooth transitions. Due to the uniformness, no large deviations from an ideal flat plate is expected.
- (d)** A structure on the shield, like e.g. a *centered cross* might improve stability and rigidity of the shield. Thermal vibrations could be reduced by such a design but the effect and amplification of the Casimir interaction has to be investigated.

The resulting Casimir potentials between a macroscopic sphere and the imperfect surfaces were numerically calculated in the PFA and are shown in fig. 3.5. As logically expected, all variations are upper bounded by moving the ideal flat plate closer (or farther) to the sphere by a distance $\Delta\mathcal{L}$. For the gaussian distribution, the overestimation is not particularly large. An evenly tilted plate as well as a uniformly noisy plate do not change the Casimir interactions noticeably even at small separations. If the plate and sphere are far separated ($\mathcal{L} \gg R$) all local imperfections are neglectable as the relative effect of them decreases and gets less noticeable. But especially for small shields in the size of the particle and close separations, the considerations performed in this section are important.

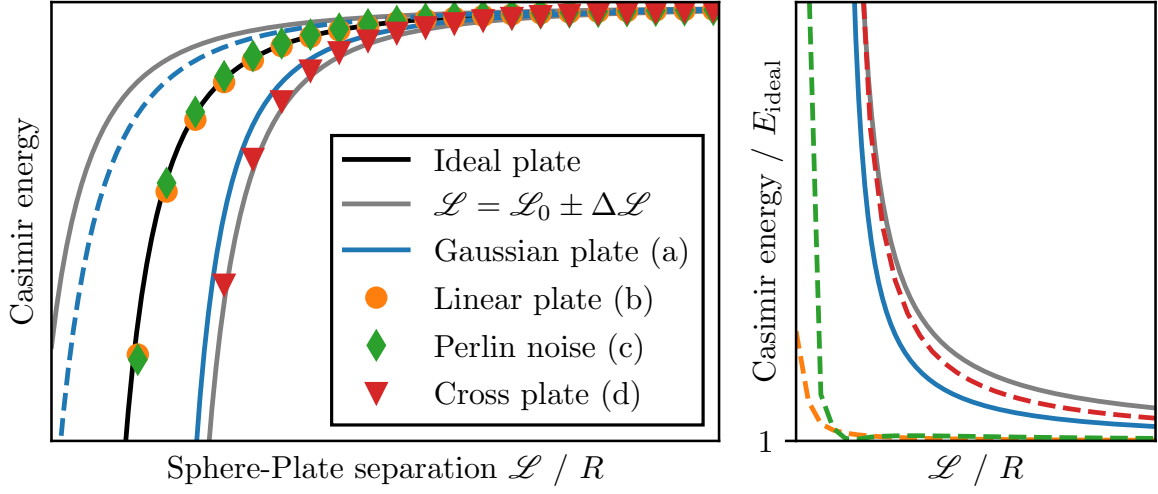


Figure 3.5: Casimir energy for the different imperfect plates shown in fig. 3.4. The dashed-blue line represents a negative gaussian displacement reducing the overall Casimir attraction. The shaded region is given by an ideal plate separated by a distance of $\mathcal{L}_0 \pm \Delta\mathcal{L}$ from the sphere where \mathcal{L}_0 is the original separation. It becomes evident that in the limit of $\mathcal{L} \rightarrow \infty$, all local imperfections are neglectable.

4 The particle in front of a static shield

The generalized setup of the system described in chapter 2 with the addition of a conducting Faraday shield is shown in fig. 4.1. As before, the particles A and B are delocalized in cat-states with superposition sizes Δx_A and Δx_B respectively. The superpositions

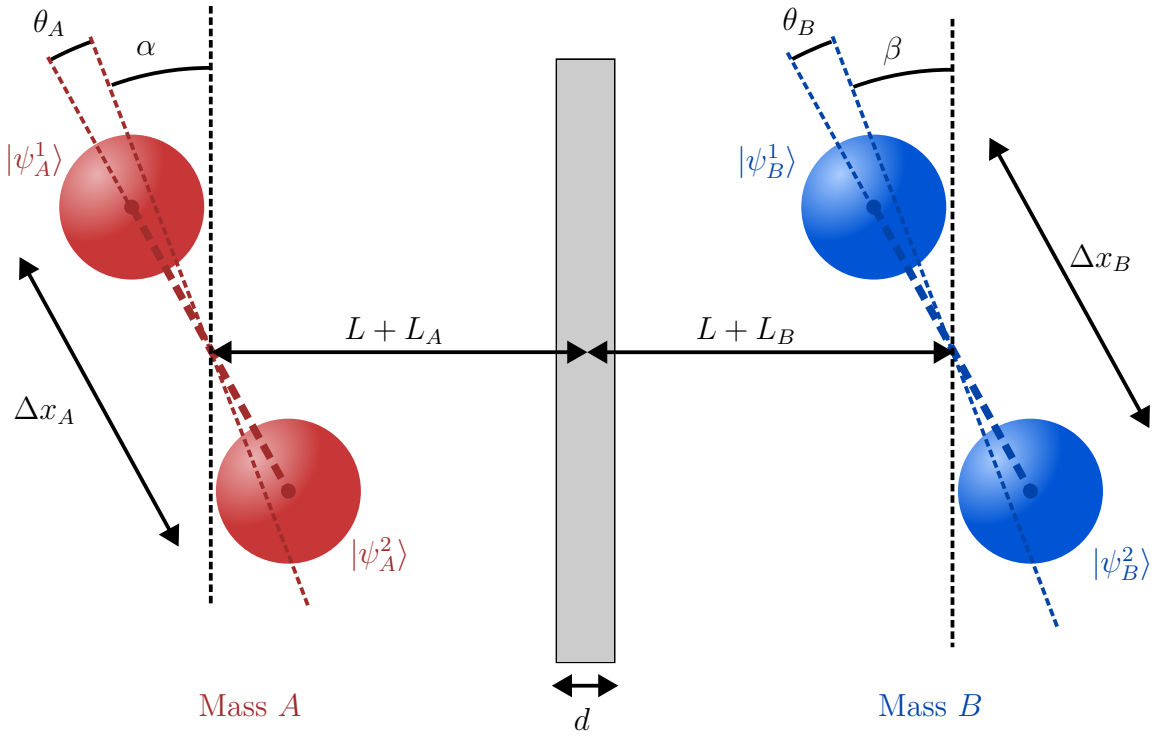


Figure 4.1: Schematic depiction of a experimental setup for the detection of gravitationally induced entanglement between two particles A and B with radius R . They are separated by a distance of $2L + L_A + L_B$ in arbitrary orientations given by the angles α and β with small variations $\theta_{A(B)}$. All variations are assumed to be normally distributed around mean zero with standard deviation $\Delta L_{A(B)}$ and $\Delta \theta_{A(B)}$. The particles are delocalized in a cat state with a separation $\Delta x_{A(B)}$ between the states $|\psi_{A(B)}^1\rangle$ and $|\psi_{A(B)}^2\rangle$. A conducting Faraday shield with thickness d is placed in the center between the particles.

are extended in arbitrary orientations $\alpha, \beta \in [0, \pi)$ a distance L away from the shield. Most notably, the configuration of $\alpha = \beta = 0$ represents the same “parallel orientation” discussed earlier in chapter 2. In the following, the case of $\alpha = \beta = \pi/2$ is referred to as the “orthogonal orientation”. If gravity is assumed to be able to mediate entanglement, the above system can generate entanglement between both particles A and B due to their mutual gravitational interaction. Placing a Faraday shield in the center between the masses should not substantially influence the gravitational entanglement generation. However, Casimir interactions between the shield and the masses are still present at small separations. It is straightforward to convince yourself that these interactions can only give rise to local phases for each cat-state, dependent only on their associated particle-shield separations $L_{A(B)}^i$ ($i = 1, 2$). Such local interactions can - assuming a static shield e.g. at zero temperature - not induce any additional entanglement between the masses.

For a complete picture, one has to consider experimental challenges and limitations in a real experiment. Measuring the states after some time to determine their entanglement requires knowledge of the states which can be obtained by e.g. **full state tomography**. Some proposals aim at measuring entanglement by means of a suitable witness [4, 6], but the generation of such an entanglement witness requires insight into the specifics of the experimental realization. In this thesis, I will focus on the most general and universally applicable case of measuring the complete density matrix of the system and checking for entanglement using a convenient entanglement measure like the “logarithmic negativity” [19] introduced in section 2.2. The density matrix of a 2 qubit system consists of 16 different entries (only 9 of them are independent⁸). For a full tomography, a lot of measurements of the system have to be made to determine the state in the required precision. During these measurements, engineering challenges of recreating the identical initial conditions, i.e. the placement of the particles in each consecutive run have to be considered. But even if it was somehow possible to place the particle at the *exact* same position each measurement, thermal vibrations of the shield induce small noisy variations in the shield-particle separation over a lot of runs.

Thus even if the masses get entangled in each run of the measurement, the measured results might differ slightly due to the varying initial placements of the particles resulting in a final measurement that looks like a mixed state

$$\rho = \int_{-\infty}^{\infty} dX \frac{1}{\sqrt{2\pi}\Delta X} e^{-X^2/2(\Delta X)^2} |\psi_X\rangle\langle\psi_X|. \quad (4.1)$$

Here, $|\psi_X\rangle$ is the pure state of a single measurement dependent on the random variable $X = \{\theta_{A(B)}, L_{A(B)}\}$ corresponding to placement inaccuracies between multiple measurements. These variations are assumed to be normally distributed with mean $\langle X \rangle = 0$ and standard deviation ΔX on the basis of the central limit theorem [36, p. 1195]. In some cases, as for example if the plate is not placed exactly in the center or at a tilt, the

⁸Using the known characteristics of the density matrix like hermiticity $\rho^\dagger = \rho$ and $\text{tr } \rho = 1$, it is possible to reconstruct ρ from only 9 specific entries.

variations $\theta_{A(B)}$ and $L_{A(B)}$ are correlated and $L_A = -L_B$ holds true. In the most general case, all placement variations are assumed to be independent and are drawn from their respective probability distribution.

Convergence for a finite number of measurements

Experimentally, it would be very interesting to know how fast the averaged density matrix $\bar{\rho}$ after a finite number of $\#$ measurements converges to the idealized asymptotic mean $\langle \rho \rangle$ given by eq. (4.5), which is calculated and analyzed in depth in the next two sections. After $\#$ measurements, the sample average is given by

$$\bar{\rho} = \frac{1}{\#} \sum_{k=1}^{\#} \rho(X_k) \quad (4.2)$$

where $\rho(X)$ depends on the random variable $X \in \{\theta_{A(B)}, L_{A(B)}\}$ and X_k is the k -th sample drawn from the normal distribution $\mathcal{N}(0, (\Delta X)^2)$ ⁹. As $\# \rightarrow \infty$, the law of large numbers and in particular the central limit theorem (CLT) ensures that $\bar{\rho} \rightarrow \langle \rho \rangle$ [36, p. 1195]. According to the CLT, the sample average $\bar{\rho}(X)$ fluctuates around $\langle \rho \rangle$ with a standard deviation given by the Berry-Esseen theorem for independent and identically distributed random variables X_k by $\sigma \sim \#^{-1/2}$ [37]. Thus, if the placements of the particles in each measurement are completely independent from each other, the rate of convergence to the ideal mean $\langle \rho \rangle$ is governed by $\mathcal{O}(1/\sqrt{\#})$.

It is however very likely that measurements are mostly performed consecutively in the same trap so that the placements in successive measurements are correlated. This correlation $\text{Cov}[\rho(X_i), \rho(X_j)] = c_{|i-j|}$ between the i -th and j -th measurement should therefore decrease with increasing $|i-j|$. The variance of $\bar{\rho}$ is now dependent of these correlations in the form [36, p. 1227]

$$\text{Var}[\bar{\rho}] = \frac{1}{\#^2} \sum_{i,j=1}^{\#} \text{Cov}[\rho(X_i), \rho(X_j)] = \frac{1}{\#} \text{Var}[\rho] + \frac{2}{\#^2} \sum_{n=1}^{\#-1} (\# - n) c_n \quad (4.3)$$

where $\text{Cov}[\rho, \rho] = \text{Var}[\rho]$ was used for the variance of the mean density matrix $\langle \rho \rangle$. For correlations $c_n \sim n^{-\alpha}$ ($\alpha < 1$) the sum in eq. (4.3) scales like

$$\sum_{n=1}^{\#-1} (\# - n) n^{-\alpha} \xrightarrow{\# \rightarrow \infty} \int_1^{\#} dn (\# - n) n^{-\alpha} \sim \#^{2-\alpha} \quad (4.4)$$

which results in $\text{Var}[\bar{\rho}] \sim \#^{-\alpha}$. In the asymptotic limit the standard deviation of the sample average $\sqrt{\text{Var}[\bar{\rho}]}$ and thus in a convergence rate to the mean $\langle \rho \rangle$ scales with $\mathcal{O}(1/\sqrt{\#}^{\alpha})$. This convergence is arbitrary slow for small α (if the setup does not change

⁹Here it isn't strictly required that X_k are normally distributed. As long as they are i.i.d. random variables, any distribution is sufficient for the following argumentation [36, p. 1195].

a lot between individual measurements) and thus the following calculations are just a worst-case estimation of the actual experimental results. If a weaker correlation in the form of $c_n \sim e^{-\alpha n}$ is used, the convergence rate is again asymptotically governed by $\mathcal{O}(1/\sqrt{\#})$.

4.1 Entanglement generation

If the state ρ is reconstructed using repeated measurements, but the initial placement of the particles were slightly different for each measurement, this is effectively comparable to an averaging process over all variations of the initial parameters in the setup. As mentioned above, this averaging results in a mixed state and for large variations $\Delta\theta$ and ΔL this process can destroy entanglement. To see this, I calculate the effective measured state $\langle\rho\rangle$ using

$$\langle\rho\rangle = \int_{-\infty}^{\infty} d\theta_A p(\theta_A) \int_{-\infty}^{\infty} d\theta_B p(\theta_B) \int_{-\infty}^{\infty} dL_A p(L_A) \int_{-\infty}^{\infty} dL_B p(L_B) \rho(\theta_A, \theta_B, L_A, L_B) \quad (4.5)$$

where $p(\cdot)$ is the gaussian probability distribution. Both θ and L are distributed normally with mean 0 and standard deviation $\Delta\theta$ or ΔL respectively. $\rho(\theta_A, \theta_B, L_A, L_B)$ is the state of a single measurement, dependent on the initial parameters $\theta_{A(B)}$ and $L_{A(B)}$ of the setup. The initial state ρ_0 at $t = 0$ is given similarly as before by eq. (2.7) at the beginning of chapter 2. During the time evolution, not only the mutual gravitational interaction between the particles must be taken into account, but also the dephasing due to the Casimir interaction between the particles and the Faraday shield. A single superposition state $|\psi_{A(B)}^i\rangle$ ($i = 1, 2$) accumulates the phase $\phi_{A(B), \text{Cas}}^i(t)$ during time evolution due to the casimir interaction where the phases are given by

$$\phi_{A(B), \text{Cas}}^i(t) = \frac{t}{\hbar} \begin{cases} \frac{3\hbar c}{8\pi} \left(\frac{\varepsilon_r - 1}{\varepsilon_r + 2} \right) \frac{R^3}{(L_{A(B)}^i)^4} & \text{for large separations (LSL)} \\ \frac{\hbar c \pi^3}{720} \varphi(\varepsilon_r) \left(\frac{\varepsilon_r - 1}{\varepsilon_r + 1} \right) \frac{R}{(\mathcal{L}_{A(B)}^i)^2} & \text{for small separations (PFA)} \end{cases} \quad (4.6)$$

Here, both analytical limits of the Casimir interaction discussed in chapter 3 have been used. The particle-shield separations $L_{A(B)}^i$ and $\mathcal{L}_{A(B)}^i = L_{A(B)}^i - R$ are dependent on the initial (varying) positions of each particle. In full generality, they are given by

$$L_{A(B)}^i = L + L_{A(B)} - \frac{d}{2} \pm \frac{\Delta x_{A(B)}}{2} \sin(\delta + \theta_{A(B)}) \quad (4.7)$$

where \pm distinct between $i = 1$ and $i = 2$ and $\delta = \alpha, \beta$ was used as an abbreviation. The mutual gravitational interaction of the state $|\psi_A^i\rangle \otimes |\psi_B^j\rangle$ is given similar to before by the accumulated phase

$$\phi_{\text{Grav}}^{ij}(t) = \frac{t}{\hbar} \frac{GM_A M_B}{L^{ij}}. \quad (4.8)$$

The separation distance L^{ij} between the states A_i and B_j in full generality is given by

$$L^{ij} = \sqrt{\left(2L + L_A + L_B \pm \frac{\Delta x_A}{2} \sin(\alpha + \theta_A) \mp \frac{\Delta x_B}{2} \sin(\beta + \theta_B)\right)^2 + \left(\frac{\Delta x_A}{2} \cos(\alpha + \theta_A) \pm \frac{\Delta x_B}{2} \cos(\beta + \theta_B)\right)^2}. \quad (4.9)$$

Expanding the accumulated gravitational- and Casimir phases to first order in $\Delta x_{A(B)} \ll L$, $\theta_{A(B)} \ll 1$ and $L_{A(B)} \ll 1$ (which is possible since all these variations are very small, as seen later), the averaging of the evolved state $\langle \rho \rangle$ eq. (4.5) can be performed analytically (for an exemplary calculation see appendix D). It turns out that with $\Delta\theta_A = \Delta\theta_B \equiv \Delta\theta$ and $\Delta L_A = \Delta L_B \equiv \Delta L$ all off-diagonal elements of the averaged state $\langle \rho \rangle$ (the so-called **coherences**) are given in the form

$$\langle \rho_{kl} \rangle = \frac{1}{4} e^{i\Delta\phi_{kl}(t)} \exp\left\{-\frac{(\Delta\theta)^2}{2} (\Delta\phi_{kl,\theta})^2 t^2\right\} \exp\left\{-\frac{(\Delta L)^2}{2} (\Delta\phi_{kl,L})^2 t^2\right\} \quad (4.10)$$

where all $\Delta\phi$ -terms are substitutes for rather lengthy phase expressions that depend on the particle-shield separation L , the orientation of the cat-state α, β , the masses of the particles $M_{A(B)}$ and the superposition size $\Delta x_{A(B)}$. It becomes evident that for large times $t \rightarrow \infty$ or for large variations in the placement $\Delta\theta, \Delta L \rightarrow \infty$ these off-diagonal elements tend to zero which leads to a continuous and monotonic loss of purity, resulting in the maximally mixed state $\text{tr} \rho^2 = 1/4$ - which obviously is not entangled. For large variations in the placement of the particles, one therefore expects the loss of coherence and thus of entanglement.

The resulting logarithmic negativity of the averaged state $E_N(\langle \rho \rangle)$ was computed numerically for different values of $\Delta\theta$ and ΔL and is shown in fig. 4.2. For this figure, the parallel orientation $\alpha = \beta = 0$ was used at times relative to the time of maximum entanglement t_{\max} from eq. (2.24). The radius of the particles was set to $R = 1 \times 10^{-5}$ m with corresponding mass $M_A = M_B = 4/3 \pi R^3 \rho_{\text{Silica}} \approx 1.1 \times 10^{-11}$ kg. A particle-shield separation of $L = 2R$ and a superposition size of $\Delta x_A = \Delta x_B = 100$ nm were chosen. In the rest of the thesis, if not otherwise specified, these parameters are used as a default. They are chosen in the specific orders of magnitude, because they result in a feasible low experiment-time $t_{\max} \approx 258$ ms and are in the region of what is soon¹⁰ possible [38]. It is important however to stress out, that all these parameters are orders of magnitude away from what is experimentally reachable today. The largest mass that was studied in matter-wave interferometry is in the order of 4×10^{-23} kg [13] with an superposition size of $\Delta x \gtrsim 500$ nm. For solid state mechanical systems quantum control and in particular groundstate cooling up to masses in the order of 10^{-13} kg [39], 10^{-11} kg [40] and 10^{-8} kg [41] with very short coherence times $\lesssim 1 \mu\text{s}$ have been demonstrated. On the contrary, the smallest mass with a measurable gravitational coupling is around 92 mg [14]. Levitated particles combine the best of both world with quantum control of large and heavy trapped solid objects as well as long coherence times up to the order of seconds [38].

¹⁰“Soon” in this context means still a long time, but the experiment could be doable within this century.

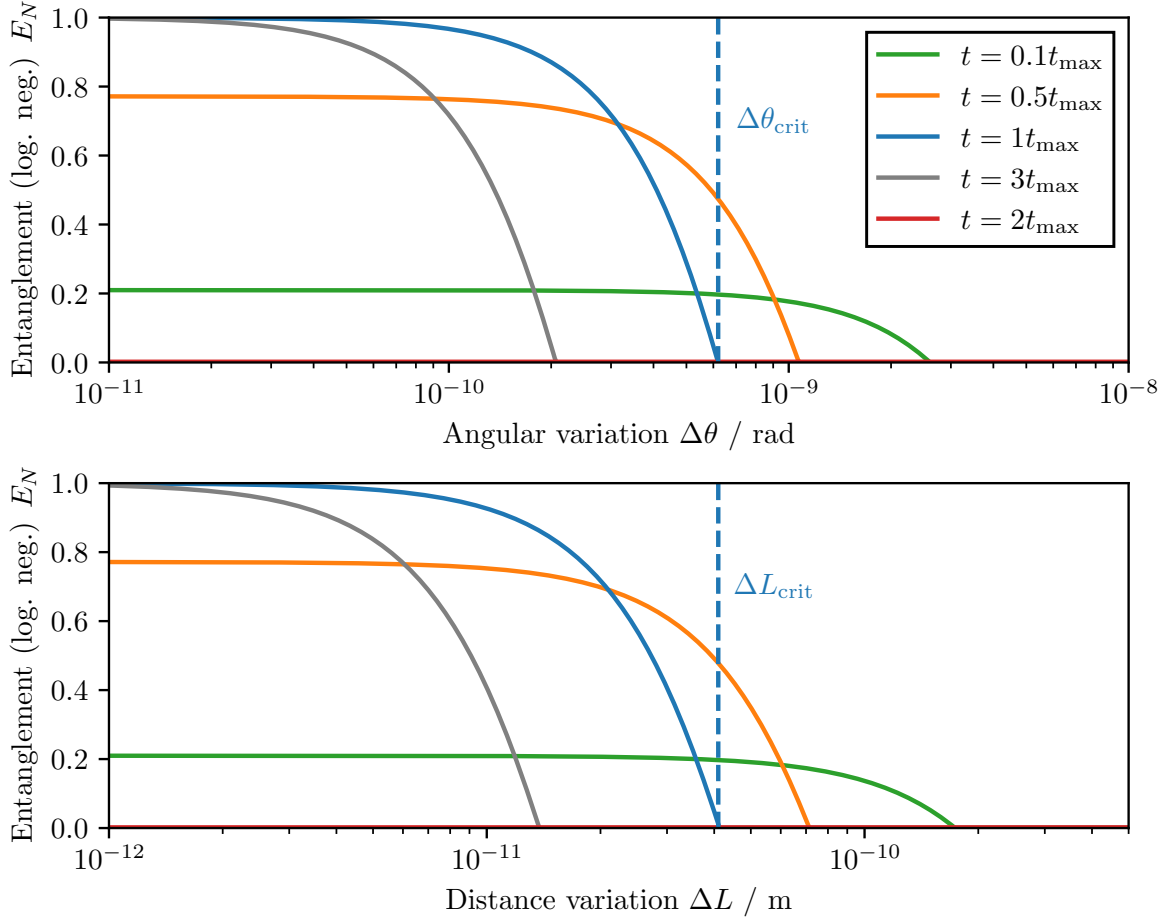


Figure 4.2: Entanglement quantified by the logarithmic negativity (eq. (2.21)) dependent on the angular variation $\Delta\theta$ and the distance variation ΔL in the parallel configuration. The entanglement is shown at different times, where $t_{\text{max}} \approx 258$ ms is the time of maximal entanglement from eq. (2.24). At the critical point $\Delta\theta_{\text{crit}}$ or ΔL_{crit} all entanglement is lost.

The entanglement of the system shown in fig. 4.2 behaves as expected. At some critical point $\Delta\theta_{\text{crit}}$ and ΔL_{crit} , the entanglement is completely lost. For the used parameters and in the parallel orientation, this threshold is around $\Delta\theta_{\text{crit}} \approx 6 \times 10^{-10}$ rad and $\Delta L_{\text{crit}} \approx 1.4 \times 10^{-10}$ m, which seems quite challenging experimentally. However, it seems like that for smaller times $t < t_{\text{max}}$ larger variations can be tolerated for the cost of having less total entanglement. This again is expected. For smaller times, the gravitational force did not have enough time to fully entangle the two particles, but also the decoherences (dependent on $\propto t^2$; see eq. (4.10) and appendix D) did not have enough time to built up. It is therefore logical, that if one does not require to measure a fully entangled state and less entanglement $E_N < 1$ is also sufficient, it may be beneficial to measure at a time $t < t_{\text{max}}$. In theory, it would be enough to measure *any* entanglement $E_N > 0$ but one has to make sure that no other mechanisms

such as direct or indirect entanglement through other couplings or noise sources have smaller entanglement rates (for a discussion see chapter 5). Measuring at an earlier point in time does not only reduce the duration of a single experimental measurement, but also increases the stability against displacement variations. This optimal time of measuring for a certain required amount of entanglement is shown in fig. 4.3. The

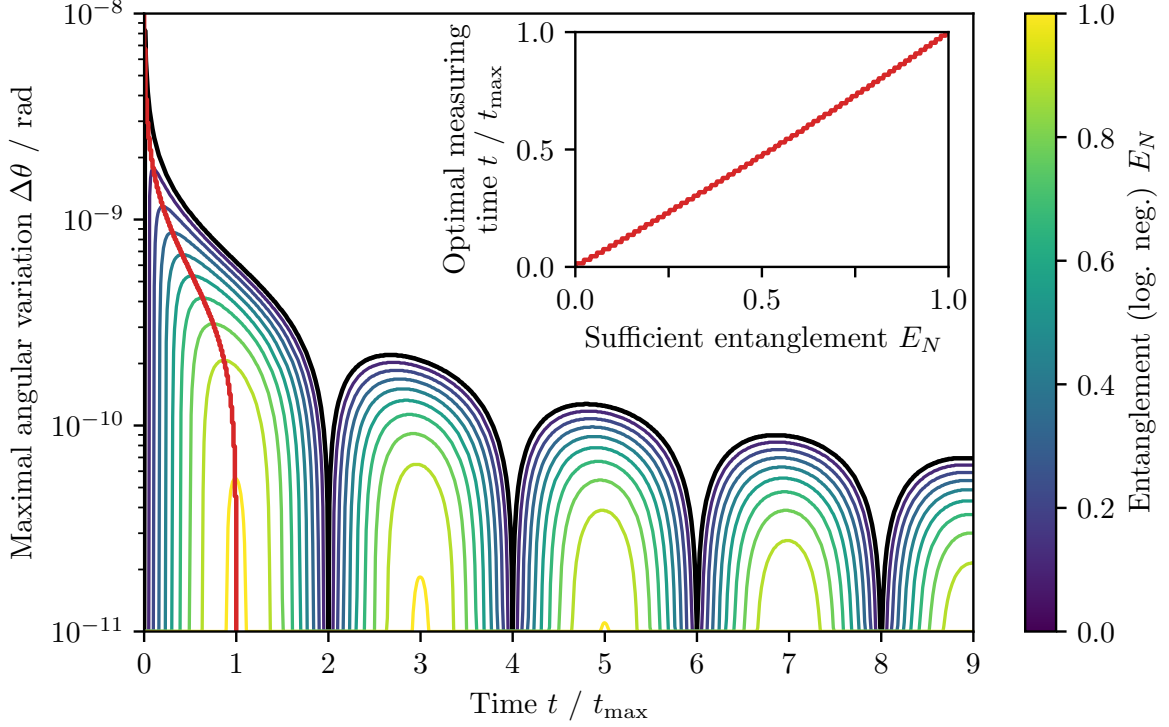


Figure 4.3: Maximal angular variation for a given time and a given required amount of entanglement. The outer most black line corresponds to the time dependence of $\Delta\theta_{\text{crit}}$. The top left as well as the red curve in the main figure shows the optimal measuring time for a sufficient amount of entanglement. At times $2kt_{\text{max}}$ no entanglement can be measured.

chart additionally lets one read out the corresponding maximal angular variation after a set time. Conversely, if one is experimentally limited by a certain maximum angular variation, one can read off the corresponding best measurement time and the maximum amount of entanglement that can be obtained. It also can be seen that at times $2kt_{\text{max}}$, $k \in \mathbb{N}$ there is no entanglement. This corresponds to the findings from the ideal scenario in chapter 2.

4.2 The optimal setup

With the general framework in hand, the next logical question to ask is, if the stability against placement-variations can be improved. The general rule of thumb for these optimizations is the following: Increase the gravitational interaction by either heavier and larger particles or by reducing the separation distance L without substantial sacrifices of experimental realization. As an example, the stability increases intuitively by increasing the separation distance L . However, this does also increase the time t_{\max} until the maximum amount of entanglement can be measured which would increase the total time $\sim \#t_{\max}$ of the experiment with $\#$ individual measurements. It is not immediately obvious, how the stability and the maximum possible variations $\Delta\theta_{\text{crit}}$ and ΔL_{crit} behave for the change in parameters. In the following section, precisely the changing of this stability is discussed for changing the orientation α, β , the separation L , the mass $M_A = M_B \equiv M$ and the superposition size $\Delta x_A = \Delta x_B \equiv \Delta x$.

4.2.1 Orientation

The arguably easiest parameter to change experimentally is the orientation of the superpositions, which is quantified by α and β in fig. 4.1. As already seen in fig. 2.2, the entanglement dynamics are dependent on the orientation. In the parallel orientation, the states take twice as long as in the orthogonal orientation to become maximally entangled. In general, it is advantageous to aim for the highest entanglement rate and thus the smallest $t_{\max}(\alpha, \beta)$, as this requires a shorter coherence time and thus reduces the total time of the experiment. The previous results from chapter 2 can be further generalized for an arbitrary orientation α, β . The logarithmic negativity is given by

$$E_N = \log_2 (1 + |\sin \Delta\phi|) \quad (4.11)$$

where $\Delta\phi$ is now dependent on the orientation and is defined as (for $\Delta x \ll L$)

$$\Delta\phi = \frac{GM_A M_B t \Delta x_A \Delta x_B}{8\hbar L^3} \left(\sin \alpha \sin \beta - \frac{1}{2} \cos \alpha \cos \beta \right). \quad (4.12)$$

The maximum entanglement $E_N = 1$ is reached for $\Delta\phi = \pm\pi/2$ and thus after a time

$$t_{\max}(\alpha, \beta) = \frac{4\pi\hbar L^3}{GM_A M_B \Delta x_A \Delta x_B} \left| \sin \alpha \sin \beta - \frac{1}{2} \cos \alpha \cos \beta \right|^{-1}. \quad (4.13)$$

For some specific symmetric cases, the resulting times for different orientations are shown in fig. 4.4. The global minima of $t_{\max}(\alpha, \beta)$ is attained in the orthogonal orientation. This is not surprising considering that this orientation maximizes the *differences in separation distances* between all superposition states. Much more interesting and surprising are the unanticipated singularities in fig. 4.4 which appear for

$$\sin \alpha \sin \beta = \frac{1}{2} \cos \alpha \cos \beta. \quad (4.14)$$

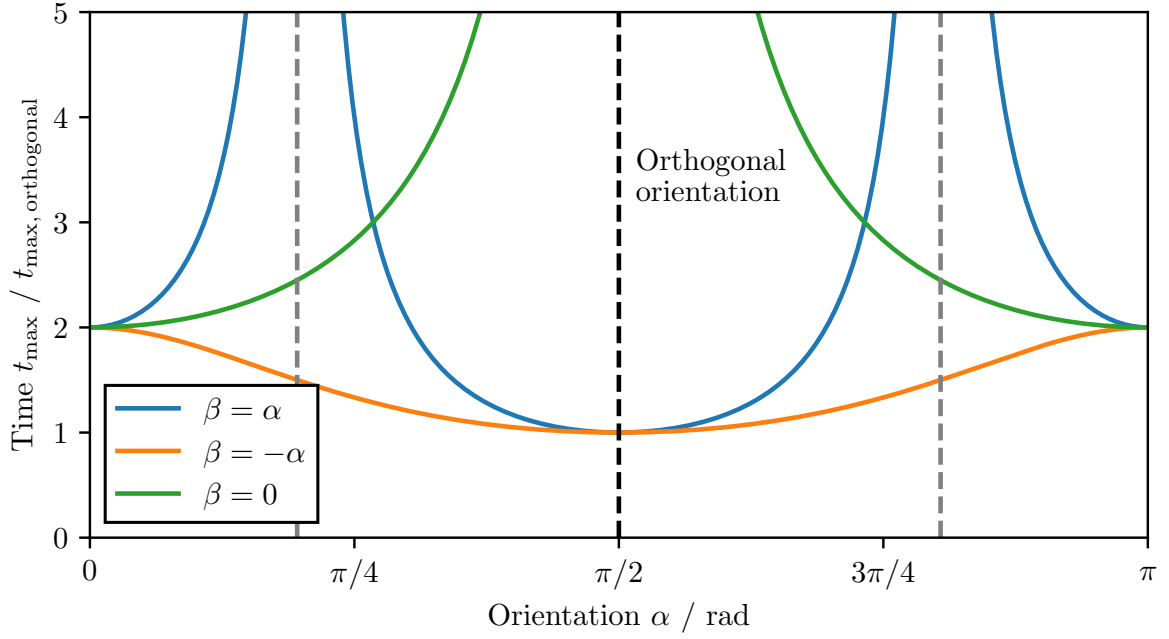


Figure 4.4: Time t_{\max} after which maximum entanglement ($E_N = 1$) is reached for different orientations. Only the most interesting and highly symmetric cases $\alpha = \pm\beta$ and $\beta = 0$ are shown. The singularity $t_{\max} \rightarrow \infty$ for $\beta = 0$ and $\alpha = \pi/2$ is expected. The two other singularities at $\alpha = \beta = 2 \arctan(\sqrt{3} \pm \sqrt{2})$ are explainable by the “harmonic mean” in fig. 4.5.

For $\beta = 0$ the singularity at $\alpha = \pi/2$ is not surprising. In this configuration, the distances $|\psi_A^1\rangle \leftrightarrow |\psi_B^{1,2}\rangle$ and $|\psi_A^2\rangle \leftrightarrow |\psi_B^{1,2}\rangle$ are identical and thus these states accumulate the same phases, resulting in a factorable global phase. In the case of $\alpha = \beta$, the two singularities are precisely given in the orientation

$$\alpha = \beta = 2 \arctan(\sqrt{3} \pm \sqrt{2}) \approx 90^\circ \pm 54.74^\circ. \quad (4.15)$$

There does not exist a straight-forward geometric interpretation why no entanglement is generated exactly in this configuration, however all 4 separation distances between the states form the “harmonic mean” visualized in fig. 4.5. Here, in the limit $\Delta x \ll L$

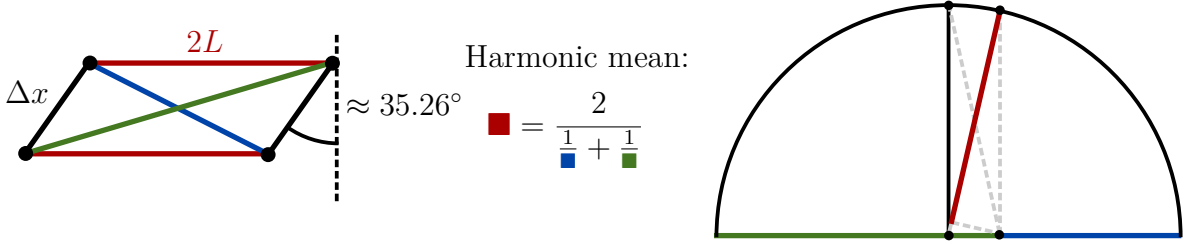


Figure 4.5: left: The system in the orientation $\alpha = \beta = 2 \arctan(\sqrt{3} - \sqrt{2})$. For $\Delta x \ll L$, all separation distances exactly form the *harmonic mean*. Here, the phases due to the mutual gravitational interaction precisely cancel out resulting in no entanglement. **right:** Geometric visualization of the harmonic mean.

everything local phase precisely cancels out resulting in a loss of entanglement. To avoid all these singularities, it is advisable to always take $\alpha = -\beta$, where all orientations result in roughly similar entanglement times t_{\max} , at most only differing by a factor of 2.

It should come as no surprise that the different orientations exhibit different stabilities. Logically, one would expect the orthogonal configuration to be much more sensitive to angular variations than the parallel one. In contrary, the parallel configuration should be much more stable against variations in the distance, since no phase difference (“dephasing”) is induced between the two superposition states $|\psi_{A(B)}^1\rangle$ and $|\psi_{A(B)}^2\rangle$ of the particle A (B).

The effect of different orientations on the stability against angular variations and the behavior of the critical angular variation $\Delta\theta_{\text{crit}}$ is shown in fig. 4.6. As expected, the orthogonal configuration is the most stable against these kind of variations. This is, because the dephasing ultimately depends on the distance between the state and the shield $L \pm \Delta x/2 \cos \theta \approx L \pm \Delta x/2(1 - \theta^2/2)$, which is a only second order effect of the angular variations θ . This explains the apparent “infinitely” good stability in the figure, as the analytical solution only uses first order approximations in θ . Exact numerical results however cap the stability at $\Delta\theta_{\text{crit, orthogonal}} \approx 7.3 \times 10^{-5}$ rad.

Respectively, the stability against distance variations ΔL_{crit} for different orientations is shown in fig. 4.7. Again aligning with expectations, the parallel configuration is (in

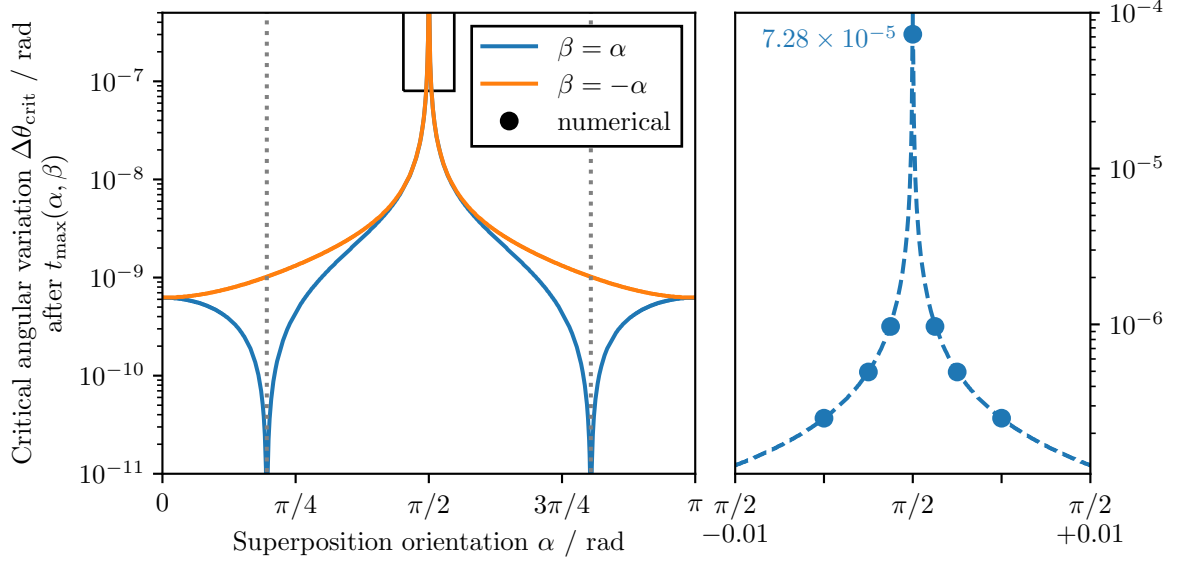


Figure 4.6: Critical angular variation $\Delta\theta_{\text{crit}}$ for different orientations after the time $t_{\text{max}}(\alpha, \beta)$ for which maximum entanglement is reached. The **orthogonal orientation** magnified on the right is very stable against angular variations and only numerical methods show a finite stability value. The singularities in the left figure for $\alpha = \beta$ arise from the fact, that these orientations need infinite time to entangle as already seen in fig. 4.4.

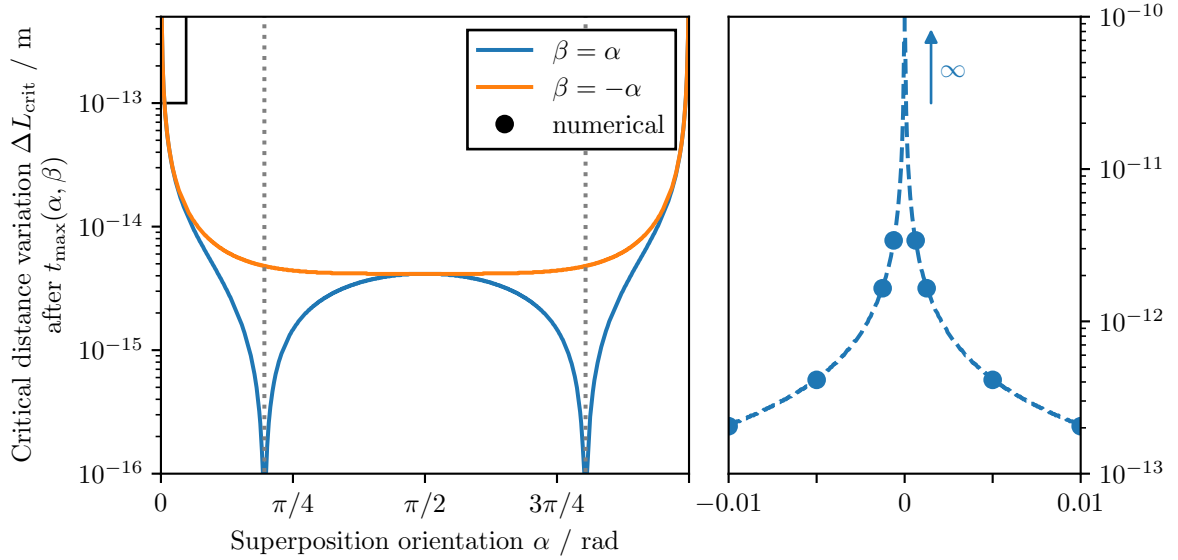


Figure 4.7: Critical distance variation ΔL_{crit} for different orientations after a time $t_{\text{max}}(\alpha, \beta)$. Here, the **parallel orientation** (magnified on the left) is infinitely stable against placement variations.

theory) exhibits an infinite stability. One however could argue, that a for this to hold, the uncertainties in the angular placement have to be zero. As could be seen in fig. 4.6, these variations are at most around $\sim 5 \times 10^{-5}$ rad and thus a realistic upper bound for the minimum required distance variations is given by $\Delta L_{\text{crit,parallel}} = \Delta L_{\text{crit}}(\alpha \approx 5 \times 10^{-5} \text{ rad}) \simeq 4 \times 10^{-11} \text{ m}$. It is important to keep in mind, that these stability values can be improved substantially by changing e.g. the separation distance L or the particle size R .

Considering these results, the parallel orientation seems to be the only realistic experimental option, even if it requires slightly larger coherence times t_{max} . Keeping particle-shield separation variations below 0.01 nm - approximately the size of a single atom - is practically impossible, especially under the additional consideration of the thermal vibrations of the shield and the particles, which are in the same order of magnitude as seen later in chapter 5. With this data on hand, it is possible to generate the stability diagram in fig. 4.8, showing the optimal orientation in which the most entanglement can be measured. For most combinations of ΔL and $\Delta\theta$, entanglement is only given in one certain orientation.

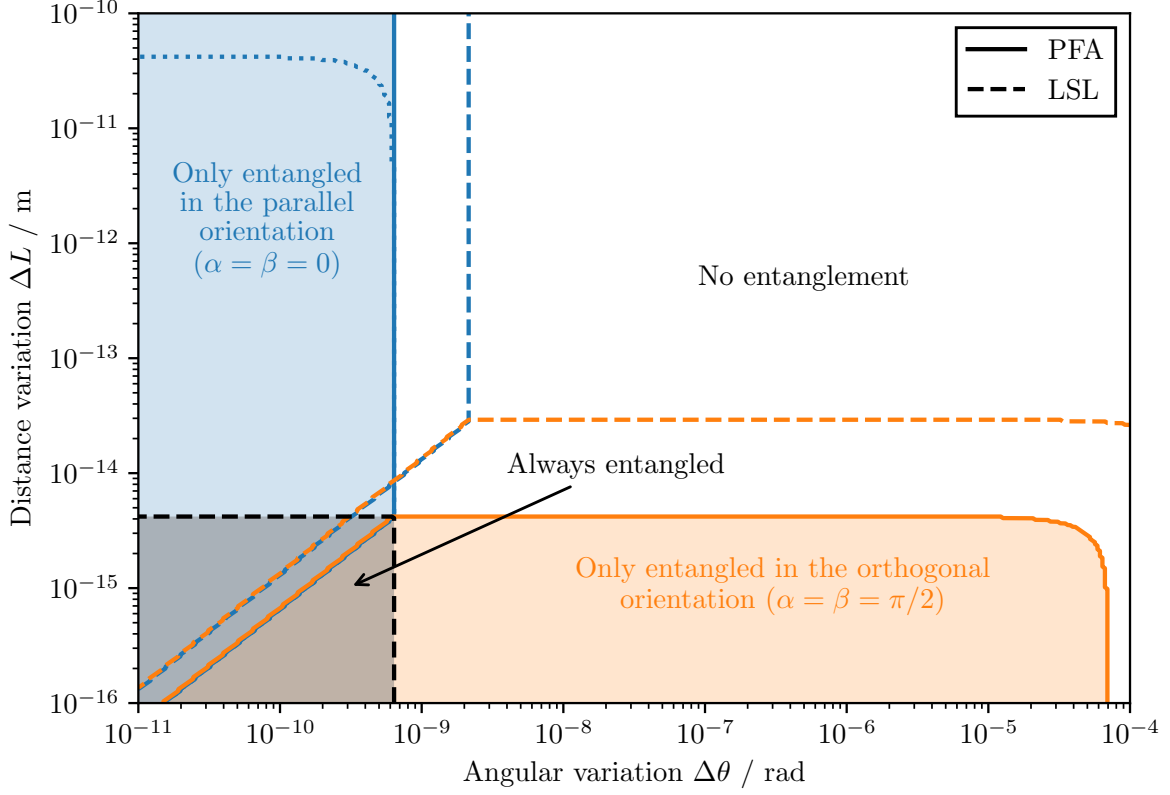


Figure 4.8: Optimal orientation for the experimental setup dependent on the variations in angle $\Delta\theta$ and distance ΔL for a initial separation distance of $L = 2R = 2 \times 10^{-5}$ m at time t_{\max} . The different predictions for the proximity-force-approximation (PFA) and the large-separation-limit (LSL) are shown. At a distance of $L = 20 \mu\text{m}$ the actual casimir interaction is somewhere in the middle between both approximations. In the region where entanglement is given regardless of the orientation (the bottom left), the orientation with *more* entanglement is still colored. The dotted line corresponds to the realistic upper bound discussed in the text.

4.2.2 Separation, mass and superposition size

It is possible to improve the required stability in placement and consequently the entanglement generation by changing the other parameters shown in fig. 4.1 besides the orientation. It is especially easy to modify the separation distance L during the experiment as one is only limited in the trap stability close to the shield discussed in section 4.3. The other parameters like the particle mass M and thus the radius R , the particle material and the superposition size Δx are considerably more difficult to change. One is limited by the experimental implementation of the spatial superpositions. Considering that up to date, the largest spatial superposition of a “macroscopic object” is in the order of $\Delta x \sim 500$ nm for masses of 4×10^{-23} kg [13], large changes in the delocalization size Δx or the particles mass might be virtually impossible. However, out of a theoretical standpoint, the effects of all these parameters and the improvements reachable in stability are interesting and considered in the following section.

Beginning with the effect of a larger particle-shield separation L , the improvements on angular stability are shown in fig. 4.9. A similar figure can be created for the stability of

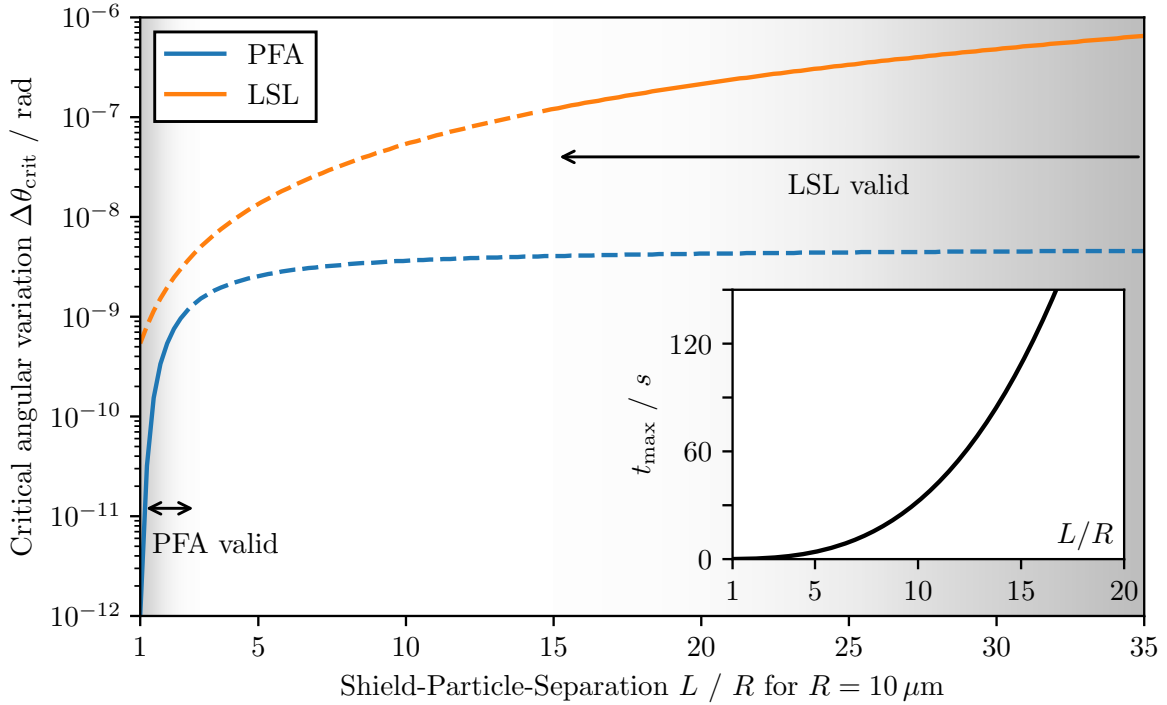


Figure 4.9: Stability against angular variations for increasing separation distances L in units of $R = 10 \mu\text{m}$ after a time $t_{\text{max}}(L)$. The dependence on the radius can be seen in fig. 4.10. Two models for the casimir-interaction are shown: The proximity-force-approximation (PFA) and the large-separation-limit (LSL). The regions outside the models validity are indicated with dashed lines. In the bottom right the time $t_{\text{max}}(L) \propto L^3$ is shown.

distance-variations ΔL , but as already discussed previously, the setup is very (infinitely) stable against small distance variations in the parallel configuration. It is intuitively clear that a larger separation improves the stability, as the relative effect of the variations $\sim \Delta x \sin \theta \ll L$ decreases and the Casimir potential tends towards zero. However, a larger separation also increases the time $t_{\max} \propto L^3$ until the maximum entanglement is built up. The combination of both effects leads to the result shown in fig. 4.9. Due to the strong distance dependence on the casimir model, both limits for either small separations $L \sim R$ (PFA) or large separations $L \gg R$ (LSL) have been compared. The “real” casimir potential lies somewhere between the two models. In general, it can be said, that a large separation is desirable, as long as the required coherence times are still reachable. Looking at the final averaged density matrix $\langle \rho \rangle$, it is possible to deduce the dependence of $\Delta\theta_{\text{crit}}$ on the separation L . The off-diagonal decoherence terms calculated in appendix D and given by eq. (D.8) scale similar to

$$\langle \rho_{ij} \rangle \sim \exp \left\{ - \left(\frac{2\phi_{\text{Casimir}}\Delta x}{(L - R - d/2)^3} \pm \frac{\phi_{\text{Gravity}}\Delta x}{4L^2} \right)^2 (\Delta\theta)^2 t^2 \right\} \quad (4.16)$$

where the gravity term can be neglected for small L ($\phi_{\text{Gravity}} \ll \phi_{\text{Casimir}}$). At the point $\Delta\theta_{\text{crit}}$ all entanglement is lost leading to $\langle \rho_{ij} \rangle \rightarrow 0$. The resulting dependence on ρ

$$\Delta\theta_{\text{crit}} \sim \frac{1}{t_{\max}} (L - R - d/2)^3 \sim \frac{(L - R - d/2)^3}{L^3} \quad (4.17)$$

which aligns very nicely with the blue curve for the PFA in fig. 4.9 ($R^2 = 0.99$). Similar arguments show that for large separations in the LSL the critical angular variation scales with $\Delta\theta_{\text{crit}} \sim L^2$.

The mass of the particles is determined by their radius R as well as their material. Most likely, the trapped and levitated particles are made of silica (SiO_2) with a density of $\rho_{\text{Silica}} = 2648 \text{ kg/m}^3$, as this material has been used widely in experiments on levitated nanoparticles [42, 43]. Due to its transparency, silica is very easy to trap in strong optical traps, but even quantum control in magnetic traps has been demonstrated with silica [43]. For this thesis, I will assume that all trapped particles are made of silica. Otherwise denser or heavier materials like e.g. stable osmium and lead isotopes would be worth considering. Trapping them in a paramagnetic trap could be theoretically possible and interesting as sufficient masses could already be reached with far fewer atoms and smaller particles, further improving coherence times and quantum control. The effect on angular stability of a larger and thus heavier particle is shown in fig. 4.10. It is important to note, that the time t_{\max} scales with M^{-2} and thus effectively with R^{-6} , making the effect of a slightly larger sphere very noticeable. One does need to find the ideal size of the sphere depending on what is possible experimentally: The mass must be large enough for gravity to have a measurable effect but simultaneously small enough for sufficient quantum control in the laboratory. Estimations suggest the usage of masses around the order of $10^{-11} \text{ kg} \approx 10^{-3} m_p$ as being possible [38]. The scaling of $\Delta\theta_{\text{crit}}$ with a changing size R of the particles can be determined similar to before. It

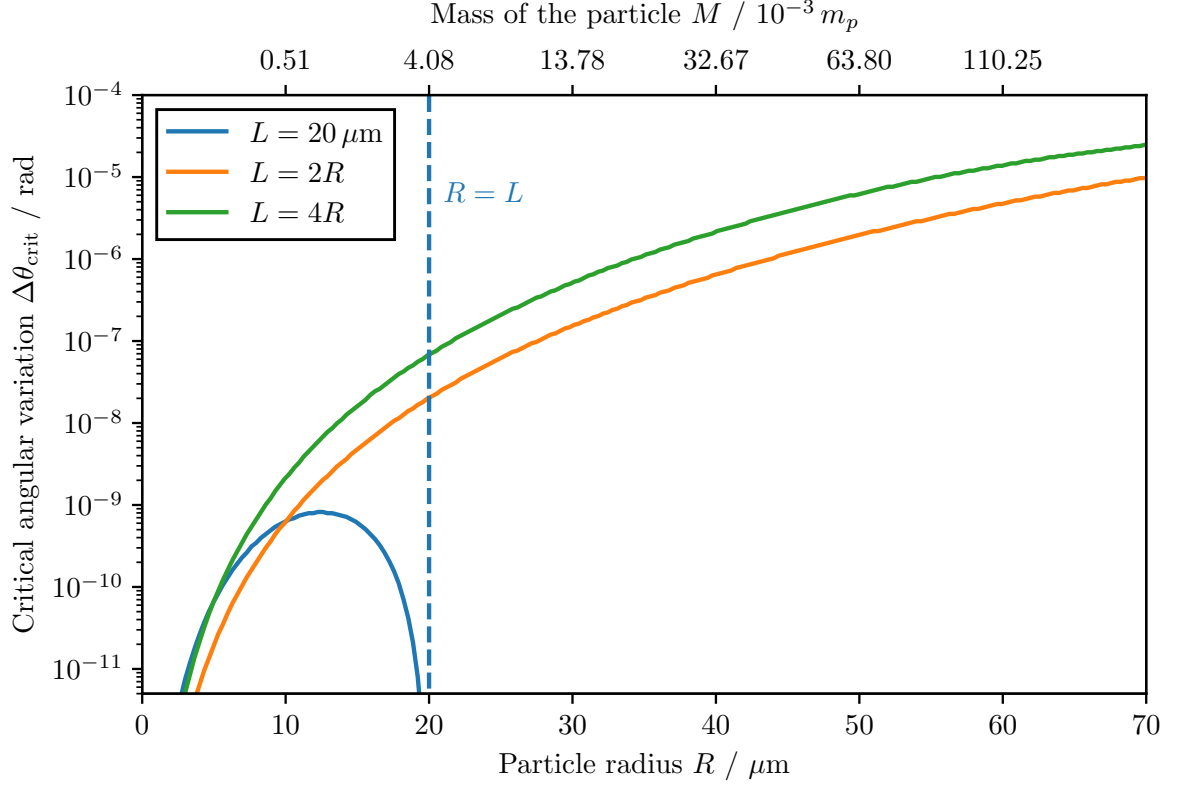


Figure 4.10: Critical angular variation $\Delta\theta_{\text{crit}}$ for different sized particles after a time $t_{\text{max}}(M)$. The mass of the corresponding particle in units of the Planck mass $m_p = \sqrt{\hbar c/G} \approx 2.176 \times 10^{-8} \text{ kg}$ is given on the top axis. For particles as large as the separation $R = L$, the surface-to-surface separation is almost zero, resulting in large casimir forces and thus no entanglement.

turns out, that for a constant separation L , the critical angular variation scales with

$$\Delta\theta_{\text{crit}} \sim \frac{(L - R - d/2)^3}{\phi_{\text{Casimir}}} \frac{1}{t_{\text{max}}} \sim \frac{(L - R - d/2)^3 R^6}{R} \quad (4.18)$$

whereas for $L \propto R$, the time $t_{\text{max}} \propto L^3/R^6$ varies additionally resulting in

$$\Delta\theta_{\text{crit}} \sim (R - d/2)^3 R^2. \quad (4.19)$$

The final parameter that theoretically be freely modified, is the size of the superposition Δx . A larger superposition size would increase the entanglement generation due to gravity because the differences in the distances between all superposition states would increase. Such effects ultimately lead to a faster build-up of entanglement scaling with $t_{\text{max}} \propto (\Delta x)^{-2}$. In matter wave experiments, superposition sizes of massive objects up to $\Delta x \approx 500 \text{ nm}$ were already achieved [13]. These sizes are much smaller than the size of the particle itself at $10 \mu\text{m}$. The effect of the superposition size on stability is shown in fig. 4.11. For large superposition sizes, the time until maximal entanglement

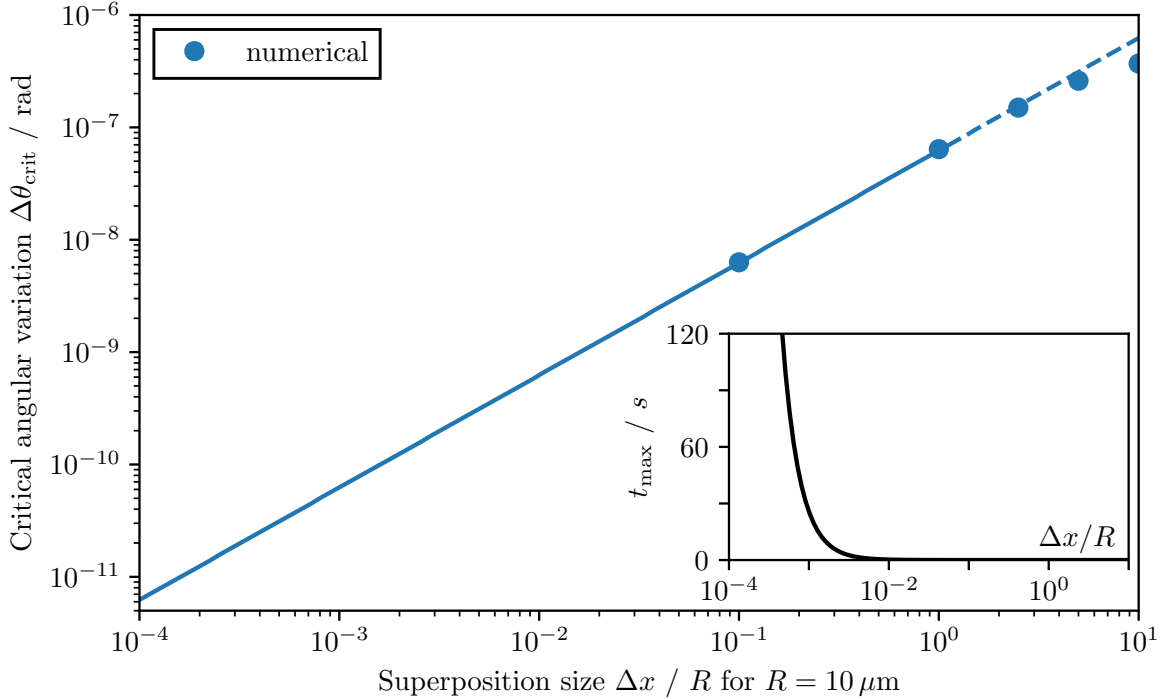


Figure 4.11: Effect of the superposition size Δx on the critical angular stability $\Delta\theta_{\text{crit}}$ after a time $t_{\text{max}}(\Delta x)$. For $\Delta x \gtrsim R$, numerical results are used. In the lower left, the time till maximum entanglement $t_{\text{max}} \propto (\Delta x)^{-2}$ is shown. For $\Delta x \ll R$, the resulting relation between Δx and $\Delta\theta_{\text{crit}}$ is linear.

is reached, decreases drastically. In the shorter time, the dephasing due to the casimir effect between the shield and the states is less substantial, increasing the stability against

variations in the placement. A larger superposition size on the other hand results in a greater effect of angular variations $\sim \Delta x \sin(\theta)$. Both of these effects result in a effective scaling of $\sim \Delta x$, which explains the linear curve¹¹.

4.3 Trapping the particle

Another consequence of shielding that requires consideration is the trapping. Levitated particles are trapped and cooled in an ultra-high vacuum by either a magnetic, optical or electrical radiofrequency Paul-trap [44]. These traps differ in the trapping mechanism, but if the particle is cooled close to the ground state, all trapping potentials can be considered “harmonic” with trapping frequency $\omega_{\text{trap}} = 2\pi \times f$. The strength of the trapping potential $V \propto f^2$ differs for the different trapping types. Typical values range from 1 Hz – 1 kHz for magnetic traps [43, 44] up to 10 kHz – 300 kHz for optical traps [44]. The different types of traps also offer different advantages and disadvantages: Optical traps are relatively noisy due to the constant interaction between the particle and the light. Magnetic traps for large particles are less noisy, but only low trapping frequencies are possible [44]. For electric traps, the particle must be charged, which causes a lot of different problems, as seen in section 5.1.

Strictly spoken, to generate cat-state superpositions a non-harmonic potential like e.g. a “double well potential” is required. In the parallel orientation, the double wells are also oriented parallel to the shield resulting in a almost-harmonic potential from the side-view as seen in fig. 4.12.

If the particle in the harmonic trapping potential is placed close to the shield, the Casimir interaction $\sim \mathcal{L}^{-2}$ can disturb the trapping and eventually even suck the particle onto the shield. The total potential $V_{\text{tot}} = V_{\text{trap}} + V_{\text{Casimir}}$ is shown in fig. 4.12 for a stable and unstable configuration. Due to the influence of the attractive Casimir force, the equilibrium position of the trap shifts slightly closer to the shield by $\Delta\xi$. This shift

$$\Delta\xi = \frac{-\nabla V_{\text{Casimir}}}{m(2\pi f)^2} = \frac{2\hbar c\pi^3}{720} \left(\frac{\varepsilon_r - 1}{\varepsilon_r + 1} \right) \varphi(\varepsilon_r) \frac{R}{\mathcal{L}^3} \frac{1}{m(2\pi f)^2} \quad (4.20)$$

is negligibly small as it is in the order of $\Delta\xi \approx 10^{-13}$ m for $f = 1$ kHz and $L = 2R = 20 \mu\text{m}$.

To determine the stability of a trapped particle with mass $M \propto R^3$ in a trap with frequency f placed at a distance $L_0 > R$ in front of the shield, the number of bound energy-eigenstates in the potential V_{tot} is considered. From fig. 4.12 it becomes clear, that as long as the particles thermal energy is well below E_0 , the trap is stable and the particle is bound. Here, E_0 is defined as the local maximum of the potential

$$E_0 = \max_{L \in (R, L_0)} (V_{\text{trap}} + V_{\text{Casimir}}) \quad (4.21)$$

¹¹Here it is shown in a double-logarithmic plot. The relation between Δx and $\Delta\theta_{\text{crit}}$ is nevertheless linear, which can be seen with similar arguments as used previously.

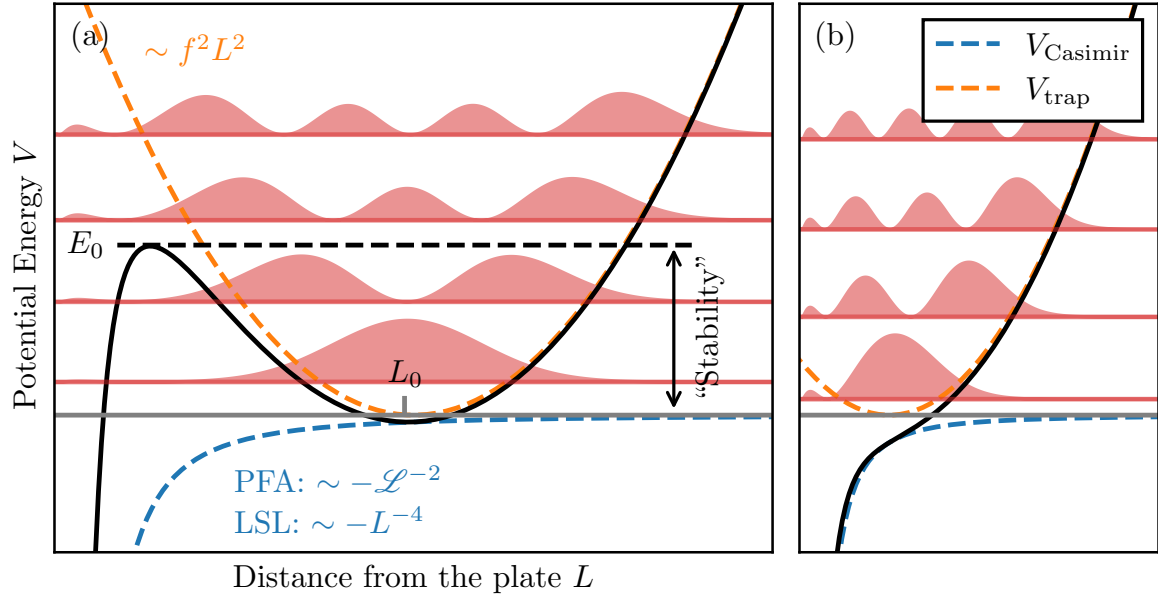


Figure 4.12: Visualization of the potential as an overlay of the harmonic trapping potential $V_{\text{trap}} = m(2\pi f)^2 L^2/2$ and the casimir potential V_{Casimir} . f is the trapping frequency and L_0 the position of the trap. In red, eigenstates of the potential are visualized offset by the eigen-energies. **(a)** Almost harmonic bounded potential which can hold the particle, if its energy is less than E_0 . **(b)** Potential with no bounded states. Here, trapping is not possible.

where L_0 is the position where the particle is trapped. If there does not exist a local maximum, i.e.

$$\frac{\partial}{\partial L} (V_{\text{trap}} + V_{\text{Casimir}}) > 0 \quad (4.22)$$

for all $L \in (R, L_0)$, the resulting trap cannot be stable. These regions of no stability are shown as a white area in the stability diagram fig. 4.13. In the general case, the stability can be measured by computing the number of bound eigenstates $n(E_0)$ with energies less than E_0 and comparing them with the number of thermally excited states \bar{n} . At a temperature T on average

$$\bar{n} = \frac{1}{e^{\beta\hbar\omega} - 1} \quad (4.23)$$

states are occupied, where $\beta = 1/k_B T$ and $\omega = 2\pi f$. This is true, as long as the potential is assumed to be harmonic, which is, as seen shortly, a very good approximation. To find the number of possible bound energy-eigenstates in the potential, I am using the **WKB-approximation** [45]. In this approximation, the energy of the n -th eigenstate of a smooth and appropriately slow varying potential $V(x)$ can be calculated using [45, p. 163]

$$\int_{x_1}^{x_2} dx \sqrt{2m(E - V(x))} = \left(n + \frac{1}{2}\right) \pi \hbar, \quad (4.24)$$

where $V(x_1) = V(x_2) = E$ are two turning points corresponding to energy E . Conversely, it is possible to use this approximation to numerically estimate the total number of bound states in the potential $V = V_{\text{trap}} + V_{\text{Casimir}}$ using

$$n(E_0) \approx \frac{1}{\hbar\pi} \int_{x_1}^{x_2} dx \sqrt{2m(E_0 - V(x))}, \quad (4.25)$$

which is closely given (highest deviation around 40%; averaged relative error $\sim 0.9\%$) by the harmonic approximation $n(E_0) \sim E_0/\hbar\omega$. The resulting number of bound states is shown in fig. 4.13 as well as the stability boundaries at specific temperatures where $\bar{n} = n(E_0)$. It turns out, that regardless the type of the trap, a successful trapping even at room temperature should be possible as long as the particle is placed appropriately far away from the trap. The ability to trap and levitate the masses is therefore not significantly impaired by the presence of the Faraday shield.

4.4 Discussions

Looking at the preceding results, it is clear that the planned experiment represents a significant engineering challenge. The decoherence due to the Casimir interactions between the particles and the Faraday shield requires a accuracy in the placement of the particles in the order of $\Delta L = 10^{-10}$ m and $\Delta\theta = 10^{-9}$ rad. Achieving these accuracies appears to be very challenging and it will be necessary to adjust the originally proposed parameters in fig. 4.1. The separation distance L as well as the orientation are particularly easy to change. As discussed earlier, the parallel orientation might be the only viable option, as

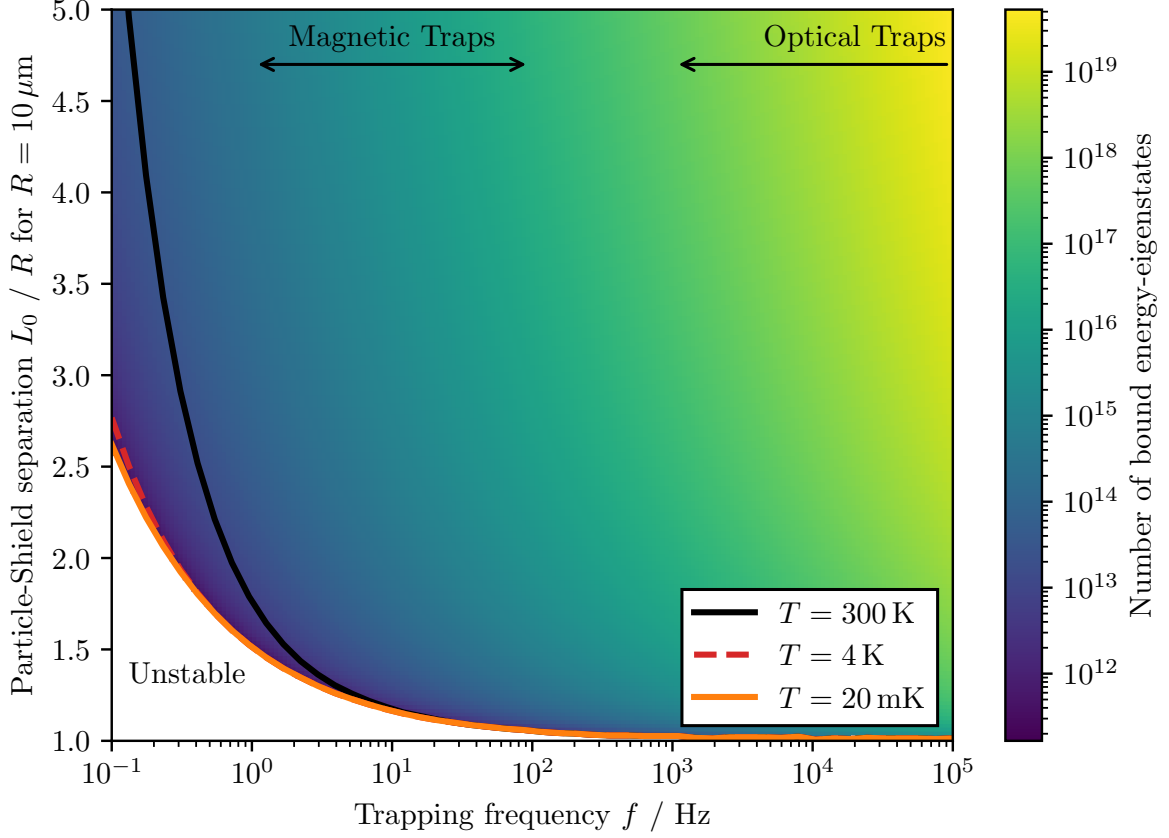


Figure 4.13: Stability diagram for different trapping frequencies $f = \omega/2\pi$ and particle-shield separations L_0 . The number of bound energy-eigenstates for each combination of f and L_0 are calculated using the WKB-approximation. The number of thermally occupied states \bar{n} at different Temperatures is overlaid. As an example, for $f = 1$ Hz, $\bar{n}(T = 300 \text{ K}) \approx 10^{13}$ states are thermally occupied. All regions below these boundaries are unstable. A increase in the radius R and thus the mass M improves the regions of stability massively.

this position is almost infinitely stable against variations in the distance. The orthogonal orientation would require placement accuracies in the order of single atoms (see in fig. 4.7). The separation L can be freely chosen and a larger separation reduces the effect of placement variations as seen in fig. 4.9 but substantially increases the required coherence time $t_{\max} \propto L^3$. It could also be argued that at a distance of $L \geq 200 \mu\text{m} = 20R$ (compare to section 2.3), the Faraday shield would no longer be required because the Casimir forces between the particles are ~ 10 times weaker than the gravitational interactions due to their rapid decrease at large distances. However, the loss of entanglement due to angular and distance variations in placement is not solely due to Casimir forces between the particle and the shield, so that a complete removal of the shield does not fully eliminate the required placement accuracy. The slightly varying gravitational interaction alone can induce enough decoherence on its own to destroy entanglement. The critical variations for a gravitational interaction alone in the parallel configuration after t_{\max} are given by $\Delta\theta_{\text{crit, ideal}} = 1.1 \times 10^{-3}$ rad and $\Delta L_{\text{crit, ideal}} = 7 \times 10^{-4}$ m, which should not pose an engineering problem.

Changing the other parameters such as the particles size or superposition size might not be possible. Substantially changing both would increase the difficulty in groundstate cooling and quantum control unforeseeable. For all these considerations, the trapping does not play a role as this should be possible with a suitable magnetic or optical trap for almost any possible configuration of the setup parameters (compare to the results from section 4.3).

One of the objectives of this thesis is, to determine whether it is possible to bring the particles closer together through the presence of the Faraday shield in order to increase gravitational entanglement and reduce the required coherence times. To achieve this, the previous results from this chapter can be used to find the optimal parameters of the experimental setup. The goal of the optimization process can be expressed as the following:

One wants to get *as much entanglement as possible* in the *shortest time possible* with the *largest possible variations* in the placement while still considering the limitations in the particles mass as well as in the superposition size.

In full generality, it is not possible to find a local optimum for choosing the parameters. This is because (if the mass M and the superposition size Δx is fixed) the coherence time - which should be minimized - scales with $t \propto L^3$ by eq. (4.13) and the critical angular variation - which should be as large as possible - scale with $\Delta\theta_{\text{crit}} \propto (L - R)^3/L^3$ for small separations (eq. (4.17)) or $\Delta\theta_{\text{crit}} \propto L^2$ for $L \gg R$. Both of these optimization criteria cannot be fulfilled simultaneously as long as no constraints are given. Given however a coherence time t_{target} and/or the minimum possible placement accuracy, it is possible to determine the required sphere-plate separation L as well as the amount of entanglement, one can maximally expect using the following steps:

1. Lets assume that the size of the particle R and consequently the mass $M = 4/3\pi R^3 \rho_{\text{Silica}}$ as well as the superposition size Δx are fixed. An increase in ei-

ther of them would have a positive effect of the optimization goal stated above, as the time t_{\max} decreases and the stability against placement variations increases simultaneously.

2. The following ratio given by eq. (4.13) in the parallel orientation and by Ref. [38]

$$\frac{M^2(\Delta x)^2}{L^3} t_{\max} = \frac{8\pi\hbar}{G} = \text{const.} \quad (4.26)$$

is fixed. For orthogonal configurations, this constant would reduce by a factor of $1/2$.

3. In general it is possible to measure at a earlier time $t_{\text{target}} = \tau t_{\max}$ (i.e. the coherence time) with $\tau \leq 1$, where less total entanglement has been build up but in general a grater stability against placement variations can be achieved (see fig. 4.3). Putting all assumptions together, the ratio

$$\frac{t_{\text{target}}}{\tau L^3} = \frac{8\pi\hbar}{G} \frac{1}{M^2(\Delta x)^2} = \text{const.} \quad (4.27)$$

is constant.

4. In the parallel orientation, the distance variations don't matter as the system is infinitely stable against variations in the particle-shield separation. The critical angular variation however scales like $\Delta\theta_{\text{crit}} \sim (L - R)^3/L^3$ for small distances and like $\Delta\theta_{\text{crit}} \sim L^2$ shown in fig. 4.9. it is therefore possible to determine the minimum separation $L_{\min} > R$ for a given placement accuracy.
5. Using the required separation, one can calculate $\tau \in (0, 1]$ using eq. (4.27) and look up the maximal possible entanglement in the top right of fig. 4.3 after an evolution time τt_{\max} .

As an example, the radius is fixed as $R = 10 \mu\text{m}$ and the superposition size is $\Delta x = 100 \text{ nm}$. Let's say that such a particle can be placed with an accuracy of $\Delta\theta = 10^{-7} \text{ rad}$ and a coherence time of 1 s is reachable. Using the steps outlined above, the required minimum particle-shield separation is around $L \approx 15R$ and the maximal amount of measurable entanglement is given by $E_N \approx 9.2 \times 10^{-3}$. For more entanglement, either a heavier particle, a larger superposition size, a higher placement accuracy or larger coherence times are required. It is therefore actually possible, to bring the particles closer together than without the Faraday shield and still measure entanglement. One is only limited by the placement accuracy and repeatability.

5 The consequences of a thermal shield

Up until now, the dynamics and properties of the shield were neglected. At a non-zero temperature however, thermal vibrations of the shield may influence the generation of entanglement substantially. In this chapter, firstly the required size of the shield is estimated. Then, the thermal vibrations of a large and small shield as well as the effect on entanglement generation is considered. In the experiment, the particles are cooled down into the ground state for effective quantum control and the generation of spatial superpositions. For cooling, often liquid helium at $T \approx 4$ K is used but cryogenic freezers can cool small setups down to the order of $T \approx 20$ mK. For all relevant calculations, these temperatures are used as a reference point.

5.1 Thickness and size of the shield

The thickness and radius r_s of the shield can be estimated by considering a real shield made of a conducting material with large conductivity σ . Even a superconducting shield could be considered for a almost perfect shielding against electrostatic field. For a real shield made of e.g. copper, the transmission T of electromagnetic waves is given by [46]

$$T = \left| \frac{\mathbf{E}_{\text{after}}}{\mathbf{E}_{\text{before}}} \right| = \frac{2}{Z_0 \sigma d} \quad (5.1)$$

where $Z_0 = 377 \Omega$ the impedance of free space (provided the shield is placed in a vacuum or air) and d the thickness of the shield. The electric conductivity has a strong dependence on temperature and decreases with $1/T^5$ ¹² with increasing temperatures [48, p. 284-286]. The electric conductivity for copper at room temperature ($\sigma = 59.6 \times 10^6$ S/m) should therefore be a very valid worst-case approximation. Measured data suggest a conductivity of $\sigma(T = 10) \approx 1.5 \times 10^{10}$ S/m [47].

The general goal is to place the particles as close as possible to increase the gravitational interaction between them, requiring to choose the thickness of the shield as thin as possible. To estimate the thickness of the shield, the condition that entanglement between the masses should be built up faster mainly due to gravity is used. All other

¹²This behavior is only true for temperatures below the Debye temperature. For copper, this limit is around $\Theta_D = 343$ K. In the experiment, the shield is cooled down, so the low-temperature limit of the electric conductivity for metals is very valid [47].

possible interactions like Coulomb or Casimir forces, should be suppressed sufficiently by the shield. To quantify the amount of entanglement built-up over time, I obt for a measure I call **entanglement rate**

$$\Gamma = \left. \frac{d}{dt} E_N(\rho) \right|_{t=0} \quad (5.2)$$

where E_N is an appropriate entanglement measure - in this case the logarithmic negativity [19] introduced in section 2.2. For the gravitational entanglement, the entanglement rate can be calculated in the parallel orientation using eq. (2.23):

$$\Gamma_{\text{Gravity}} = \frac{GM_A M_B \Delta x_A \Delta x_B}{16\hbar L^3 \log 2}. \quad (5.3)$$

The entanglement rate for other interactions should be smaller (and ideally a lot smaller) than the entanglement rate due to gravity, otherwise the eventually measured entanglement may not be solely due to gravitational interactions. In the following, the required size of the shield is estimated for undesired Coulomb- and Casimir interactions.

5.1.1 Shielding Coulomb-Interactions

The main focus of the shield is to block electromagnetic interactions between the particles. Experimentally, it might be beneficial for the masses to carry a small amount of charge to help with the trapping and allow the usage of electric traps [44]. The potential energy due to Coulomb interactions

$$V = \frac{1}{4\pi\epsilon_0} \frac{q_A q_B}{2L} \quad (5.4)$$

between the particles has the same structure as the gravitational potential and can therefore induce entanglement by the same logic. Using a shield, this coupling is suppressed by a factor of T . The entanglement rate Γ_{Coulomb} is therefore easily calculable in a similar form as eq. (5.3) to

$$\Gamma_{\text{Coulomb}} = \frac{T |q_A q_B| (\Delta x)^2}{64\pi\epsilon_0 \hbar L^3 \log 2} \quad (5.5)$$

Requiring that $\Gamma_{\text{Gravity}} > \Gamma_{\text{Coulomb}}$, this inequality yields a maximum transmission and thus a minimum thickness of

$$T \frac{|q_A q_B|}{4\pi\epsilon_0} < GM_A M_B \quad (5.6)$$

$$\iff d > \frac{1}{2\pi\epsilon_0 Z_0 \sigma G} \frac{|q_A q_B|}{M_A M_B} = \frac{9}{32} \frac{1}{Z_0 \sigma} \frac{1}{\pi^3 \epsilon_0 G \rho^2} \frac{e^2}{R^6} \quad (5.7)$$

where in the last step $M_A = M_B$ and $q_A = q_B = e$ has been assumed. The shield thickness heavily depends on the radius of the particle where small and light masses make the shield unworkably thick. A silica sphere with a radius of $R = 10^{-5}$ m would

require a shield around the thickness of 10 nm at 4 K up to $2.5 \mu\text{m}$ at room temperature. A realistic thickness for the shield at low temperatures could therefore be $d = 100 \text{ nm}$.

Electric fields however can still propagate around a Faraday shield of finite size and induce entanglement. It is however possible, to estimate the required radius r_s of the shield to block a specific amount η of the electric field. The resulting radius corresponding to η is derived in appendix C.1 and the result is shown in fig. 5.1. The transmission

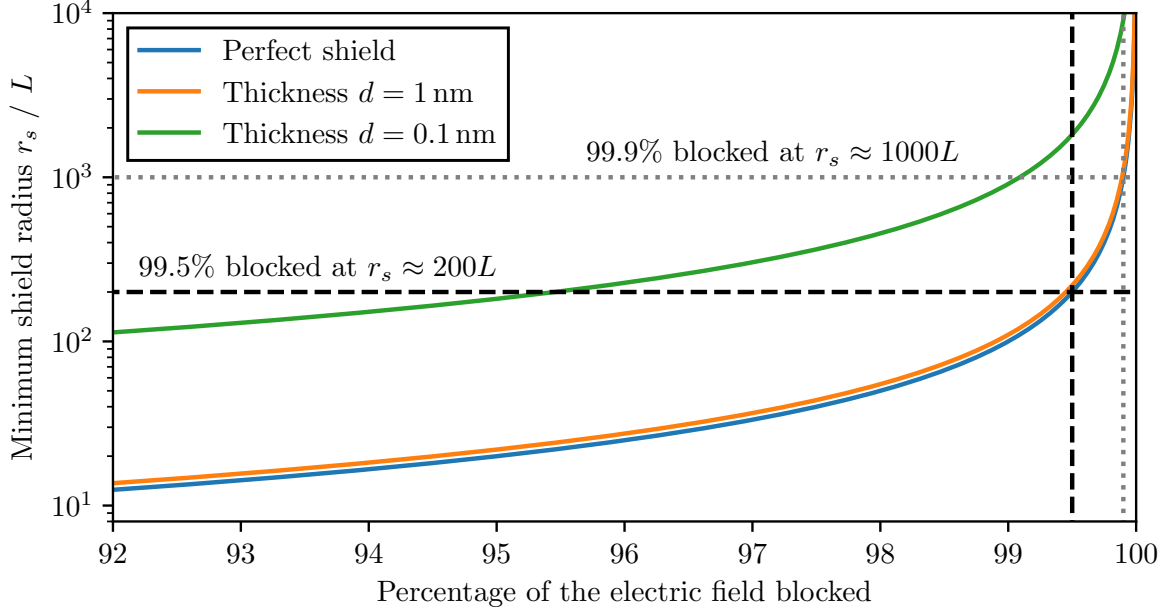


Figure 5.1: Radius of the shield depending on the shield effectiveness η . Additionally a real shield with different thicknesses d at room temperature is considered. For a shielding between 99.5 – 99.9% ($\eta = 0.995 - 0.999$), a radius of at least $r_s = 200 - 1000L$ should be used. For a sphere-plate distance of $L = 2 \times 10^{-5} \text{ m}$, the shield radius should be in the order of millimeters and centimeters.

T should be replaced by a modified transmission $\tilde{T} = T\eta + (1 - \eta)$ where the shield effectiveness η depends on r_s . Now, the condition eq. (5.6) introduces a limit for the minimum effectiveness and thus a limit on the minimum radius of

$$\eta_{\min} = 1 - \frac{4\pi\epsilon_0 G M_A M_B}{|q_1 q_2|}. \quad (5.8)$$

Thus using the setup with the parameters from earlier, a minimum effectiveness of $\eta_{\min} \gtrsim 0.99997$ and thus a radius of $\gtrsim 66 \text{ cm}$ is required. This shield is too large for all practical purposes and it might be beneficial to choose slightly heavier masses to reduce the shield size to the orders of $\sim 1 \text{ cm}$. This would require both spheres to have approximately double the radius than before. Using neutral masses without any charge would also be beneficial and the shield size could be reduced to only the size of the

spheres themselves, however it might be an engineering challenge, to trap and levitate uncharged massive particles.

5.1.2 Shielding Casimir-Interactions

Similarly to Coulomb interactions, it is possible to estimate the required thickness of the shield necessary to sufficiently suppress Casimir interactions. Between two spheres with radius R and separation $2L$, the Casimir potential reads [22]

$$V = -\frac{23\hbar c}{4\pi \cdot 128L^7} \left(\frac{\varepsilon_r - 1}{\varepsilon_r + 2}\right)^2 R^6. \quad (5.9)$$

The entanglement rate can be obtained similarly as before by expanding the casimir potential between the spheres in small Δx and computing the logarithmic negativity as before:

$$\Gamma_{\text{Casimir}} = T^2 \frac{161}{4096} \frac{cR^6(\Delta x)^2}{\pi L^9 \log 2} \left(\frac{\varepsilon_r - 1}{\varepsilon_r + 2}\right)^2. \quad (5.10)$$

The dependence on T^2 is only a systematic guess but should be sufficient for a basic estimation. Casimir and van der Waals forces are second order effects in the dipole-dipole interaction [25]. Demanding again, that the entanglement due to gravity should be mediated faster than due to Casimir interactions $\Gamma_{\text{Gravity}} > \Gamma_{\text{Casimir}}$, one arrives at the expression

$$T^2 \frac{161cR^6}{256\pi L^6} \left(\frac{\varepsilon_r - 1}{\varepsilon_r + 2}\right)^2 < \frac{GM_A M_B}{\hbar} \quad (5.11)$$

$$\iff d^2 > \frac{4 \cdot 161c\hbar R^6}{256Z_0^2\sigma^2\pi L^6 GM_A M_B} \left(\frac{\varepsilon_r - 1}{\varepsilon_r + 2}\right)^2 \quad (5.12)$$

$$\iff d > \sqrt{\frac{1449}{4096} \frac{c\hbar}{G\pi^3} \frac{2}{Z_0\sigma\rho L^3} \frac{\varepsilon_r - 1}{\varepsilon_r + 2}} \quad (5.13)$$

where again in the last step I assume $M_A = M_B$. For large separations, the shield thickness can go arbitrary low because of the weakness of the casimir interactions at larger distances. Between two silica spheres separated in the order of magnitude as the radius ($L = 2 \times 10^{-5}$ m), the required minimum thickness is between 4×10^{-11} m at 4 K and 10 nm at room temperature. Either way, it is much thinner than a Faraday shield required to shield electrostatic Coulomb interactions. The effect of ε_r was neglected in these numbers. The minimum thickness only changes by a factor between 0 and 1 due to dielectric materials. In fact, these thicknesses are much thinner than recommended, because the shield loses rigidity. It turns out that the vibrational frequency and thus the energy of a thermal shield depends linearly on the thickness and a thinner shield would excite more and larger vibrations. A more detailed discussion of this matter is given in the next section.

5.1.3 Gravitational effects of the shield

The gravitational interaction between the masses and the shield is generally neglected, as it has no influence on the generation of entanglement between the particles. At most, indirect entanglement between the particles, mediated by the thermal oscillations of the shield, is possible, since both masses couple to the shield gravitationally. However, as calculated in section 5.3, this second-order effect is very weak and not problematic at all, since it is still a gravitationally mediated entanglement - which is exactly what the experiment wants to measure anyway. The gravitational force between a sphere with mass M and a infinitesimal mass segment $dm = r\rho_{\text{Cu}}d\varphi$ of the shield made of copper with density $\rho_{\text{Cu}} = 8960 \text{ kg/m}^3$ at a distance r from the center is given by

$$d\mathbf{F} = \frac{GMdm}{\ell} \hat{\ell} \Rightarrow dF_z = \frac{GM r \rho_{\text{Cu}} d}{\ell^2} dr d\varphi \cos \theta, \quad (5.14)$$

where $\ell^2 = r^2 + L^2$ denotes the distance between the sphere and the mass segment and $\theta = \arccos L/\ell$ is the angle between them. The total attractive force between the mass and the shield with radius r_s is therefore

$$F_z = GM\rho_{\text{Cu}}dL \int_0^{r_s} dr \int_0^{2\pi} d\varphi \frac{r}{(r^2 + L^2)^{3/2}} = 2\pi GM\rho_{\text{Cu}}d \left(1 - \frac{L}{\sqrt{L^2 + r_s^2}} \right). \quad (5.15)$$

For large shields $r_s \gg L$ this is independent of the particle-shield separation L . For a shield with thickness $d = 100 \text{ nm}$ and the usual silica particle, the attraction force is around $F_{\text{particle-shield}} \approx 4.1 \times 10^{-24} \text{ N}$ which is comparable with the attraction gravitational attraction force between the two masses at $F_{\text{particle-particle}} \approx 5.0 \times 10^{-24} \text{ N}$ but is much weaker than the Casimir attraction between the particle and the shield with $F_{\text{Casimir}} \approx 1.4 \times 10^{-17} \text{ N}$. Therefore, the gravitational effect of the shield can really be neglected in all practical calculations.

5.2 Thermal shield vibrations

A spherical plate with radius r_s that is fixed at the edge can vibrate in different vibrational modes labeled by the indices (k, l) where $k \in [1, \infty)$ and $l \in [0, \infty)$. The exact vibrational frequency and the mode shape can only be given in terms of the Bessel functions. In fact, one of the first occurrences of these functions can be traced back to Euler trying to solve the very similar problem of a vibrating perfectly flexible membrane [49]. In general, the vibrations of a plate made out of a real material with thickness d can be described by the differential equation [50, p. 490]

$$D\nabla^2\nabla^2 u = -\rho d\ddot{u} \quad (5.16)$$

where D is given by material properties like Youngs module E and the poisson number ν as

$$D = \frac{d^3 E}{12(1 - \nu^2)}. \quad (5.17)$$

The general solution of this differential equation can be written in terms of the Bessel functions as (derived in Ref. [50, p. 490-495])

$$u_{kl}(r, \theta, t) = \left[J_l(\beta_k r) - \frac{J_l(\beta_k r_s)}{I_l(\beta_k r_s)} I_l(\beta_k r) \right] \cos(l\theta + \phi_1) \sin(\omega_{kl}t + \phi_2) \quad (5.18)$$

with

$$\beta_k = \frac{\tilde{r}_k}{r_s} \quad \text{and} \quad \omega_{kl} = \frac{\tilde{r}_k^2}{r_s^2} \sqrt{\frac{D}{\rho d}} = \tilde{r}_k^2 \frac{d}{r_s^2} \sqrt{\frac{E}{12\rho(1-\nu^2)}}, \quad (5.19)$$

where \tilde{r}_k is the k -th solution of the equation

$$J_l(\tilde{r}_k) I_{l+1}(\tilde{r}_k) + I_l(\tilde{r}_k) J_{l+1}(\tilde{r}_k) = 0. \quad (5.20)$$

The phases ϕ_1 and ϕ_2 can be determined by initial conditions and refer to the rotation of the plate as well as temporal offsets. The shape of the first few modes is shown in fig. 5.2. In general, every possible vibration of the plates can be expressed as a sum of these default modes u_{kl} . The amplitude z of the vibrations are determined by the temperature T and can be calculated by treating the amplitude of each vibration as a separate quantum harmonic oscillator with frequency ω_{kl} . The expectation value of the amplitude $\langle z \rangle$ is obviously zero and the variance $(\Delta z)^2 = \langle z^2 \rangle - \langle z \rangle^2$ at temperature T is given by (derivation in appendix C.2)

$$(\Delta \hat{z}_{kl})_T^2 = \frac{\hbar}{2\tilde{m}\omega_{kl}} \coth\left(\frac{\hbar\omega_{kl}}{2k_B T}\right) \approx \frac{k_B T}{\tilde{m}\omega_{kl}^2}. \quad (5.21)$$

In the last step $\hbar\omega \ll k_B T$ was used. \tilde{m} is the *effective mass* of the mode in which the precise shape is considered. A intuitive estimation for this mass can be given by the average amplitude of the mode

$$\tilde{m} = m \frac{1}{\pi r_s^2} \int_0^{r_s} dr \int_0^{2\pi} r d\theta u_{kl}(r, \theta, t) \quad (5.22)$$

with $m = \rho\pi r_s^2 d$ being the total mass of the shield. The amplitude of the plate vibrations are therefore in the order of $\Delta z_{kl} \propto \omega^{-1}$ at high temperatures or for low frequencies.

The effect of individual modes

For a shield with radius $r_s = 1$ cm (in the following referred to as the “large shield”) and thickness $d = 100$ nm made out of Copper with $E = 110$ GPa and $\nu = 1/3$, the frequencies for the first few modes are between 11.0 s^{-1} for $(1, 0)$ up to 1018 s^{-1} for like $(7, 6)$. These frequencies and thus the energy of the vibration $\hbar\omega$ is very small compared to the thermal energy $k_B T$ at all reasonable temperatures. This means, that one expects a lot of modes to be substantially populated. Even at temperatures of 10^{-6} K, the first

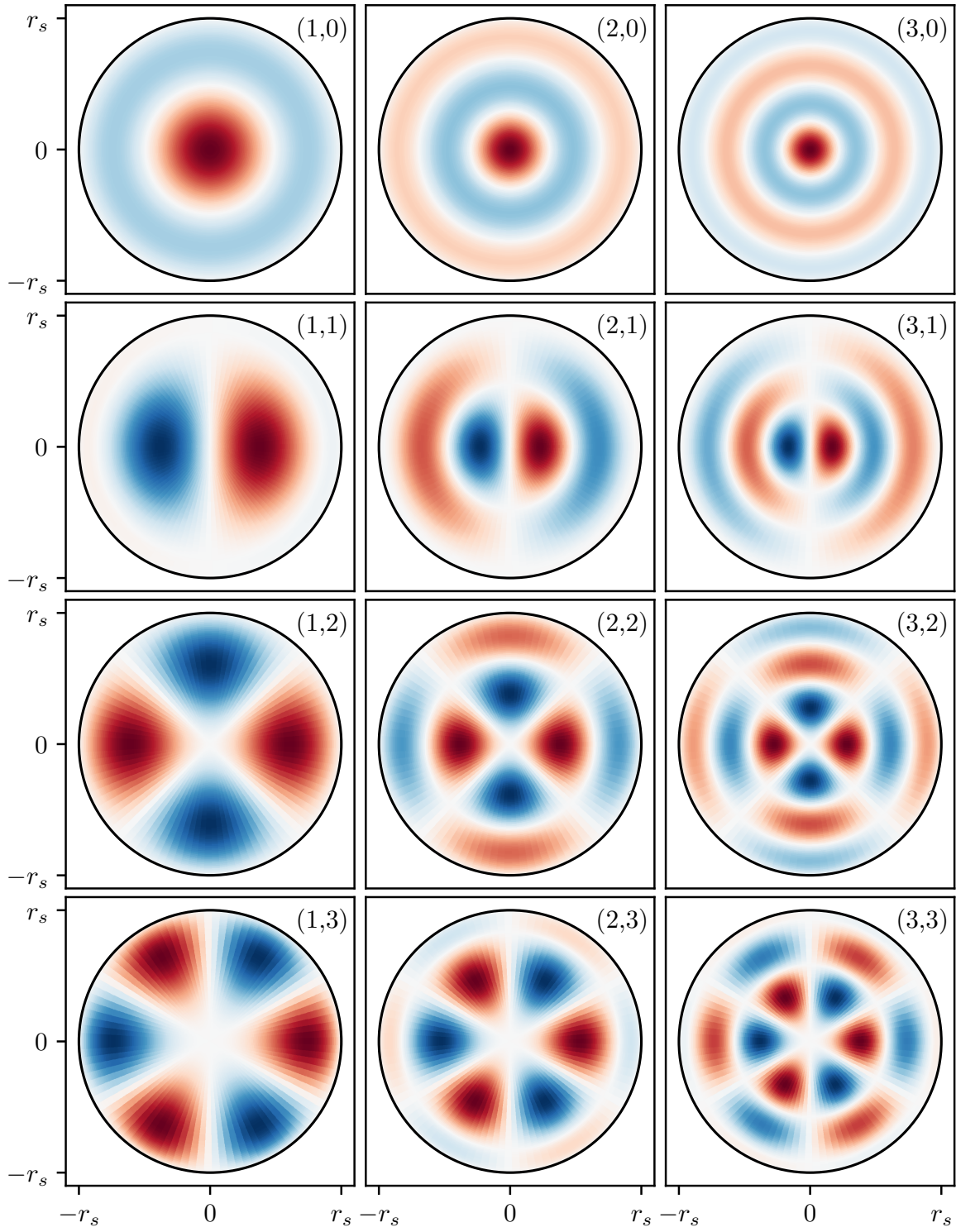


Figure 5.2: Shape of the first 12 modes (k, l) ($k \geq 1$ and $l \geq 0$) of a vibrating spherical plate fixed at the edge with $r_s/d = 1000$.

600 modes are all equally likely to occur with a probability of $\approx 1/Z$ where Z is the partition function

$$Z = \sum_{m \in \{(k,l)\}} e^{-\beta \hbar \omega_m}. \quad (5.23)$$

It is possible to calculate the asymptotic increase in the frequencies ω_{kl} for high modes $k \rightarrow \infty$. This is, because the behavior for large inputs of the Bessel functions [51, eq. 10.17.3]

$$J_l(x) \sim \cos\left(x - \frac{l\pi}{2} - \frac{\pi}{4}\right) \quad \text{for } x \rightarrow \infty \quad (5.24)$$

and modified Bessel functions [51, eq. 10.40.1]

$$I_l(x) \sim \frac{e^x}{\sqrt{2\pi x}} \quad \text{for } x \rightarrow \infty \quad (5.25)$$

is known resulting in an asymptotic expansion of eq. (5.20)

$$\sim \frac{e^x}{\sqrt{2\pi x}} \left[\cos\left(x - \frac{l\pi}{2} - \frac{\pi}{4}\right) + \cos\left(x - \frac{l\pi}{2} - \frac{3\pi}{4}\right) \right] = 0. \quad (5.26)$$

Therefore, the distribution of zeros \tilde{r}_k is periodic for large k as well as for large l . The frequencies increase therefore with $\mathcal{O}(k^2 + l^2)$ for large modes. The amplitude $\Delta z_{kl} \propto 1/\omega$ therefore decreases quadratically with increasing mode order. Therefore, even if at reasonable temperatures a lot of modes are occupied, the amplitude and thus the effect of each mode decreases for higher modes. Additionally, because of the consideration of a real vibrating plate, the amplitude of the maximum of the shape u_{kl} decreases for higher modes because the increased number of bulges require more material of the shield limiting the overall amplitude of the vibration even more. Due to all these effects combined, it is sufficient to only consider the first few modes in all subsequent numerical calculations. However the effects of infinity many modes can be estimated asymptotically using the known scaling of ω_{kl} with increasing modes (k, l) .

It is also interesting to consider the scaling of the amplitudes Δz for differently sized shields. According to eq. (5.19), the frequency ω increases quadratically with decreasing shield radius r_s . However, the effective mass \tilde{m} eq. (5.22) depends also quadratically on the size of the shield resulting in a total dependence of $\Delta z \sim r_s$ for large temperatures and/or low modes.

5.3 Entanglement in front of a thermal shield

The entanglement generation between the two particles depends heavily on the variation of the separation between the shield and the particles, as has been seen in chapter 4. The vibrating shield can be interpreted as varying the separation and angle of the cat-state in front of the plate - visualized in fig. 5.3. This is only a good approximation for shields

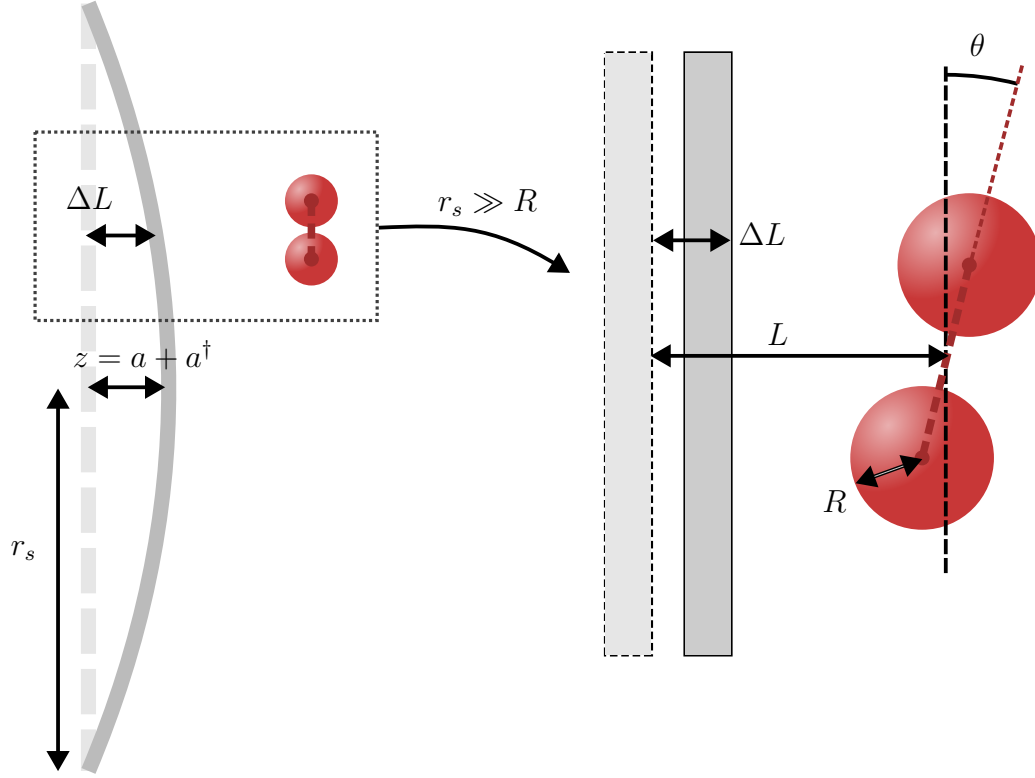


Figure 5.3: For a large $r_s \gg R$ and locally flat shield, the thermal vibrations with amplitude z can be interpreted as a static shield where the particle A (shown in the figure) is placed at $L + \Delta L$ at angle θ and particle B is placed at $L - \Delta L$ with angle $-\theta$ where both variations depend on the amplitude. At low vibrational frequencies $1/\omega \approx t_{\max}$ the amplitude can be assumed to be static during a experimental run and for each measurement thermally distributed around $\langle z \rangle = 0$ with Δz given by eq. (5.21).

larger than the particles radius $r_s \gg R$ and low vibrating frequencies $1/\omega \approx t_{\max}$ and can therefore be used well to describe the highly disturbing first few modes on a large shield. Furthermore, this interpretation is possible because as shown in section 3.3, the Casimir interaction between a sphere and a tilted plane does not differ from the interaction between a flat plane. Contrary to the problem considered in chapter 4, here only the thermal amplitude z_{kl} is a independent random variable distributed around $\langle z_{kl} \rangle = 0$ with standard deviation Δz_{kl} given by eq. (5.21). Both, the variations in the particle-shield separation ΔL as well as in the angle θ are correlated to the amplitude z . For a large shield, this can be understood as

$$\theta = \arctan(z |\nabla u|) \approx z |\nabla u| \quad \text{and} \quad \Delta L = z |u| \quad (5.27)$$

where ∇u is the gradient of the shape of the vibrational mode. Performing similar calculations as done before in chapter 4, the averaged density matrix $\langle \rho \rangle$ dependent on Δz_{kl} can be calculated. The entanglement quantified by the logarithmic negativity [19] introduced in section 2.2 dependent on the temperature T is shown in fig. 5.4. This is not

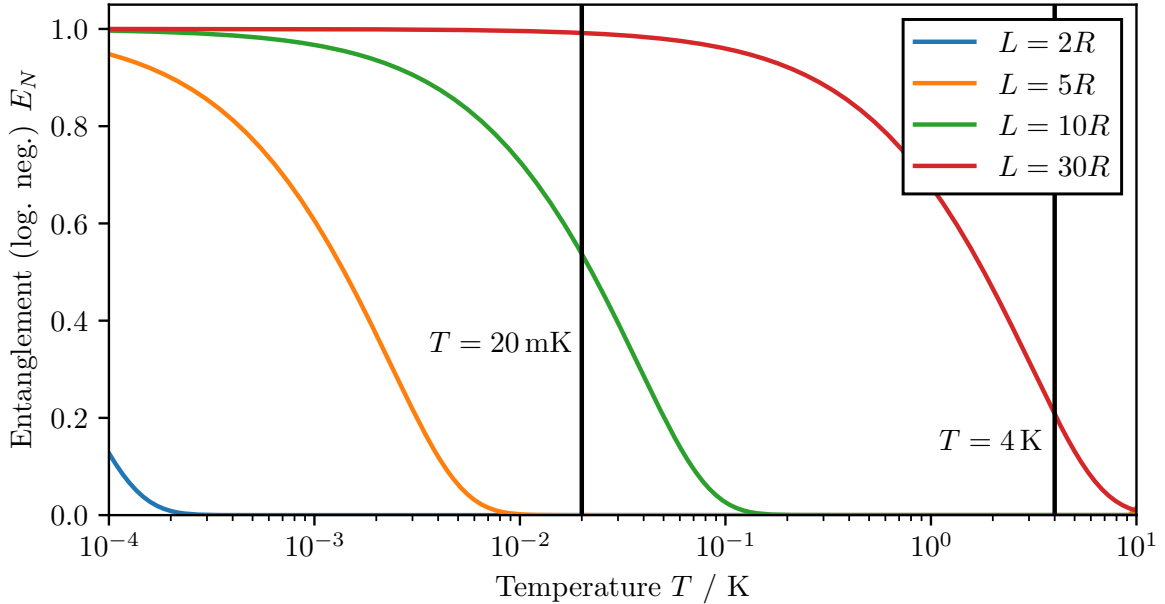


Figure 5.4: Entanglement between the particles (parallel orientation) in front of a thermal shield in the first mode (1,0) at temperature T for different particle-shield separations L .

surprising considering that the thermal amplitudes $\Delta z_{1,0} \approx 9 \times 10^{-11}$ m at 20 mK which is comparable with the previously calculated values for ΔL_{crit} in chapter 4. Surprisingly this result does not change for different shield radii - at least as long as the condition $r_s \ll R$ is fulfilled and the shield shape can locally be linearized. This is because the gradient $|\nabla u| \propto 1/r_s$ which perfectly cancels with the dependence on $z \propto r_s$ leaving θ independent of r_s . If the cat-state orientation is now chosen parallel to the shield, the

dependence on ΔL is irrelevant leaving the final resulting entanglement independent of r_s .

5.3.1 Analytic dynamics

Surprisingly the influence of the thermal shield on entanglement generation can be calculated analytically.

$$\begin{aligned} \hat{H} = \sum_{\substack{m \in \{(k,l)\} \\ k \geq 1, l \geq 0}} \hbar \omega_m \left(\hat{a}_m^\dagger \hat{a}_m + \frac{1}{2} \right) \\ + \left[g_{\text{Grav}}^{1,1} + \left(g_{\text{A,m,Cas}}^1 + g_{\text{B,m,Cas}}^1 \right) (\hat{a}_m + \hat{a}_m^\dagger) \right] \left| \psi_A^1 \psi_B^1 \right\rangle \left\langle \psi_A^1 \psi_B^1 \right| \\ + \left[g_{\text{Grav}}^{1,2} + \left(g_{\text{A,m,Cas}}^1 + g_{\text{B,m,Cas}}^2 \right) (\hat{a}_m + \hat{a}_m^\dagger) \right] \left| \psi_A^1 \psi_B^2 \right\rangle \left\langle \psi_A^1 \psi_B^2 \right| \\ + \left[g_{\text{Grav}}^{2,1} + \left(g_{\text{A,m,Cas}}^2 + g_{\text{B,m,Cas}}^1 \right) (\hat{a}_m + \hat{a}_m^\dagger) \right] \left| \psi_A^2 \psi_B^1 \right\rangle \left\langle \psi_A^2 \psi_B^1 \right| \\ + \left[g_{\text{Grav}}^{2,2} + \left(g_{\text{A,m,Cas}}^2 + g_{\text{B,m,Cas}}^2 \right) (\hat{a}_m + \hat{a}_m^\dagger) \right] \left| \psi_A^2 \psi_B^2 \right\rangle \left\langle \psi_A^2 \psi_B^2 \right| \end{aligned} \quad (5.28)$$

where g_{Grav}^{ij} is the gravitational coupling between the states $|\psi_A^i\rangle$ and $|\psi_B^j\rangle$. The Casimir interaction between state $|\psi_{A(B)}^i\rangle$ and the shield is denoted by $\tilde{g}_{\text{A(B),m,Cas}}^i$. These couplings are dependent on the amplitude $\hat{z}_m = \sqrt{\hbar/2\tilde{m}\omega_m}(\hat{a}_m + \hat{a}_m^\dagger)$ and the shape $u_m(r_{A(B)})$ of the vibrational mode $m = \{(k, l)\}$ at the position $r_{A(B),i}$ of the cat state:

$$\tilde{g}_{\text{A(B),m,Cas}}^i = \frac{\hbar c \pi^3}{720} \left(\frac{\varepsilon_r - 1}{\varepsilon_r + 1} \right) \varphi(\varepsilon_r) \frac{R}{(\mathcal{L} + \hat{z}_m u_m(r))^2} \approx g_{\text{PFA}} \left(\frac{1}{\mathcal{L}^2} + \frac{2\hat{z}_m u_m(r_{A(B),i})}{\mathcal{L}^3} \right). \quad (5.29)$$

Ignoring the first term in the expansion, which just produces a global phase in the evolved system, the couplings g_{Cas} appearing in eq. (5.28) are finally given by

$$g_{\text{A(B),m,Cas}}^i = g_{\text{PFA}} \frac{2u_m(r_{A(B),i})}{\mathcal{L}^3} \sqrt{\frac{\hbar}{2\tilde{m}\omega_m}}. \quad (5.30)$$

It is possible to analytically calculate the time evolution of a system consisting of the initial state ρ_{system} (given by eq. (2.7)) combined with the infinite vibrational modes ρ_{th} of the thermal shield

$$\rho_0 = \bigotimes_{m \in \{(k,l)\}} (\rho_{\text{th},m}) \otimes \rho_{\text{system}}. \quad (5.31)$$

These thermal states can be expanded into coherent states $|\alpha\rangle = \hat{D}(\alpha)|0\rangle$ as [52]

$$\rho_{\text{th},m} = \frac{1}{Z} \sum_{n=1}^{\infty} e^{-\beta \hbar \omega_m (n+1/2)} |n\rangle \langle n| = \int d\alpha^2 \frac{1}{\pi \bar{n}} e^{-\frac{|\alpha|^2}{\bar{n}}} |\alpha\rangle \langle \alpha| \quad (5.32)$$

where \bar{n} is the average occupation number. The time evolution of the particle-system $\rho_{\text{system}}(t) = \text{tr}_{\text{th}} \{\rho(t)\}$ can be calculated by tracing out all states corresponding to the thermal shield.

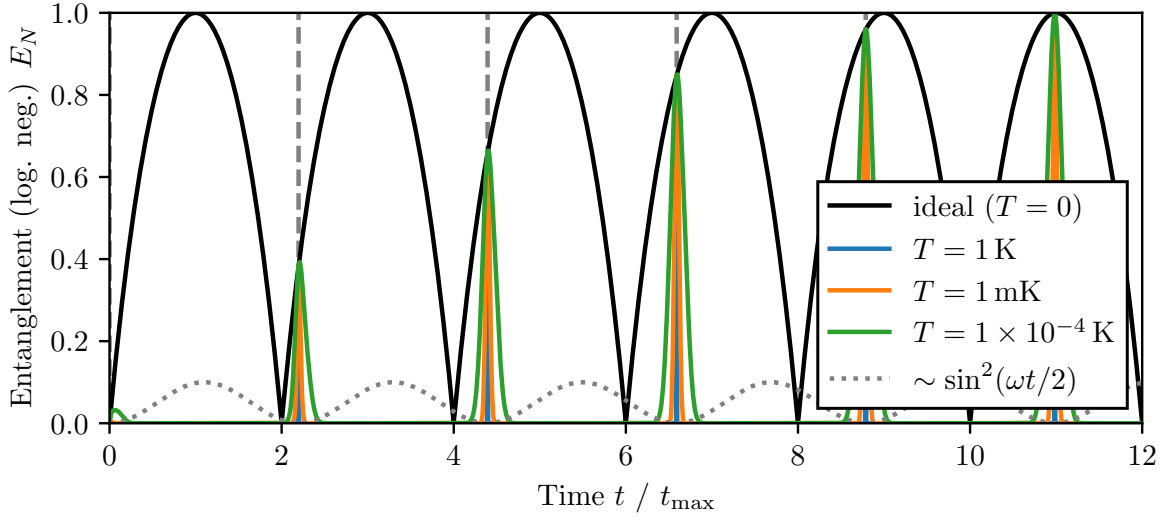


Figure 5.5: Entanglement dynamics in front of a thermal shield in mode $(1, 0)$ at different temperatures. Only at specific times $2\pi k/\omega_{1,0}$, $k \in \mathbb{N}$, entanglement is observable. This behavior is expected and aligns with the findings in Ref. [53].

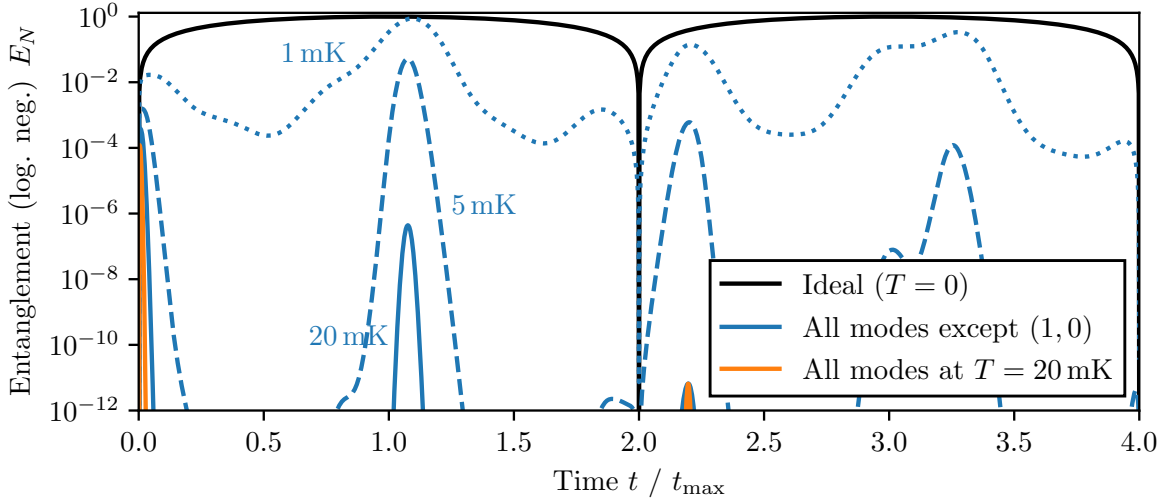


Figure 5.6: Entanglement dynamics in front of a thermal shield. In orange, the first 50 modes have been used in the numeric calculation. The effect of all remaining modes is around $1.7 \times 10^{-11} \%$. In blue, all modes except the first mode $(1, 0)$ have been considered at different temperatures ranging from 1 mK up to 20 mK. The particle-shield separation is fixed at $L = 2R = 20 \mu\text{m}$.

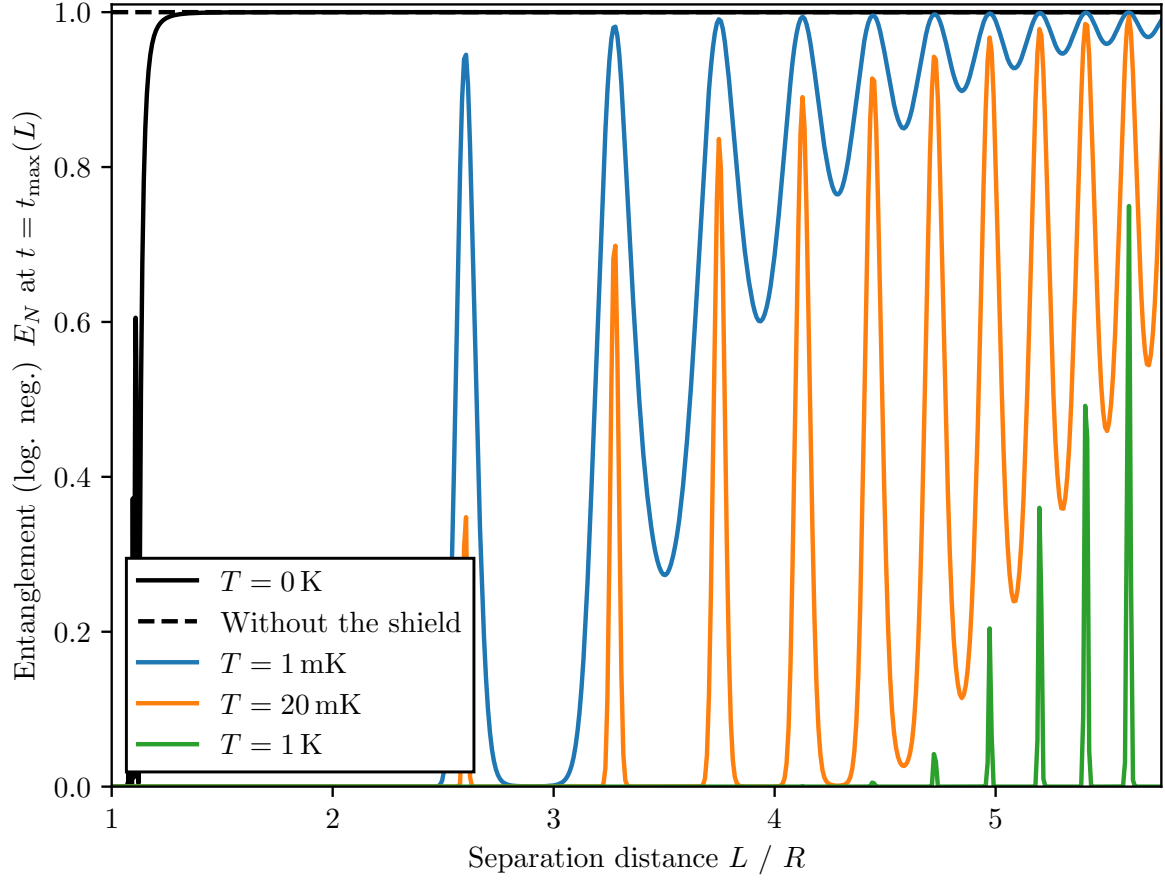


Figure 5.7: All modes, Entanglement at t-max

5.3.2 Small shields

5.4 Discussions on the shield

- ****Charged or uncharged**** Compare requirements in size and thickness as well as thermal vibrations, which are less a problem for smaller shields
- Small shield = local casimir effect. Compare with sec. 3.3
- How large are the effects of thermal vibration and how bad is everything (Maybe in the next section, otherwise a little bit chaotic)
- Maybe a cross-structure or a different geometry of the shield could reduce vibrations and a larger shield might be okay. But local structures again
- Rectangular plate (frequencies only one order of magnitude ($\sqrt{\pi^4}$) better -i no real improvements)
- Possible to measure casimir forces with a similar technique of dephasing (very sensitive)

6 Discussion and outlook

- Squeezed states (similar to cat states) [10]
- Possible to measure casimir interactions using dephasing and so on with similar methods

Bibliography

- [1] N. Maskelyne, “A proposal for measuring the attraction of some hill in this kingdom by astronomical observations”, *Philosophical Transactions of the Royal Society of London* **65**, 495–499 (1775) 10.1098/rstl.1775.0049.
- [2] R. D. Davies, “A Commemoration of Maskelyne at Schiehallion”, *Quarterly Journal of the Royal Astronomical Society* **26**, 289–294 (1985).
- [3] T. Krisnanda, G. Y. Tham, M. Paternostro, and T. Paterek, “Observable quantum entanglement due to gravity”, *npj Quantum Information* **6**, 10.1038/s41534-020-0243-y (2019) 10.1038/s41534-020-0243-y, arXiv:1906.08808.
- [4] H. Chevalier, A. J. Paige, and M. S. Kim, “Witnessing the nonclassical nature of gravity in the presence of unknown interactions”, *Physical Review A* **102**, 022428 (2020) 10.1103/physreva.102.022428, arXiv:2005.13922.
- [5] J. S. Pedernales, G. W. Morley, and M. B. Plenio, “Motional Dynamical Decoupling for Matter-Wave Interferometry”, *Phys. Rev. Lett.* **125**, 023602 (2019) 10.1103/physrevlett.125.023602, arXiv:1906.00835.
- [6] S. Bose, A. Mazumdar, G. W. Morley, H. Ulbricht, M. Toroš, M. Paternostro, A. Geraci, P. Barker, M. S. Kim, and G. Milburn, “A Spin Entanglement Witness for Quantum Gravity”, *Phys. Rev. Lett.* **119**, 240401 (2017) 10.1103/physrevlett.119.240401, arXiv:1707.06050.
- [7] L. Lami, J. S. Pedernales, and M. B. Plenio, “Testing the quantum nature of gravity without entanglement”, *Phys. Rev. X* **14**, 021022 (2023) 10.1103/physrevx.14.021022, arXiv:2302.03075.
- [8] R. Horodecki, P. Horodecki, M. Horodecki, and K. Horodecki, “Quantum entanglement”, *Rev. Mod. Phys.* **81**, 865–942 (2007) 10.1103/revmodphys.81.865, arXiv:quant-ph/0702225.
- [9] M. B. Plenio and S. Virmani, “An introduction to entanglement measures”, *Quantum Information & Computation* **7**, 1–51 (2005), arXiv:quant-ph/0504163.
- [10] J. S. Pedernales and M. B. Plenio, “On the origin of force sensitivity in tests of quantum gravity with delocalised mechanical systems”, *Contemporary Physics* **64**, 147–163 (2023) 10.1080/00107514.2023.2286074, arXiv:2311.04745.
- [11] D. Carney, P. C. E. Stamp, and J. M. Taylor, “Tabletop experiments for quantum gravity: a user’s manual”, *Classical and Quantum Gravity* **36**, 034001 (2018) 10.1088/1361-6382/aaf9ca, arXiv:1807.11494.

- [12] M. Christodoulou, A. Di Biagio, M. Aspelmeyer, Č. Brukner, C. Rovelli, and R. Howl, “Locally mediated entanglement in linearised quantum gravity”, *Physical Review Letters* **130**, 100202 (2022) 10.1103/physrevlett.130.100202, arXiv:2202.03368.
- [13] Y. Y. Fein, P. Geyer, P. Zwick, F. Kiałka, S. Pedalino, M. Mayor, S. Gerlich, and M. Arndt, “Quantum superposition of molecules beyond 25 kDa”, *Nature Physics* **15**, 1242–1245 (2019) 10.1038/s41567-019-0663-9.
- [14] T. Westphal, H. Hepach, J. Pfaff, and M. Aspelmeyer, “Measurement of Gravitational Coupling between Millimeter-Sized Masses”, *Nature* **591**, 225–228 (2021) 10.1038/s41586-021-03250-7, arXiv:2009.09546.
- [15] H. B. G. Casimir, “On the attraction between two perfectly conducting plates”, *Proc. Kon. Ned. Akad. Wet.* **51**, 793 (1948).
- [16] H. B. G. Casimir and D. Polder, “The Influence of Retardation on the London-van der Waals Forces”, *Physical Review* **73**, 360–372 (1948) 10.1103/physrev.73.360.
- [17] L. Gurvits, “Classical deterministic complexity of Edmonds’ problem and Quantum Entanglement”, in *Proceedings of the thirty-fifth annual acm symposium on theory of computing*, Vol. 4, STOC03 (June 2003), pages 10–19, 10.1145/780542.780545, arXiv:quant-ph/0303055.
- [18] G. Vidal and R. F. Werner, “A computable measure of entanglement”, *Phys. Rev. A* **65**, 032314 (2001) 10.1103/physreva.65.032314, arXiv:quant-ph/0102117.
- [19] M. Plenio, “Logarithmic negativity: a full entanglement monotone that is not convex.”, *Physical Review Letters* **95**, 090503 (2005) 10.1103/PhysRevLett.95.090503, arXiv:quant-ph/0505071.
- [20] R. L. DeBiase, “Are Casimir Forces Conservative?”, *Physics Procedia* **38**, 18–33 (2012) 10.1016/j.phpro.2012.08.008.
- [21] B. Yi, U. Sinha, D. Home, A. Mazumdar, and S. Bose, “Massive spatial qubits: Testing macroscopic nonclassicality and Casimir entanglement”, *Physical Review Research* **5**, 033202 (2023) 10.1103/physrevresearch.5.033202, arXiv:2106.11906.
- [22] T. Emig, N. Graham, R. L. Jaffe, and M. Kardar, “Casimir forces between arbitrary compact objects”, *Phys. Rev. Lett.* **99**, 170403 (2007) 10.1103/physrevlett.99.170403, arXiv:0707.1862.
- [23] T. W. van de Kamp, R. J. Marshman, S. Bose, and A. Mazumdar, “Quantum Gravity Witness via Entanglement of Masses: Casimir Screening”, *Phys. Rev. A* **102**, 062807 (2020) 10.1103/physreva.102.062807, arXiv:2006.06931.
- [24] F. London, “Zur Theorie und Systematik der Molekularkräfte”, *Zeitschrift für Physik* **63**, 245–279 (1930) 10.1007/bf01421741.

- [25] M. Bordag, U. Mohideen, and V. M. Mostepanenko, “New developments in the Casimir effect”, *Physics Reports* **353**, 1–205 (2001) 10.1016/s0370-1573(01)00015-1, arXiv:quant-ph/0106045 [quant-ph].
- [26] G. L. Klimchitskaya, U. Mohideen, and V. M. Mostepanenko, “The Casimir force between real materials: Experiment and theory”, *Reviews of Modern Physics* **81**, 1827–1885 (2009) 10.1103/revmodphys.81.1827, arXiv:0902.4022.
- [27] S. K. Lamoreaux, “The Casimir force: background, experiments, and applications”, *Reports on Progress in Physics* **68**, 201–236 (2004) 10.1088/0034-4885/68/1/r04.
- [28] M. Bordag, “Proceedings of the Fourth Workshop on Quantum Field Theory under the Influence of External Conditions”, in *The Casimir Effect 50 Years Later* (June 1999), pages 1–410, 10.1142/9789814527576.
- [29] L. H. Ford, “Casimir Force between a Dielectric Sphere and a Wall: A Model for Amplification of Vacuum Fluctuations”, *Phys. Rev. A* **58**, 4279–4286 (1998) 10.1103/physreva.58.4279, arXiv:quant-ph/9804055.
- [30] E. M. Lifshitz, “The theory of molecular attractive forces between solids”, *Sov. Phys. JETP* **2**, 73–83 (1956) 10.1016/b978-0-08-036364-6.50031-4.
- [31] M. Hartmann, “Casimir effect in the plane-spheregeometry: Beyond the proximityforce approximation”, PhD thesis (Universität Augsburg, July 2018).
- [32] T. Emig, “Fluctuation induced quantum interactions between compact objects and a plane mirror”, *Journal of Statistical Mechanics: Theory and Experiment* **2008**, P04007 (2007) 10.1088/1742-5468/2008/04/p04007, arXiv:0712.2199.
- [33] A. Bulgac, P. Magierski, and A. Wirzba, “Scalar Casimir effect between Dirichlet spheres or a plate and a sphere”, *Physical Review D* **73**, 025007 (2006) 10.1103/physrevd.73.025007.
- [34] I. G. Pirozhenko and M. Bordag, “On the Casimir repulsion in sphere-plate geometry”, *Physical Review D* **87**, 085031 (2013) 10.1103/physrevd.87.085031, arXiv:1302.5290.
- [35] K. Perlin, “An image synthesizer”, *SIGGRAPH Comput. Graph.* **19**, 287–296 (1985) 10.1145/325165.325247.
- [36] K. F. Riley, *Mathematical methods for physics and engineering*, edited by M. P. Hobson and S. J. Bence, Third edition, Hier auch später erschienene, unveränderte Nachdrucke (Cambridge University Press, Cambridge, 2018), 1333 pages.
- [37] A. C. Berry, “The accuracy of the Gaussian approximation to the sum of independent variates”, *Transactions of the American Mathematical Society* **49**, 122–136 (1941) 10.1090/s0002-9947-1941-0003498-3.
- [38] M. Aspelmeyer, *Quantum sources of gravity: the next frontier of macroscopic quantum physics*, <https://www.youtube.com/watch?v=0AVDrVY-rTw>, Timestamp: 51:00, May 2024.

- [39] A. D. O’Connell, M. Hofheinz, M. Ansmann, R. C. Bialczak, M. Lenander, E. Lucero, M. Neeley, D. Sank, H. Wang, M. Weides, J. Wenner, J. M. Martinis, and A. N. Cleland, “Quantum ground state and single-phonon control of a mechanical resonator”, *Nature* **464**, 697–703 (2010) 10.1038/nature08967.
- [40] K. C. Lee, M. R. Sprague, B. J. Sussman, J. Nunn, N. K. Langford, X.-M. Jin, T. Champion, P. Michelberger, K. F. Reim, D. England, D. Jaksch, and I. A. Walmsley, “Entangling Macroscopic Diamonds at Room Temperature”, *Science* **334**, 1253–1256 (2011) 10.1126/science.1211914.
- [41] M. Bild, M. Fadel, Y. Yang, U. von Lüpke, P. Martin, A. Bruno, and Y. Chu, “Schrödinger cat states of a 16-microgram mechanical oscillator”, *Science* **380**, 274–278 (2022) 10.1126/science.adf7553, arXiv:2211.00449.
- [42] D. Grass, J. Fesel, S. G. Hofer, N. Kiesel, and M. Aspelmeyer, “Optical trapping and control of nanoparticles inside evacuated hollow core photonic crystal fibers”, *Applied Physics Letters* **108**, 10.1063/1.4953025 (2016) 10.1063/1.4953025, arXiv:1603.09393.
- [43] B. R. Slezak, C. W. Lewandowski, J.-F. Hsu, and B. D’Urso, “Cooling the motion of a silica microsphere in a magneto-gravitational trap in ultra-high vacuum”, *New Journal of Physics* **20**, 063028 (2018) 10.1088/1367-2630/aacac1, arXiv:1802.03424 [quant-ph].
- [44] C. Gonzalez-Ballester, M. Aspelmeyer, L. Novotny, R. Quidant, and O. Romero-Isart, “Levitodynamics: levitation and control of microscopic objects in vacuum”, *Science* **374**, 10.1126/science.abg3027 (2021) 10.1126/science.abg3027, arXiv:2111.05215.
- [45] W. P. Schleich, “Waves à la WKB”, in *Quantum Optics in Phase Space* (John Wiley & Sons, Ltd, Berlin, Feb. 2001) Chap. 5, pages 153–169.
- [46] G. A. E. Vandenbosch, “The basic concepts determining electromagnetic shielding”, *American Journal of Physics* **90**, 672–681 (2022) 10.1119/5.0087295.
- [47] R. Berman, D. K. C. Macdonald, and F. E. Simon, “The thermal and electrical conductivity of copper at low temperatures”, *Proceedings of the Royal Society of London. Series A. Mathematical and Physical Sciences* **211**, 122–128 (1952) 10.1098/rspa.1952.0029.
- [48] R. Gross and A. Marx, *Festkörperphysik*, 3., akt. Aufl, De Gruyter Studium (De Gruyter, Berlin, 2018), 11066 pages.
- [49] J. Dutka, “On the Early History of Bessel Functions”, *Archive for History of Exact Sciences* **49**, 105–134 (1995).
- [50] S. S. Rao, *Vibration of Continuous Systems*, 2nd Edition (Wiley, Jan. 2019), 10.1002/9781119424284.

Bibliography

- [51] F. W. J. Olver, A. B. Olde Daalhuis, D. W. Lozier, B. I. Schneider, R. F. Boisvert, C. W. Clark, B. R. Miller, B. V. Saunders, H. S. Cohl, M. A. McClain, and eds., ***NIST Digital Library of Mathematical Functions***, <https://dlmf.nist.gov/>, Release 1.2.2 of 2024-09-15, 2024.
- [52] M. O. E. Steiner, J. S. Pedernales, and M. B. Plenio, “Pentacene-Doped Naphthalene for Levitated Optomechanics”, 10.48550/ARXIV.2405.13869 (2024) 10.48550/ARXIV.2405.13869, arXiv:2405.13869 [quant-ph].
- [53] J. S. Pedernales, K. Streltsov, and M. B. Plenio, “Enhancing Gravitational Interaction between Quantum Systems by a Massive Mediator”, Physical Review Letters **128**, 110401 (2021) 10.1103/physrevlett.128.110401, arXiv:2104.14524.
- [54] M. A. Nielsen and I. L. Chuang, ***Quantum computation and quantum information***, 10th anniversary ed. (Cambridge University Press, Cambridge, 2010), 1676 pages.
- [55] D. J. Griffiths, ***Elektrodynamik, Eine Einführung***, edited by U. Schollwöck, 4th edition (Pearson, Hallbergmoos, 2018), 1711 pages.
- [56] S. Blanes, F. Casas, J. A. Oteo, and J. Ros, “The Magnus expansion and some of its applications”, Physics Reports **470**, 151–238 (2008) 10.1016/j.physrep.2008.11.001, arXiv:0810.5488 [math-ph].

A TITLE TO BE DONE

A.1 Evolution under a gravitational Hamiltonian

In this section the time evolution of a system under Hamiltonian eq. (2.3) is calculated a) using the gravitational interaction \hat{H}_G as a perturbation b) using an exact time evolution of coherent states.

A.1.1 Using time dependent perturbation theory

A general biparty Fock state $|\psi_0\rangle = |kl\rangle$ with $k, l \in \mathbb{N}_0$ can be evolved in time under a Hamiltonian eq. (2.3) treating the gravitational interaction $H_G = -\hbar g(\hat{a}_1\hat{a}_2^\dagger + \hat{a}_1^\dagger\hat{a}_2)$ as a perturbation. The resulting state $|\psi(t)\rangle$ after some time t is in the most general form given as

$$|\psi(t)\rangle = \sum_{i,j \geq 0} c_{i,j}(t) |i, j\rangle \quad (\text{A.1})$$

where the coefficients $c_{i,j}(t)$ are given by first order perturbation theory as

$$c_{i,j}(t) = c_{i,j}(t=0) - \frac{i}{\hbar} \int_0^t dt' \langle ij | \hat{H}_G | kl \rangle e^{-i(E_{kl} - E_{ij})t'/\hbar}. \quad (\text{A.2})$$

The exponent is given by the energy of the appropriate Fock states $E_{kl} - E_{ij} = \hbar\omega(k + l - (i + j))$ and the matrix element in the integrand can be calculated to

$$\langle ij | \hat{H}_G | kl \rangle = \begin{cases} -\hbar g & \text{if } i = k \pm 1 \text{ and } j = l \mp 1 \\ 0 & \text{otherwise} \end{cases}. \quad (\text{A.3})$$

The coefficients for $t = 0$ are trivially given from the initial state as

$$c_{i,j}(t=0) = \begin{cases} 1 & \text{for } i, j = k, l \\ 0 & \text{otherwise} \end{cases}. \quad (\text{A.4})$$

For the non-zero states the energies in the exponent equate to zero and the evolved state is given by (up to a normalization)

$$|\psi(t)\rangle = |kl\rangle - igt |k-1, l+1\rangle - igt |k+1, l-1\rangle + \mathcal{O}(g^2). \quad (\text{A.5})$$

The result eq. (2.5) is represented by eq. (A.5) for the case of $k = 1$ and $l = 0$.

A.1.2 Using an exact time evolution

The Hamiltonian eq. (2.3) can be rewritten using symmetric and antisymmetric normal modes

$$\hat{a}_{\pm} = \frac{1}{\sqrt{2}}(\hat{a}_1 \pm \hat{a}_2) \quad (\text{A.6})$$

in the form of

$$\hat{H} = \hbar\omega_+ \hat{a}_+^\dagger \hat{a}_+ + \hbar\omega_- \hat{a}_-^\dagger \hat{a}_-, \quad \omega_{\pm} = \omega \pm (-g) \quad (\text{A.7})$$

The initial state consisting of two coherent oscillator states is in the new modes given by

$$|\psi(t)\rangle = |\alpha\rangle_1 |\beta\rangle_2 = \left| \frac{1}{\sqrt{2}}(\alpha + \beta) \right\rangle_+ \left| \frac{1}{\sqrt{2}}(\alpha - \beta) \right\rangle_- \quad (\text{A.8})$$

A general coherent state $|\gamma\rangle$ evolves in time under an Hamiltonian $\hat{H} = \hbar\omega \hat{a}^\dagger \hat{a}$ like $|\gamma(t)\rangle = |e^{-i\omega t}\gamma\rangle$ which can be used to evolve the state in eq. (A.8):

$$|\psi(t)\rangle = \left| \frac{1}{\sqrt{2}}e^{-i\omega_+ t}(\alpha + \beta) \right\rangle_+ \left| \frac{1}{\sqrt{2}}e^{-i\omega_- t}(\alpha - \beta) \right\rangle_- \quad (\text{A.9})$$

$$= |e^{-i\omega t}(\alpha \cos gt - \beta \sin gt)\rangle_1 |e^{-i\omega t}(-\alpha \sin gt + \beta \cos gt)\rangle_2, \quad (\text{A.10})$$

where in the last line the back-transformation from the \pm -modes (A.8) was used.

A.2 Exemplary calculation of E_N

In this section, the logarithmic negativity E_N eq. (2.21) is exemplary calculated for the state eq. (2.13). The density matrix of this system is given by

$$\rho(t) = |\psi(t)\rangle\langle\psi(t)| = \frac{1}{4} \begin{pmatrix} 1 & e^{i\Delta\phi} & e^{i\Delta\phi} & 1 \\ e^{-i\Delta\phi} & 1 & 1 & e^{-i\Delta\phi} \\ e^{-i\Delta\phi} & 1 & 1 & e^{-i\Delta\phi} \\ 1 & e^{i\Delta\phi} & e^{i\Delta\phi} & 1 \end{pmatrix}. \quad (\text{A.11})$$

Consequently, the partially transposed density ρ^{Γ_B} is given by

$$\rho^{\Gamma_B}(t) = \frac{1}{4} \begin{pmatrix} 1 & e^{-i\Delta\phi} & e^{i\Delta\phi} & 1 \\ e^{i\Delta\phi} & 1 & 1 & e^{-i\Delta\phi} \\ e^{-i\Delta\phi} & 1 & 1 & e^{i\Delta\phi} \\ 1 & e^{i\Delta\phi} & e^{-i\Delta\phi} & 1 \end{pmatrix}. \quad (\text{A.12})$$

The eigenvalues were calculated using `Mathematica` and equate to

$$\left\{ \sin^2\left(\frac{\Delta\phi}{2}\right), \cos^2\left(\frac{\Delta\phi}{2}\right), \frac{\sin \Delta\phi}{2}, -\frac{\sin \Delta\phi}{2} \right\}$$

According to lemma 2.1, $\|\rho^{\Gamma_B}\|_1$ is given by the sum of the absolute eigenvalues, which is equal to $1 + |\sin \Delta\phi|$. The negativity as the absolute sum of all negative eigenvalues (demonstrated in proposition 2.3) equates to $\mathcal{N} = |\sin \Delta\phi|/2$. Both methods result in a logarithmic negativity of $E_N = \log_2(1 + |\sin \Delta\phi|)$.

B Casimir interactions

B.1 Polarizability of a dielectric sphere

The polarizability α is defined via

$$\mathbf{E}_\infty \alpha = \mathbf{p}, \quad (\text{B.1})$$

where \mathbf{p} is the induced dipole moment and \mathbf{E}_∞ is the external electric field that induces the dipole moment. For a linear and uniform dielectric, it is given as $\mathbf{p} = \mathcal{V} \varepsilon_0 (\varepsilon_r - 1) \mathbf{E}_\text{in}$ [55, p. 220-226]. Here, \mathcal{V} is the volume of the object and \mathbf{E}_in is the electric field inside the dielectric. The electrostatic boundary conditions for the problem are given by

$$V_\text{in}|_{r=R} = V_\text{out}|_{r=R} \quad \text{and} \quad \varepsilon_r \varepsilon_0 \frac{\partial V_\text{in}}{\partial r} \Big|_{r=R} = \varepsilon_0 \frac{\partial V_\text{out}}{\partial r} \Big|_{r=R} \quad (\text{B.2})$$

and the electric potential outside of the sphere at $r \rightarrow \infty$ should be equal to the external dipole-inducing field $V_\text{out}|_{r \rightarrow \infty} = -\mathbf{E}_\infty \cdot \mathbf{r} = -E_\infty r \cos \theta$. The electric potential inside and outside the sphere can be calculated using the spherical decomposition of the general electric potential $V \propto 1/|\mathbf{r} - \mathbf{r}'|$ into Legendre Polynomials P_l [55, p. 188-190]:

$$V_\text{in}(r, \theta) = -E_\infty r \cos \theta + \sum_{l=0}^{\infty} A_l r^l P_l(\cos \theta), \quad (\text{B.3})$$

$$V_\text{out}(r, \theta) = -E_\infty r \cos \theta + \sum_{l=0}^{\infty} \frac{B_l}{r^{l+1}} P_l(\cos \theta). \quad (\text{B.4})$$

Applying both boundary conditions, it follows that [55, p. 249-251]

$$\begin{cases} A_l = B_l = 0 & \text{for } l \neq 1, \\ A_1 = -\frac{3}{\varepsilon_r + 2} E_\infty, \quad B_1 = \frac{\varepsilon_r - 1}{\varepsilon_r + 2} R^3 E_\infty \end{cases} \quad (\text{B.5})$$

and the resulting homogenous electric field $\mathbf{E}_\text{in} = -\nabla V_\text{in}$ inside the sphere is given as

$$\mathbf{E}_\text{in} = \frac{3}{\varepsilon_r + 2} \mathbf{E}_\infty. \quad (\text{B.6})$$

The field is shown on the right in fig. B.1. The polarizability α of the sphere can be now be determined to

$$\alpha_\text{sphere} = 4\pi \varepsilon_0 R^3 \left(\frac{\varepsilon_r - 1}{\varepsilon_r + 2} \right). \quad (\text{B.7})$$

Depending on the definition, sometimes the factor $4\pi \varepsilon_r$ is dropped.

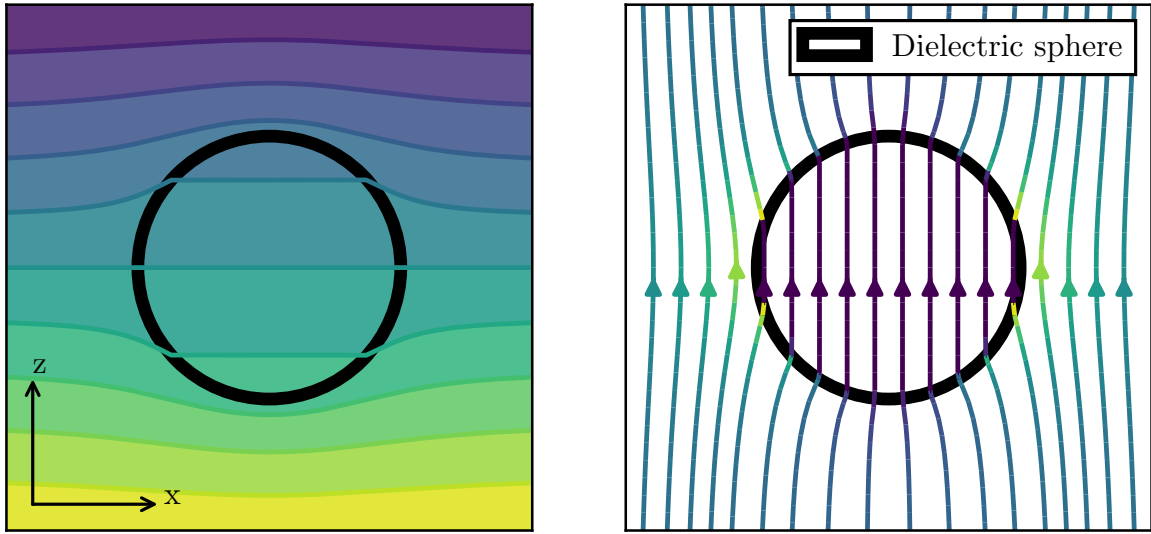


Figure B.1: **left:** Electric potential V of a dielectric sphere in a external electric field $\mathbf{E}_\infty \parallel \mathbf{e}_z$. **right:** The corresponding electric field lines inside and outside the dielectric sphere.

C The shield and its consequences

C.1 Blocking of the shield

Assume two spheres A and B with charge q_A and q_B separated by a distance $2L$ on the x -axis. A circular shield is placed perfectly in the center of the spheres orthogonal to the direct connection between them. The magnitude of the field at a distance z in the direction \mathbf{e}_x from this connection line is given by

$$E_x(z) = \frac{L(q_A - q_B)}{4\pi\epsilon_0(L^2 + z^2)^{3/2}} \quad (\text{C.1})$$

The total flux the circular shield with radius r_s is given by

$$\Phi = \int_0^{r_s} dz \int_0^{2\pi} z d\varphi E_x(z) = \frac{(q_A - q_B)}{2\epsilon_0} \left[1 - \frac{L}{\sqrt{L^2 + r_s^2}} \right]. \quad (\text{C.2})$$

Comparing the total flux for $r_s \rightarrow \infty$ with the flux through the shield, one can arrive at the charge-independent **effectiveness** η of the shield as

$$\eta = \frac{\Phi}{\Phi_\infty} = 1 - \frac{L}{\sqrt{L^2 + r_s^2}} \quad (\text{C.3})$$

and thus a shield with radius

$$r_s = L \sqrt{\frac{1 - (1 - \eta)^2}{(1 - \eta)^2}} \quad (\text{C.4})$$

will block a fraction η of the total field.

C.2 Thermal harmonic oscillator

The amplitude z of a single vibrational shield-mode (k, l) with frequency $\omega_{kl} \equiv \omega$ behaves like a quantum harmonic oscillator. The average amplitude $\langle z \rangle_n = 0$. The variance $(\Delta z)^2 = \langle z^2 \rangle - \langle z \rangle^2$ however is given by

$$(\Delta z)_n^2 = \langle z^2 \rangle_n = \frac{\hbar}{2m\omega} (1 + 2n). \quad (\text{C.5})$$

At a temperature T , the occupation of the modes is described by the boltzmann distribution:

$$\langle z^2 \rangle_T = \sum_{n=0}^{\infty} \frac{1}{Z} e^{-\beta E_n} \langle z^2 \rangle_n, \quad (\text{C.6})$$

where $\beta = 1/k_B T$, $E_n = \hbar\omega(n + 1/2)$ is the energy of mode n and

$$Z = \sum_{n=0}^{\infty} e^{-\beta E_n} = \frac{e^{-\beta \frac{\hbar\omega}{2}}}{1 - e^{-\beta \hbar\omega}} \quad (\text{C.7})$$

is the partition function. Using known series, the expression eq. (C.6) can be evaluated to

$$(\Delta z)_T^2 = \langle z^2 \rangle_T = \frac{\hbar}{2m\omega} \sum_{n=0}^{\infty} \frac{1}{Z} [e^{-\beta E_n} + 2ne^{-\beta E_n}] \quad (\text{C.8})$$

$$= \frac{\hbar}{2m\omega} \left[1 + \frac{2}{Z} \sum_{n=0}^{\infty} ne^{-\beta E_n} \right] \quad (\text{C.9})$$

$$= \frac{\hbar}{2m\omega} \left[1 + \frac{2e^{-\beta \hbar\omega}}{1 - e^{-\beta \hbar\omega}} \right] = \frac{\hbar}{2m\omega} \coth\left(\frac{\hbar\omega}{2k_B T}\right) \quad (\text{C.10})$$

D Calculations

The series expansions of the Casimir terms in the PFA $1/(\mathcal{L}_{A(B)}^i)^2$ from eq. (4.7) are given by:

$$\begin{aligned} \frac{1}{(\mathcal{L}_{A(B)}^i)^2} &\approx \frac{4}{(d-2L+2R)^2} \pm \frac{8\Delta x_{A(B)} \sin \delta}{(d-2L+2R)^3} \pm \theta_{A(B)} \left(\frac{8\Delta x_{A(B)} \cos \delta}{(d-2L+2R)^3} \right) \\ &+ L_{A(B)} \left(\frac{16}{(d-2L+2R)^3} \pm \frac{48\Delta x_{A(B)} \sin \delta}{(d-2L+2R)^4} \right) \pm \theta_{A(B)} L_{A(B)} \frac{48\Delta x_{A(B)} \cos \delta}{(d-2L+2R)^4} \quad (\text{D.1}) \end{aligned}$$

where again the abbreviation $\delta = \alpha, \beta$ was used and the \pm terms align to the corresponding notation in eq. (4.7). The series expansion for the gravitational terms $1/L^{ij}$ with $i, j = 1, 2$ from eq. (4.9) is given by

$$\begin{aligned} \frac{1}{L^{ij}} &= \frac{1}{2L} \pm \frac{\Delta x_B \sin \beta - \Delta x_A \sin \alpha}{8L^2} \mp \theta_A \frac{\Delta x_A \cos \alpha}{8L^2} \pm \theta_B \frac{\Delta x_B \cos \beta}{8L^2} \\ &+ L_A \left(-\frac{1}{4L^2} \pm \frac{\Delta x_A \sin \alpha - \Delta x_B \sin \beta}{8L^3} \right) + L_B \left(-\frac{1}{4L^2} \pm \frac{\Delta x_A \sin \alpha - \Delta x_B \sin \beta}{8L^3} \right) \\ &\pm L_A \theta_A \frac{\Delta x_A \cos \alpha}{8L^3} \mp L_A \theta_B \frac{\Delta x_B \cos \beta}{8L^3} \pm L_B \theta_A \frac{\Delta x_A \cos \alpha}{8L^3} \mp L_B \theta_B \frac{\Delta x_B \cos \beta}{8L^3} \\ &+ L_A L_B \left(\frac{2}{4L^3} \pm \frac{3\Delta x_B \sin \beta - 3\Delta x_A \sin \alpha}{16L^4} \right) \\ &\mp L_A L_B \theta_A \frac{3\Delta x_A \cos \alpha}{16L^4} \pm L_A L_B \theta_B \frac{3\Delta x_B \cos \beta}{16L^4} \quad (\text{D.2}) \end{aligned}$$

The resulting average over $\theta_{A(B)}$ and $L_{A(B)}$ can be computed by

$$\int_{-\infty}^{\infty} d\theta_A d\theta_B dL_A dL_B p(\theta_A) p(\theta_B) p(L_A) p(L_B) e^{i\phi} \quad (\text{D.3})$$

where $p(\cdot)$ is a gaussian probability distribution in the form of

$$p(x) = \frac{1}{\sqrt{2\pi}\Delta x} e^{-\frac{x^2}{2(\Delta x)^2}} \quad (\text{D.4})$$

and ϕ is, as seen in the expansions above, linear in θ_i and L_i with occasional mixed terms. These mixed terms (here denoted by $\Delta A, \Delta B$ for either $\Delta\theta$ or ΔL) can be neglected in first order because in the final result, they appear in the form of

$$\sim \exp \left\{ -\frac{a^2(\Delta A)^2}{2b^2(\Delta A)^2(\Delta B)^2 + 2} \right\} \rightarrow 1 \quad (\text{D.5})$$

D Calculations

which tends to one for small variations $\Delta A, \Delta B \ll 1$ (a, b are constants). Each averaged element of the density matrix can therefore be analytically calculated using

$$\prod_{\Delta A = \{\Delta \theta_{A(B)}, \Delta L_{A(B)}\}} \int_{-\infty}^{\infty} dA \frac{1}{\sqrt{2\pi} \Delta A} e^{-\frac{A^2}{2(\Delta A)^2}} e^{i\phi_1 A} e^{i\phi_2} = \prod_{\Delta A} e^{-\frac{\phi^2(\Delta A)^2}{2}} e^{i\phi_2} \quad (\text{D.6})$$

where again ϕ_1 is the lengthy linearized phase proportional to the series expansions above *and proportional to t* and ϕ_2 is again the lengthy part of the phase independent of the integration parameter A .

As an example, the value of the element $\langle \rho_{12} \rangle$ is given: During time evolution, this element corresponding to $|\psi_A^1 \psi_B^1\rangle \langle \psi_A^1 \psi_B^1|$ picks up the phase (notation from section 4.1)

$$\phi = \phi_{\text{A,Casimir}}^1 + \phi_{\text{B,Casimir}}^1 - \phi_{\text{A,Casimir}}^1 - \phi_{\text{B,Casimir}}^2 + \phi_{\text{Gravity}}^{11} - \phi_{\text{Gravity}}^{12}. \quad (\text{D.7})$$

According to (D.3) and (D.6), the average density matrix element can be calculated analytically yielding

$$\langle \rho_{12} \rangle \approx \exp \left\{ i \left(-\phi_{\text{Casimir}} \frac{16\Delta x_B \sin \beta}{(d - 2L + 2R)^3} + \phi_{\text{Gravity}} \frac{\Delta x_B \sin \beta}{4L^2} \right) t \right\} \quad (\text{D.8})$$

$$\exp \left\{ - \left(\frac{16\Delta x_B \cos \beta}{(d - 2L + 2R)^3} \phi_{\text{Casimir}} - \frac{\Delta x_B \cos \beta}{4L^2} \phi_{\text{Gravity}} \right)^2 \frac{(\Delta \theta_B)^2}{2} t^2 \right\} \quad (\text{D.9})$$

$$\exp \left\{ - \left(\frac{\Delta x_B \sin \beta}{4L^3} \phi_{\text{Gravity}} \right)^2 \frac{(\Delta L_A)^2}{2} t^2 \right\} \quad (\text{D.10})$$

$$\exp \left\{ - \left(\frac{96\Delta x_B \sin \beta}{(d - 2L + 2R)^4} \phi_{\text{Casimir}} + \frac{\Delta x_B \sin \beta}{4L^3} \phi_{\text{Gravity}} \right)^2 \frac{(\Delta L_B)^2}{2} t^2 \right\} \quad (\text{D.11})$$

where

$$\phi_{\text{Casimir}} = \frac{c\pi^3}{720} \left(\frac{\varepsilon_r - 1}{\varepsilon_r + 1} \right) \varphi(\varepsilon_r) R \quad \text{and} \quad \phi_{\text{Gravity}} = \frac{GM_A M_B}{\hbar} \quad (\text{D.12})$$

was used. The resulting logarithmic negativity of $\langle \rho \rangle$ was calculated numerically.